Needle-free Injection Nozzle Geometry

by

John Liu

B.S. in Applied Physics, California Institute of Technology (2009)
S.M. in Mechanical Engineering, Massachusetts Institute of Technology (2012)

Submitted to the Department of Mechanical Engineering
in partial fulfillment of the requirements for the degree of

Doctor of Philosophy in Mechanical Engineering

at the

MASSACHUSETTS INSTITUTE OF TECHNOLOGY

February 2018

Signature redacted

Author .....
Department of Mechanical Engineering
January 18, 2018

Signature redacted

Certified by.....
Ian W. Hunter
Hatsopoulos Professor of Mechanical Engineering
Thesis Supervisor

Signature redacted

Accepted by .....
Rohan Abeyaratne
Chairman, Department Committee on Graduate Theses

Needle-free Injection Nozzle Geometry

by

John Liu

Submitted to the Department of Mechanical Engineering
on January 18, 2018, in partial fulfillment of the
requirements for the degree of
Doctor of Philosophy in Mechanical Engineering

Abstract

The development of needle-free injection (NFI) delivery systems has become increasingly important because of the advantages it affords such as increased patient acceptability, enhanced occupational safety for health providers, safe disposal, and increased speed of mass vaccination in the face of pandemic influenza or bioterror emergencies. Jet injection, wherein drug is propelled at high pressure through a narrow orifice to create a high-speed fluid jet sufficient to penetrate tissue, is one of several needle-free methods for administration of drug. Despite promising research and development, few efforts study the fluid dynamics of NFI and address the role of nozzle design. This thesis presents the development of nozzle geometries and the optimization of the nozzle shape for NFI applications.

We develop nozzle geometries that produce non-axial jets to expand the range of NFI delivery modalities. A rigid, compact, multi-piece ampoule is designed and fabricated as a platform to conveniently house different nozzle inserts one at a time to offer increased jet consistency and functional flexibility. Two nozzle geometries that respectively produce radial jets and intersecting jets are designed and fabricated. Through high-speed imaging and injection into tissue analog and *ex vivo* porcine tissue, we demonstrate the utility of these nozzles for a range of injection applications including intradermal, intratympanic, and traditional uses. The presented ampoule is more successful than a commercial jet injection ampoule in adhering to desired position and velocity trajectories and the energy efficiencies of jet ejections are compared.

Using computational fluid dynamics, we explore how the geometric elements of nozzle shape affect viscous loss and cavitation within the nozzle, the jet's velocity field at the orifice exit, and nozzle wall structural integrity. These insights inform the creation of an objective function and a class of curves used for nozzle shape optimization. A novel nozzle manufacturing technique is developed using a combination of micro-drilling and sink electrical discharge machining to fabricate axisymmetric nozzle orifices. Optically clear planar nozzles are developed and fabricated to image and compare the cavitation within the interior of nozzles of different shapes. The optimized nozzle demonstrates at least a 7% increase in mechanical efficiency and a decrease in cavitation of two orders of magnitude from a commercial jet injection nozzle.

Thesis Supervisor: Ian W. Hunter
Title: Hatsopoulos Professor of Mechanical Engineering

Acknowledgments

I want to first and foremost recognize my PhD advisor, Professor Ian Hunter. His knowledge and expertise that spreads an unusual breadth and depth has provided much to draw from. His example as a constant inventor, scientist, educator, and entrepreneur has provided a ready source of personal inspiration. Because of his philosophy of providing the lab a wealth of equipment and opportunity, I could quickly track from idea to prototype and experiment, week-by-week. I am thankful for his patience towards me as a student from my early days as a Masters student to now as I finish the doctoral thesis.

The two other members on my thesis committee, Professor Pierre Lermusiaux and Professor Mathias Kolle have provided invaluable guidance. I first took Pierre's numerical fluid mechanics class in 2015 and was gripped by a thinker of understanding and warmth. Pierre was particularly helpful in guiding my CFD simulations and optimization. Mathias has been a helpful backboard when tracking through the journey from first thesis committee to defense, and I have enjoyed the many conversations surrounding the experimental and fabrication aspects of my work.

A great part of what has made my graduate experience a rewarding one is the members within the Bioinstrumentation Laboratory. They are top-notch in their fields, colleagues of curiosity and drive, and friends whom I cherish. I want to particularly recognize Dr. Cathy Hogan who has been an invaluable support and colleague, and has provided much of the know-how and necessary understanding for biological experimentation. She is an expert in the needle-free injection space among others and my work would be ill-informed without her input. Dr. Ellen Mazumdar was a crucial source of mentorship and advice when I was a junior student settling into the lab. I cherish the opportunity to have trekked through most of the graduate journey with colleagues and friends Ashin Modak and Ashley Raynal, who have given both invaluable technical and emotional support. Geehoon Park was helpful in the set up of the NFI injector and jet ejection imaging. It has been a pleasure to have the chance to work with other former and current members, such as Dr. Brian Hemond, Nick De-

mas, Craig Cheney, Mike Zervas, Anshul Singhal, Aoyu Zhang, Alison Cloutier, Span Spanbauer, and Randall Briggs. Finally, much thanks to Kate Melvin and Shibani Joshi for all of their unseen assistance–the lab could not run without them.

I am privileged to receive the support of many passionate and compassionate people in the Mechanical Engineering department at MIT are passionate. Professor Maria Yang has been a generous mentor through every major career decision in recent times, from the time I was deciding which graduate school to go to, through the quals process, and when I sought clarity in the decision for the PhD. Professor Peko Hosoi took time out of her busy schedule to help me gain a deeper physical intuition of the fluid mechanics extended a gracious invitation to join Team Peko meetings. Dr. Kaitlyn Hood was helpful in getting me set up with nozzle geometry optimization. Dr. Shabnam Raayai has been a helpful resource in discussing structural mechanics of the tissue and ampoule walls. Jing Lin gave helpful feedback towards CFD studies as a TA of 2.29 and optimization techniques after the class ended. I am thankful for Dr. James Bales' trust and support in lending and teaching me how to use incredible imaging equipment. My research would certainly be much uglier without the Edgerton Center. And finally, Leslie Regan–thank you for keeping all of the cogs and wheels of this department running.

Teaching has been a lifeline during my time as a graduate student. One of the greatest joys in my graduate career has been the opportunity to teach incredible students–people who inspire, motivate, and challenge me to become a better thinker, teacher, and person. I am grateful to have had the chance to teach or develop curriculum for 8.01, 8.02, 2.671, and the Media Lab freshman year program at MIT and Physics 1 and 2 at SUTD. I consider myself fortunate to have the opportunity to teach with passionate world experts, among whom are Professor Ian Hunter, Dr. Barbara Hughey, Dr. Michael Bove, Professor Anantha Chandrakasan, and Christina Chase. Dr. Peter Dourmashkin has been most influential in my teaching career at the university. Being inspired by his way of teaching and personal impact on university students helped convince me that finishing the PhD was indeed a valuable endeavor. I am grateful for his mentorship, example, and friendship over these years.

A number of communities have provided emotional, spiritual, and physical support over these years. From cooking many meals for me in the month leading up to my qualifying exams, seeking truth together, or helping me practice talks, members of the Graduate Christian Fellowship have kindly given up their time and energy to support me. Park Street Church has been a spiritual home for me since 2011. Many have been mentor figures in my spiritual life and church service, such as David Rix, Jason Abraham, Julian Linnell, and Jim Bruce. No personal acknowledgement of this journey would be complete without mentioning Park Street International Fellowship, a community where I have found great fulfillment, peace, and companionship. I am grateful for the opportunity consider Stuart DeLorme a personal mentor, someone who has met with me over countless meals for encouragement and prayer and opened his home, along with Hsuan DeLorme. I am grateful to receive many prayers and support from many dear PSIF friends. If listed, the names and thanks could fill a thesis in itself.

I thank the friends who have walked with me the longest and most closely. I consider myself privileged for the accountability, sense of purpose, and laughter I have had to share with Gerald Pho, Mark Ku, and Thomas Chiasson day-in and day-out over the years. They have been closer than brothers. I am grateful for QT Ren's loyal friendship that has been a quiet but steady impact in my life. David Lee, Ming Yu Ngai, Akin Omigbodun, Guan-ting Ku, Caleb and Christina Yu have celebrated my joys as their joys and my sorrows as their sorrows.

I would like to express gratitude to my family who has given their unconditional love and support since the beginning. My parents, Jay and Yvonne Liu, immigrated from Taiwan to the States for my father to study a PhD in material science at Cornell University. Despite his attempts to dissuade me from STEM in high school because of challenges in the industry, some of my fondest childhood memories are made of making Rube Goldberg machines with him, and I ended up following in his footsteps anyway. My mother has been my longstanding spiritual mentor, who has constantly pointed me to Christ. Her influence is integral in forming who I am today. To Elizabeth and Esther: a cord of three strands is not easily broken, still.

I cannot express enough towards Tiara Liu, the woman I love. She has accompanied me to the laboratory countless weekends and late weekday nights, celebrated in every high and prayed for me with tears in the lows. She has supported me in every endeavor sacrificially and selflessly. I look forward to a life spent with her. Tiara, this accomplishment is as much yours as it is mine.

For my last acknowledgement, I cite an ancient psalm that has grounded and stayed me all of my years here at MIT.

The Lord is my shepherd; I shall not want.
He makes me lie down in green pastures.
He leads me beside quiet waters.
He restores my soul.
He leads me on paths of righteousness
for his name's sake.
Even though I walk through the valley of the shadow of death,
I shall fear no evil,
for you are with me;
your rod and your staff,
they comfort me.
You prepare a table before me
in the presence of my enemies;
you anoint my head with oil;
my cup overflows.
Surely goodness and mercy shall follow me
all the days of my life,
and I shall dwell in the house of the Lord
forever.

Contents

List of Figures **13**

List of Tables **23**

1 Introduction **25**

1.1 Shortcomings of Needle-based Drug Delivery 25

1.2 Needle-Free Drug Delivery Systems 26

1.3 Needle-Free Jet Injection 28

1.4 Basic Calculations and Their Limitations 31

1.4.1 Control Volume Arguments 32

1.4.2 Non-Dimensional Parameters 34

1.5 A General Overview of CFD Simulations 34

1.5.1 Physical Model 35

1.5.2 Meshing 37

1.6 Chapter Descriptions 38

2 Ampoule and Nozzle Development **39**

2.1 Introduction 39

2.2 Ampoule Design and Machining 41

2.3 Nozzle Geometry Function, Design, and Manufacturing 42

2.4 Materials and Methods 44

2.5 Results and Discussion 47

2.6 Summary 53

3 Elements of Axisymmetric Nozzle Geometry **55**

3.1 Introduction 55

3.2 Model Setup 59

3.3 Fluid Flow Analysis 61

3.4 Entrance Fillet 64

3.5 Angle of Entrance 68

3.6 Exit Fillet 70

3.7 Orifice Length 76

3.8 Orifice Angle 81

3.9 Summary 86

4 Nozzle Shape Optimization **89**

4.1 Introduction 89

4.2 Objective Function 89

4.2.1 Fully Developed Flow 90

4.2.2 Cavitation 101

4.2.3 Efficiency 107

4.3 Geometry 108

4.3.1 General Basis Functions 108

4.3.2 Physics Informed Basis Function 109

4.4 Optimization 112

4.5 Summary 114

5 Nozzle Orifice Fabrication **121**

5.1 Introduction 121

5.2 Fabrication of Axisymmetric Nozzles 121

5.2.1 Background on Electrical Discharge Machining 122

5.2.2 Developing a Nozzle Fabrication Method 123

5.2.3 Micro-drilling and Sink EDM Fabrication 126

5.2.4 Post-processing 128

5.3 Fabrication of Planar Nozzles 129

5.4 Manufacturing Informed Geometry Optimization 131
5.4.1 Planar Nozzle Optimization 131
5.4.2 Polycarbonate Axisymmetric Nozzle Optimization 132
5.5 Summary 135

6 Comparisons of Commercial to Optimized Nozzles 141
6.1 Introduction 141
6.2 Efficiency 141
6.3 Cavitation 142
6.4 Summary 149

7 Conclusion 151
7.1 Future Work 152
7.1.1 Experimental confirmation of optimization 152
7.1.2 Cavitation 152
7.1.3 Device development and manufacturing 153

8 Bibliography 155

List of Figures

1-1 Three common needle-free drug delivery systems: a) microneedles, b) epidermal powder ballistics, and c) jet injection. 26

1-2 a) Representative plot of coil position versus time of the linear Lorentz-force actuator and b) injection depth versus jet speed in different animal models. Figures taken from [1]. 29

1-3 a) Actual (blue and red) versus desired (black) piston trajectories in the BioInstrumentation jet injector using a) the traditional PD feedback control and b) adaptive control. Figures taken from [2]. 29

1-4 a) Piston position and b) jet bulk velocity versus time of an Injex ampoule using feedforward control. c) The piston of the Injex ampoule, inset shows the rubber tip (scale bar = 3 mm). 30

1-5 a) Cross-sections of injections into *ex vivo* porcine tissue and b) high-speed images of jets that issue from two Injex nozzles from the same batch (top and bottom) (figures a-b taken from [3]). c) Micro-CT scans of the nozzle interiors at the orifice exit. 31

1-6 The system and control volume (red dotted line) depicts the simple case of a cylindrical NFI syringe, in which a solid piston of radius R_1 is pushed at a speed U(t) into a fluid-filled ampoule of the same radius, forcing the fluid out of a cylindrical nozzle of internal radius R_2. . . . 32

1-7 Representative meshing of the CFD model. b-c) Fillets were introduced at sharp corners and mesh elements in these regions were limited in maximum size to 0.5 μm or less. 37

2-1 The axial jet is limited in its ability to perform a) intradermal injections in clinical settings and b) will likely damage sensitive auditory components in intratympanic injections. 40

2-2 The multi-piece ampoule. A picture showing the four parts (left to right): head, nozzle insert (boxed in red), body, and piston with a close-up of its tip (left inset). A cross section (right inset) shows the ampoule body seats an O-ring in a circular groove, a nozzle insert (boxed in red) that is readily exchanged, and a head that attaches to the threads of the ampoule body and compresses the O-ring to form the fluidic seal. Figures adopted from [4]. 42

2-3 Three nozzles inserts are designed and fabricated to be housed in the ampoule one at a time: (a) the standard nozzle that produces a single jet along the axis of the ampoule for traditional NFI injections, (b) the radial jets nozzle for intradermal injection, and (c) the intersecting jets nozzle for intratympanic injection. (Blue arrows indicate direction of fluid flow, dotted blue signifies dispersed fluid.) Figures taken from [4]. 43

2-4 Representative plots of actual (blue) and desired (red) velocity and position trajectories of the multi-piece ampoule and Injex ampoule during jet ejection (vjet of 160 m/s, tjet of 2 ms, vft of 50 m/s volume of 110 μL). Fluid velocity trajectories of the (a) multi-piece ampoule and (b) Injex ampoule and piston position (volume) trajectories of the (c) multi-piece ampoule and (d) Injex ampoule. Figures taken from [4]. 48

2-5 High-speed images of ejected jets of the (a) standard nozzle (6400 fps), (b) radial jets nozzle (2000 fps), and (c) intersecting jets nozzle (4000 fps). (Scale bars = 3 mm.) Figures taken from [4]. 49

2-6 Acrylamide (left) and *ex vivo* porcine tissue (right) injections of single axial jets produced by the standard nozzle (top) and the Injex ampoule (bottom).Figures taken from [4]. 50

2-7 Injections of the radial jets nozzle. (a) High-speed images of an injection into acrylamide gel, (b) image of the erosion holes and boluses in acrylamide gel post-injection, and (c) midline cross section of injected *ex vivo* porcine tissue.Figures taken from [4]. 51

2-8 Injections of the intersecting jets nozzle. (a) High-speed images of an injection into acrylamide gel, images of acrylamide gels after tympanic membrane analog injection of (b) the intersecting jets nozzle and (c) the Injex ampoule, and (d) midline cross section of injected *ex vivo* porcine tissue.[4] 52

2-9 Ejection efficiencies of the studied ampoule configurations. Efficiency is calculated as the ratio between output mechanical kinetic energy of the jet and input electrical energy into the actuator. Figures taken from [4]. 53

3-1 a) High-speed still of a collimated jet issuing from the radial jets nozzle. b) A close-up of the jet reveals a straight jet at lower speeds (top) and axisymmetric dispersion at high speeds (bottom). 56

3-2 a) Dispersion in jets that issue from fuel injector nozzles is caused by cavitation within the injector nozzle. b) The farther the cavitation extends down the orifice, L*, the larger the spray angle of the jet. Figures taken from [5]. 57

3-3 Pipe losses associated with pipe entrance geometry. Figures taken from [6]. 58

3-4 An overview of the key issues of fluid dynamics and tissue mechanics accounted for in the needle-free injection space. 59

3-5 Set up with a) boundary conditions and b) elements of axisymmetric geometry for parametric study. 60

3-6 Pressure field of the orifice of a cylindrical nozzle. A large negative pressure exists at the sharp corner (z = 1 mm) and and larger downstream region of lesser negative pressure. The lower limit to the shown pressure is -6 MPa and the upper limit is 3.169 kPa, the vapor pressure of water at 25 °C. 63

3-7 a) Streamlines of flow in geometries where entrance fillet is swept from 0.1 to 50 μm. The red box indicates the area of b) magnified streamline plots. 65

3-8 Velocity profiles of geometries where entrance fillet is swept: a) axial velocity magnitude, b) radial velocity, and 3) maximum % difference between the set of velocity profiles. 66

3-9 Mechanical efficiencies of geometries where entrance fillet is swept. . . 67

3-10 a) Cavitation pressure regions of geometries where entrance fillet is swept from 0.1 to 50 μm. The red box indicates the area of b) magnified plots. 68

3-11 a) Streamlines of flow in geometries where entrance angle is swept from 0 to 60 degrees. The red box indicates the area of b) magnified streamline plots. 69

3-12 Velocity profiles of geometries where entrance angle is swept: a) axial velocity magnitude, b) radial velocity, and 3) maximum % difference between the set of velocity profiles. 71

3-13 Mechanical efficiencies of geometries where entrance angle is swept. . 72

3-14 a) Cavitation pressure regions of geometries where entrance angle is swept from 0 to 60 degrees. The red box indicates the area of b) magnified plots. 72

3-15 a) Streamlines of flow in geometries where exit fillet is swept from 0.1 to 50 μm. The red box indicates the area of b) magnified streamline plots. 73

3-16 Velocity profiles of geometries of different exit fillet radii: a) axial velocity, b) radial velocity, and 3) maximum % difference between the set of velocity profiles. 75

3-17 Mechanical efficiencies of geometries where exit fillet radius is swept. 76

3-18 a) Cavitation pressure regions of geometries where exit fillet is swept from 0.1 to 50 μm. The red box indicates the area of b) magnified plots. 77

3-19 Representative image of streamlines at the orifice entrance for the orifice length sweep. 77

3-20 Velocity profiles of geometries of different orifice lengths: a) axial velocity, b) radial velocity, and 3) maximum % difference between the set of velocity profiles. 79

3-21 Mechanical efficiencies of geometries of different orifice lengths. 80

3-22 a) Cavitation pressure regions of geometries where entrance fillet is swept from 0.1 to 50 μm. b) Representative pressure plot at the orifice entrance. 81

3-23 a) Streamlines of flow in geometries where orifice angle is swept from 0 to 60 degrees. The red box indicates the area of b) magnified streamline plots. 82

3-24 Velocity profiles of geometries where orifice angle is swept: a) axial velocity magnitude, b) radial velocity, and 3) maximum % difference between the set of velocity profiles. 84

3-25 Mechanical efficiencies of geometries where orifice angle is swept. . . . 85

3-26 a) Cavitation pressure regions of geometries where orifice angle is swept from 0 to 60 degrees. The red box indicates the area of b) magnified plots. 85

4-1 Three general areas of shape optimization - objective function, geometry space, and optimization method. 90

4-2 The force exerted onto tissue using jets of two types of flow of the same flow rate are compared: plug flow (left) and Poiseuille flow (right). For a first-order model, the approximation is made that all of a jet's kinetic energy is converted into static energy upon impinging the tissue surface. Thus the velocity profile (top row) is used to derive the axial force per unit surface area exerted on the tissue surface (bottom row). 92

4-3 The geometry and boundary conditions used to simulate the stress field caused by a jet impinging on the surface of skin. An axisymmetric geometry with side b as the centerline was used. 93

4-4 First principal stress fields induced in tissue by a) a jet of plug flow at 150 m/s and b) a jet of Poiseuille flow of the same flow rate (color bar represents stress in Pascals). 94

4-5 The geometry and boundary conditions used to simulate a water jet ejected into a a glycerol reservoir. An axisymmetric geometry with side b as the centerline was used. 95

4-6 Inlet boundary condition was set to a velocity field uniform over the inlet radius (plug flow) that varied over time. The velocity time profile has a high velocity phase v_{jet} designed to breach the tissue followed by a lower velocity phase v_{follow} designed to deliver the bulk of the drug [1]. 96

4-7 Simulation of an ejection of a jet of water into glycerol. Regions of red are occupied by water and regions of green are occupied by glycerol, a) where the black box indicates the window of zoom for the b) time-lapse snapshots from 0 to 25 μs. Depth of ejection, d, is defined as the maximum distance in the axial direction the boundary of the water travels within 25 μs. 97

4-8 Depth of jet ejection into glycerol versus length of orifice. The depth of injection only slightly increases with greater orifice length and greater more fully developed flow. 98

4-9 a) Given a desired (green) and actual (blue) velocity profile, we can define $V^*(r)$ as the L2 norm of the two velocity profiles. 99

4-10 a) Inlet power and outlet power, b) mechanical efficiency, and c) axial velocity profiles (at outlet) of pipes of length that ranges from 0.25 to 10 mm and constant inlet velocity of 200 m/s. 102

4-11 a) Inlet power and outlet power, b) mechanical efficiency, and c) axial velocity profiles (at outlet) of pipes of constant length 1 mm and inlet velocities that ranges from 150 to 240 m/s. 103

4-12 By tracking a seed bubble down many streamlines that span across the nozzle, one can estimate the amount of cavitation a nozzle will produce and the regions where cavitation will occur. a) A sample streamline of the flow in a cylindrical nozzle. b) The pressure along the sample streamline a fluid particle or bubble will experience. c) A first-order estimate of the radius of the bubble as it travels along the streamline. d) By plotting 50 streamlines spanning the entire nozzle, one can predict where the cavitation will occur in the region of flow. The flow region is represented by a grayscale plot, where white is assigned to no bubble and fully black is assigned to a bubble of 5 μm radius. 105

4-13 10th order Chebyshev and 10th order rational Chebyshev polynomials fit to a given nozzle shape. Red is the fit and black is the target nozzle shape. 109

4-14 Maximum difference between sample nozzle shape and their normal and rational Chebyshev polynomial fits. 110

4-15 Given profiles of a) bulk velocity or c) bulk velocity squared such as linear, quadratic, or cubic, the b, d) nozzle shapes to produce such bulk shaping can be directly computed. 111

4-16 a) Solutions to the 1-D convection diffusion equation at different values of "time", shown here a range of 1/20 to 1. b) Given average inlet and outlet velocity, and length, mapping the the solutions form profiles of bulk velocity. c) Using conservation of mass flow, nozzle shapes are calculated from the bulk velocity profiles. 115

4-17 CFD solves of sample geometries generated by the bulk shaping approach. Total velocity is shown here as a 2D surface plot. Sweeping the one parameter, non-dimensional "time", yields a range of nozzle shapes. 116

4-18 Results of optimization using objective function Z_1: a) loss residual, b) velocity field residual, and total residual. 117

4-19 Results of optimization using objective function Z_2: a) loss residual, b) cavitation residual, and total residual. 118

4-20 The optimized geometry of the Z_2 objective function: length = 0.5 mm, TF = 0.025. (Scale bar = 1 mm.) 119

5-1 Electrical discharge machining operates on the principle of spark erosion [7]. a) Hundreds of volts are applied across a liquid dielectric filled gap between the electrode and workpiece, generating thousands of sparks per second and b) forming an ionized channel between workpiece and electrode. c) Each spark produces a tiny crater by melting and vaporizing, thus eroding the workpiece to the shape of the tool. . 123

5-2 Metal machining of electrodes. a) CAD drawing of an electrode, the shape of which is the modeled after the interior of the injex ampoule. b) Electrodes are turned on the EMCO lathe, yielding c - d) electrodes with tips with diameters as small as 30 μm. 124

5-3 Graphite electrode machining. a-b) The EMCO mini-lathe was outfitted with a custom air evacuation and HEPA filter system to clear the air of graphite debris, yielding c-d) graphite electrodes. 125

5-4 Sink EDM electrode using different materials. Left column pictures show fresh electrodes, right column of pictures show electrodes after machining to show tool wear. 127

5-5 Materials are imaged on the SEM after sink EDM machining: a) stainless steel 316, stainless steel 420, and carbon steel alloy 1045. 128

5-6 A fabrication method is developed that involves three stages of micro-machining: micro-drilling, small-feature sink, and large-feature sink. 129

5-7 a) A post-processing method ejects an air-sand mixture to sands the interior of nozzles. b) Nozzles of dispersed jets produce c) collimated jets after post-processing. 130

5-8 1 mm sheet aluminum is cut on the Wire EDM to form a monolithic aluminum structure of which the nozzle shape forms the interior cut-out. The cut-outs of the following geometries are shown: cylindrical, Injex, and optimized planar nozzle 131

5-9 The 2D clear nozzle is composed of a two aluminum plates cut by wire EDM, sandwiched between two optically clear cast acrylic walls, and attached to an circular adapter to fit into the multi-piece ampoule. A 2D version of the cylindrical nozzle was a) first designed in CAD then b) fabricated and tested. 131

5-10 Planar Nozzle Optimization: a) the planar nozzle objective function and b) the optimized geometry for planar nozzles. (Scale bar = 1 mm.) 132

5-11 Fluid-structure model setup: geometry and boundary conditions. . . . 133

5-12 Total velocity and von Mises stress fields of nozzles. Polycarbonate nozzles of geometries hosting large pressure gradients such as a) TF0.025L0.5, will fail, while other nozzle geometries such as the b) TF0.2L2 will not fail. 135

5-13 Structural residual for polycarbonate nozzles. 136

5-14 a) Manufacturing-informed objective function, b) the optimized nozzle for objective function Z_4. 136

5-15 Overview of the final optimization framework for nozzle shape optimization. 139

6-1 Nozzles commonly used in needle-free injection industry or research are compared to the optimized nozzle: a) Injex nozzle, b) cylindrical orifice, c) O'Keefe nozzle, d) SPT nozzle, and e) Bird Precision 24 nozzle. 142

6-2 Efficiency comparison of commercial available nozzles with the optimized planar nozzle. 143
6-3 Comparison of simulated cavitation between commercial available nozzles and the optimized nozzle. 144
6-4 Cavitation metric comparison of commercial available nozzles with the optimized nozzle geometry. 145
6-5 Imaged cavitation within the planar nozzle of the cylindrical shape. Cavitating bubbles appear as dark patches because they refract and scatter the light away from the camera lens and sensor. The red box in the first frame indicates the area of zoom of the subsequent frames. Orange lines denote the nozzle walls to distinguish between the dark wall and cavitation in the orifice. 146
6-6 Side-by-side comparisons between the simulated (left) and imaged cavitation (right), where orange lines in the cavitation image indicate the nozzle walls. Black regions represent regions of cavitation in both simulated and imaged cavitation. 147
6-7 COMSOL simulation of an ejection of water into atmospheric air. Regions of blue are occupied by air and regions of red are occupied by water. As water is ejected from the nozzle with increasing speed, the slowly moving jet front bunches together and is pushed out by the faster traveling fluid behind it, eventually forming a "curling lip". . . . 148
6-8 The curling lip is imaged in the fluid flow of planar nozzles. The curling lip develops until t = 0.613, after which the faster moving fluid behind the curling lip penetrates through to form the jet. 149
6-9 Imaged cavitation of three different nozzle geometries in the planar nozzle: cylindrical, Injex, and the optimized planar nozzle. Left column of pictures shows the nozzle at t = 0, where the black line near the orifice exit shows the initial water-air interface. The right picture column shows the nozzle at full flow, where orange lines indicate nozzle walls. 150

List of Tables

1.1 Non-dimensional parameters of a 200 μm diameter liquid water jet traveling through air at 175 m/s. 34
1.2 Summary of CFD simulations. 35

3.1 Default values for cylindrical geometry parametric studies. 61

5.1 Overview of manufacturing methods for nozzle orifices. 122
5.2 Characteristics of tested electrode materials. 137
5.3 Characteristics of tested workpiece materials. 138

Chapter 1

Introduction

1.1 Shortcomings of Needle-based Drug Delivery

The traditional paradigm of drug injection using needles and syringes poses significant issues to safety and drug delivery efficacy. First and foremost, needles pose serious hazards to every level of society–the general public, health care worker, and end user. While trained healthcare workers in hospitals and clinics in the US and Canada report numbers as low as 0.18 injuries per healthcare worker per year, it is estimated that in countries such as Egypt and Pakistan, each healthcare worker experiences 4.7 sharps-related injuries each year [8], each costing an average of $400 [9], leading to over 80,000 contractions of HCV, HBV, or HIV [10]. Despite the low cost of materials and manufacturing of disposable and resterilizable needles and syringes ($0.06 per injection), when the expenses for iatrogenic infections are factored in, the total cost increases by more than an order of magnitude [8]. Outside traditional health care settings, it is estimated that 3 billion needles and syringes in the US are used and mostly disposed in household trash. Because laws and regulations are less stringent for household waste than for waste produced in hospitals and clinics, effectively unregulated residential sharps disposal creates a large public risk [11].

Second, the primitive nature of the needle limits the control over which tissue layer is targeted, inhibiting the efficacy of some drugs. For example, instead of delivering to the epidermis or dermis, which hosts much of the body's antigen-presenting cells

[12], general needles are designed for delivery to the subcutaneous or muscle tissue layer. For some vaccines, intradermal deliveries of amounts as small as 10-20% of the original dose can induce immunoresponses similar to subcutaneous or intramuscular deliveries of full doses [13]. The needle's inability to deliver to the skin may obstruct financial saving and global impact in vaccination.

Along with other issues such as patient compliance, cross-contamination due to needle reuse, belenophobia, and discomfort [8] the needle's safety hazards and limitation on drug efficacy make development of alternative drug-delivery paradigms attractive.

1.2 Needle-Free Drug Delivery Systems

NFI delivery systems are promising due to key advantages such as increased patient acceptability, enhanced occupational safety for health providers, safe disposal, and increased speed of mass vaccination in the face of pandemic or bioterror emergencies. Three of the most common needle-free drug delivery systems are highlighted in Figure 1-1.

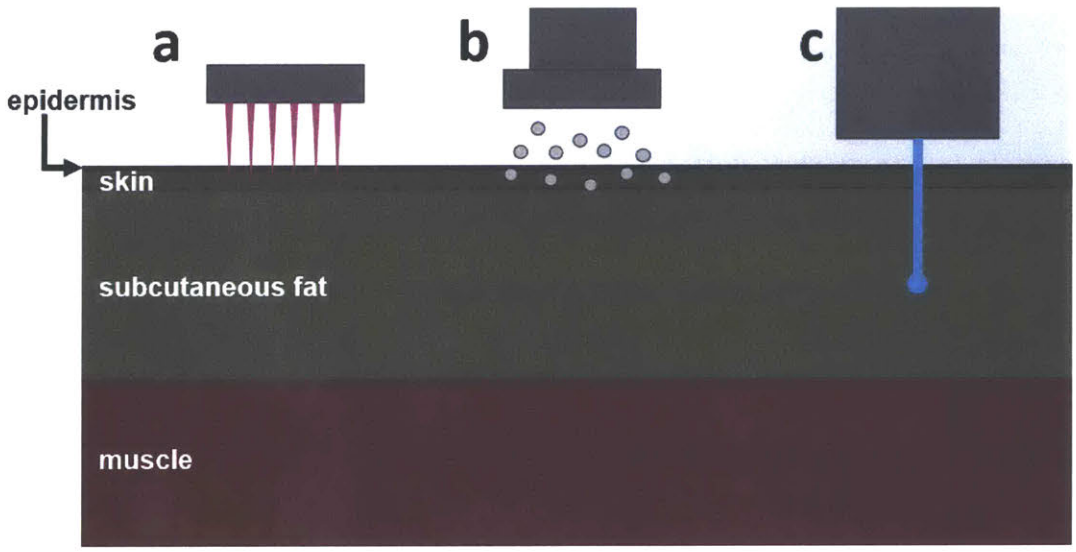

Figure 1-1: Three common needle-free drug delivery systems: a) microneedles, b) epidermal powder ballistics, and c) jet injection.

Microneedles are small needles that are pressed against the skin to puncture the tough stratum corneum and deliver drugs to the epidermal and dermal layers of the skin (Figure 1-1a). They garner interest because of their ability to deliver vaccines directly to the viable epidermis and because of decreased sensations of pain in patients due to their short length that limits the fracturing to only the top layers of skin where few nerves enervate. Recent advances in microneedles include development of mass-manufacturing methods to decrease cost and increase accessibility to the public, development of solid needles that dissolve after penetration into tissue, and the broadening of types of drugs that can be delivered. However, microneedle drug delivery is limited in its delivery volume and injection sites are limited to within the skin because of their length.

Epidermal powder ballistic delivery works on the principle of accelerating individual powdered particles using a carrier gas traveling beyond the speed of sound such that each particle has sufficient momentum to penetrate through the stratum corneum and into the viable epidermal layer (Figure 1-1b). Delivery of powdered vaccines instead vaccines reconstituted in liquid could be advantageous because of their decreased sensitivity to temperature fluctuations and potential to alleviate issues related to cold-chain storage and transportation. However, this delivery modality is also limited in its delivery depth.

Jet injection operates on the principle of pressurizing liquid drug in an ampoule to propel through a narrow orifice a high-speed fluid jet sufficient to penetrate tissue (Figure 1-1c). This delivery modality is of particular interest because of the jet's ability to pierce the skin and deliver drug to range of depths within the tissue, enabling a targeting of sites that range from the dermal to the muscle layer. Further, current jet injection technology can delivery drugs of volumes ranging from 10 μL to more than 250 μL, a greater volume than most other needle-free delivery paradigms.

1.3 Needle-Free Jet Injection

Prior Art and Development

Current commercial NFI jet injection devices use a variety of forms of stored energy for actuation, such as compressed springs, gases, or explosive chemicals. However, these forms of actuations provide limited command over pressure, no active feedback control, and thus little control on the resultant location of the delivery site. Recent work in the NFI research field developed and implemented piezoelectric actuation [14] to control the pressure versus time profile experienced in the drug ampoule, and therefore enhance control over the jet's behavior and consequent delivery depth and volume. However, because of the limited travel of piezoelectric stacks, the volume of drug delivered was limited to 20 μL.

The MIT BioInstrumentation Laboratory has developed a highly controllable, linear Lorentz-force actuator for use in needle-free injection. By controlling the coil position and therefore pressure profile to resolutions within 1 ms (Figure 1-2a) the BioInstrumentation jet injector is able to delivery to a variety of depths, as demonstrated in *ex vivo* tissue and live animal models (Figure 1-2b). Further, because of the extended travel of the actuator, the jet injector is able to deliver drug of volumes ranging from 10 μL to over 250 μL [1, 15]. Recent work has also advanced active feedback control from a traditional PD feedback control architecture to adaptive control to better dictate the pressure in real-time and adjust for variations caused by tissue load (Figure 1-3) [2].

Current Limitations

While actuator and controller designs advance, little has been done to research and innovate on the part of the injector furthest downstream and closest to the tissue: the ampoule and nozzle.

First, consider the piston performance of the ampoule of the Injex, a well-accepted needle-free injector in the current industry. Analyzing the piston's position versus

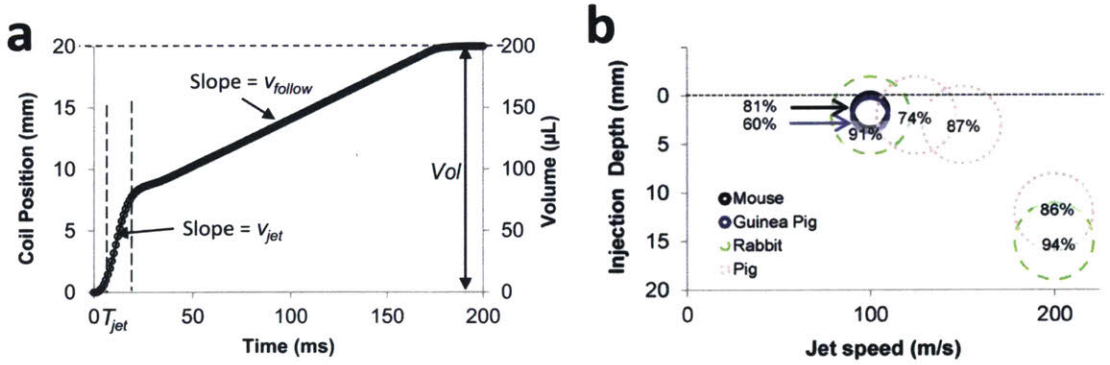

Figure 1-2: a) Representative plot of coil position versus time of the linear Lorentz-force actuator and b) injection depth versus jet speed in different animal models. Figures taken from [1].

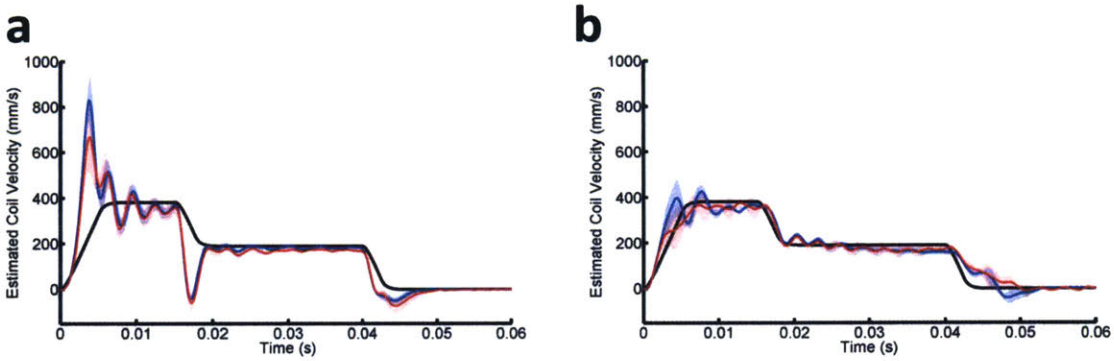

Figure 1-3: a) Actual (blue and red) versus desired (black) piston trajectories in the BioInstrumentation jet injector using a) the traditional PD feedback control and b) adaptive control. Figures taken from [2].

time trajectory reveals significant deviation between the actual and desired trajectories (Figure 1-4a). These deviations translate to further decreased control of the bulk velocity of the jet that issues from the orifice, as demonstrated in the velocity versus time trajectory (Figure 1-4b). It is conjectured that the rubber tip of the piston (Figure 1-4c) lowers the compliance, increases the ringing during injection, thereby decreasing the control over the jet velocity, and consequent volume and depth of delivery [16].

A second and greater limitation is presented by the injex ampoule. It is expected that using the same actuator, pressure profile, and control architecture will yield sim-

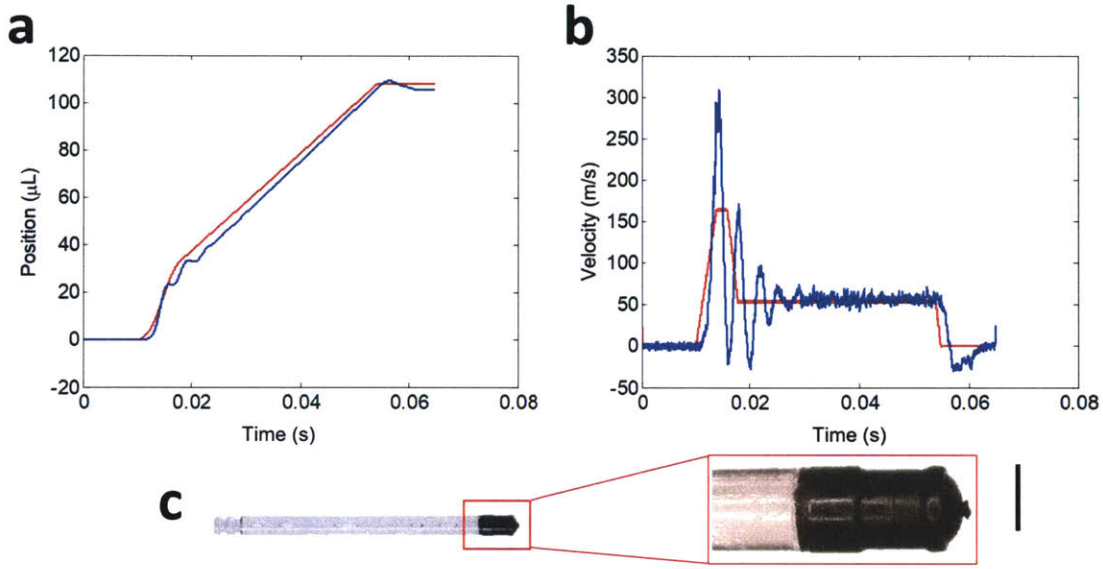

Figure 1-4: a) Piston position and b) jet bulk velocity versus time of an Injex ampoule using feedforward control. c) The piston of the Injex ampoule, inset shows the rubber tip (scale bar = 3 mm).

ilar injection patterns into *ex vivo* tissue. Using one injex ampoule for a series of injection indeed yields deep injection patterns that each breach through the dermal and subcutaneous fat and into the muscle layer (Figure 1-5a). However, changing to another injex ampoule within the same batch of ampoules yields a set of shallow injection patterns that breaches through the dermal layer and slightly into the subcutaneous fat (Figure 1-5a). High-speed imaging demonstrates that one of jets that issue from the nozzles of these two ampoules is fairly collimated in nature, while the other is entirely dispersed (Figure 1-5b). While Injex nozzles from the same batch are intended to be the same, micro-CT scanning reveals the interior three-dimensional geometry of nozzles to be drastically different (Figure 1-5c). The variability of nozzle geometry in ampoules due to loose manufacturing tolerances presents an uncontrolled factor that compromises the consistent formation of collimated jets all nozzles needed for research experiments.

To ensure precise and uniform nozzle geometry, some research groups use stainless steel orifices [16] or ceramic nozzles [17] that are incorporated into custom-made ampoules. While the geometry of such orifices are manufactured to micron tolerances

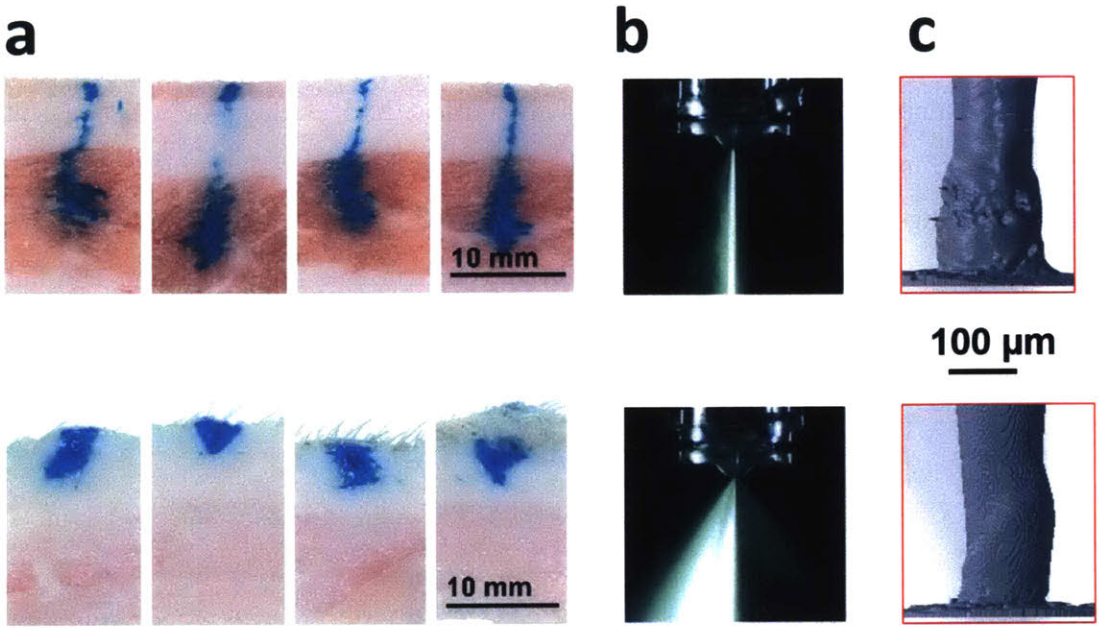

Figure 1-5: a) Cross-sections of injections into *ex vivo* porcine tissue and b) high-speed images of jets that issue from two Injex nozzles from the same batch (top and bottom) (figures a-b taken from [3]). c) Micro-CT scans of the nozzle interiors at the orifice exit.

and do not deform over the course of repeated experiments, nozzle geometries are constrained to produce single axial jets and the nozzle shape is limited to cylinders and cones.

No prior work has been dedicated to studying fluid flow through the nozzle or the influence of three-dimensional nozzle geometry on NFI fluid flow. This major gap in understanding inhibits the advance of NFI technology. It is therefore no surprise that the design of ampoule and nozzle has remained static over the past decades.

1.4 Basic Calculations and Their Limitations

To lay a basic understanding of fluid flow within the nozzle of the needle-free jet injector, common calculations are carried out and their limitations are discussed.

1.4.1 Control Volume Arguments

Figure 1-6 depicts the simple case of a cylindrical NFI syringe, in which a solid piston of radius R_1 is pushed at a speed U(t) into a fluid-filled ampoule of the same radius, forcing the fluid out of a cylindrical nozzle of internal radius R_2. To first approximation, we treat the piston, cylinder, and tube as inflexible, and the fluid density, with density ρ, as incompressible.

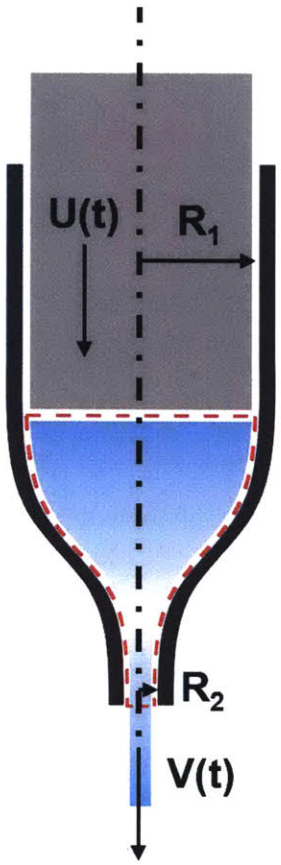

Figure 1-6: The system and control volume (red dotted line) depicts the simple case of a cylindrical NFI syringe, in which a solid piston of radius R_1 is pushed at a speed U(t) into a fluid-filled ampoule of the same radius, forcing the fluid out of a cylindrical nozzle of internal radius R_2.

All points of the control surface are fixed in the chosen reference frame and attached to just inside the walls, except the top surface is just below the piston surface and moves downward at the piston speed U(t). Using mass conservation theorem,

$$\frac{d}{dt}\int_{MV(t)} \rho\, dV = \frac{d}{dt}\int_{CV(t)} \rho\, dV + \int_{CS(t)} \rho(\vec{v} - \vec{v_c}) \cdot \vec{n}\, dA,$$

where MV is the mass volume, CV is the control volume, CS is the surface of the control volume, v is the velocity of the fluid through the surface, and v_c is the velocity of the surface.

The first term is zero because mass is conserved, the second term non-zero because the CV's volume changes as the piston moves down. The outflow term in the surface integral is the only non-zero term, as there is no inflow into the CV from the top because the fluid moves at the same speed as the piston. Thus equation 1 yields

$$\frac{d}{dt}\int_{CV(t)} \rho\, dV + \frac{d}{dt}\int_{CS(t)} \rho v_{rn}\, dA = 0,$$

where $v_{rn} = \vec{v} \cdot \vec{n} = vcos(\theta)$ is the outward normal velocity component of the fluid at the velocity relative to the control surface at that point. The first term above is zero because we have assumed incompressible flow. In the second term, $v_{rn} = -U(t)$ at the top of the CS with area πR_2^2. At the exit plane, the area is πR_2^2 and the velocity is V(t) on average. We can thus evaluate for V(t):

$$V(t) = \frac{R_1^2}{R_2^2} U(t).$$

Because we have not assumed anything about the three-dimensional nozzle geometry, the same control volume argument for any other geometry of inlet radius R_1 and outlet radius R_2. That is, the same U(t), R_1, R_2 yields the same V(t).

There are two limitations to this type of flow analysis that are immediately apparent. First, while using U(t) to describe the velocity at any point of the top surface is accurate because the piston indeed produces plug flow right at the piston surface, V(t) and can only be treated as the average velocity of the bulk fluid. However, different velocity profiles at the orifice exit may yield different injection results. Second, this model fixes U(t) but provides no information on how much pressure it will require to push the piston at that velocity.

1.4.2 Non-Dimensional Parameters

The dominant forces acting in the fluid flow of a jet can be determined by calculating non-dimensional flow parameters (Table 1.1). A 200 μm diameter liquid water jet traveling through air 175 m/s is considered as a representative example. Because the Reynold's number is well over 1000, inertial forces dominate viscous forces and the flow is turbulent. A large Weber number, indicates that inertial forces also dominate surface tension. A large Froude number indicates indicates that inertia dominates gravitational forces. A small Ohnesorgue number indicates that inertial and surface tension forces dominate viscous forces. The forces acting upon the jet in order of descending magnitude are: inertia, surface tension, viscosity, and gravity.

Non-Dimensional Parameter	**Value**
Reynold's Number	3.93×10^{4}
Weber Number	4.25×10^{-4}
Froude Number	3.12×10^{-7}
Ohnesorgue Number	5.25×10^{-3}

Table 1.1: Non-dimensional parameters of a 200 μm diameter liquid water jet traveling through air at 175 m/s.

Empirical and basic analytic expressions relate pressure drop with pipe radius, length, and friction factor in fully developed pipe flow. While these relations will be used in Chapters 3 and 4 to provide physical intuition, the radius of nozzle geometries may change rapidly along the nozzle axis, and pipe flow analysis is limited. Given the limitations of basic analytical fluid mechanics techniques, much of the study's design and optimization of nozzle geometry is informed by Computational Fluid Dynamics (CFD).

1.5 A General Overview of CFD Simulations

Comsol Multiphysics 5.3 was used to model fluid flow and its associated effects in this body of work. Simulations brought insight, raised questions, and informed design on virtually every type of work and thus are interspersed through the chapters of this thesis. Because there was a range of different types of phenomenon relevant to the

work, a number of different physics modules were used. While the relevance of each phenomenon to needle-free injection will be justified or demonstrated through the thesis, it may be helpful for the orientation of the reader to first lay out an overview of the simulations. The types of phenomenon simulated, the physics modules used, and their chapter locations are shown below in Table 1.2.

Type of flow Simulation	**Chapter**
Single phase, turbulent flow (k-epsilon)	3, 4, 5, 6
Turbulent Two-phase, Phase Field	4
Fluid-structure interaction	5

Table 1.2: Summary of CFD simulations.

For most of the work presented in this thesis, the primary module used was the Comsol fluid flow module simulating single-phase, turbulent flow. The model is generally described here; modifications unique to other studies will be described as these studies come up.

1.5.1 Physical Model

The equations of motion for a single-phase fluid are the continuity equation and the momentum equation:

$$\frac{\partial \rho}{\partial t} + \nabla \cdot (\rho u) = 0,$$

and

$$\rho \frac{\partial u}{\partial t} + \rho u \cdot \nabla u = -\nabla p + \nabla \cdot (\mu(\nabla u + (\nabla u)^T) - \frac{2}{3}(\nabla \cdot u)I) + F,$$

where:

- ρ is the density (kg/m^3)
- u is the velocity vector (m/s)
- p is the pressure (Pa)

- T is the viscous stress (Pa)
- F is the volume force vector (N/m^3)
- C_p is the specific heat capacity at constant pressure (J/(kg·K))
- T is the absolute temperature (K)
- q is the heat flux (W/m^2)
- $Q4$ contains the heat sources (W/m^3)
- S is the strain-rate tensor:

$$S = \frac{1}{2}(\nabla u + (\nabla u)^T.$$

Because we are implementing the 2D axisymmetric formulations of Navier Stokes equations, $\frac{\partial}{\partial \phi} = 0$ and we also assume no swirl flow ($u_{phi} = 0$).

We employ the k-ϵ turbulence model, one of the most widely accepted turbulence models in industrial applications [18]. The model introduces two additional transport equations and two dependent variables: the turbulent kinetic energy, k, and the turbulent dissipation rate, ϵ.

$$\mu_T = \rho C_\mu \frac{k^2}{\epsilon},$$

where C_μ is a model constant.

The transport equation for k reads:

$$\rho \frac{\partial k}{\partial t} + \rho u \cdot \nabla k = \nabla \cdot ((\mu + \frac{\mu_T}{\sigma_k} \nabla k) + P_k - \rho \epsilon),$$

where the production term is

$$P_k = \mu_T (\nabla u \cdot (\nabla u + (\nabla u)^T) - \frac{2}{3}(\nabla \cdot u)^2) - \frac{2}{3}\rho k \nabla \cdot u.$$

The transport equation for ϵ reads:

$$\rho\frac{\partial\epsilon}{\partial t}+\rho u\cdot\nabla\epsilon=\nabla\cdot((\mu+\frac{\mu_T}{\sigma_\epsilon})\nabla\epsilon)+C_{\epsilon1}\frac{\epsilon}{k}P_k-C_{\epsilon2}\rho\frac{\epsilon^2}{k}.$$

1.5.2 Meshing

The free triangular shape was used to mesh the majority of the geometry (Figure 1-7a). 5 to 8 boundary layer meshing elements were introduced at the nozzle walls, and meshing elements in the region of sharp transitions such as fillets were limited in maximum size to 0.5 μm (Figure 1-7b-c). The region of the jet's travel in the water reservoir was also refined to a maximum element size of 14 μm. The total mesh commonly yielded 40,000 to 80,000 total elements and 1000 to 2000 boundary elements.

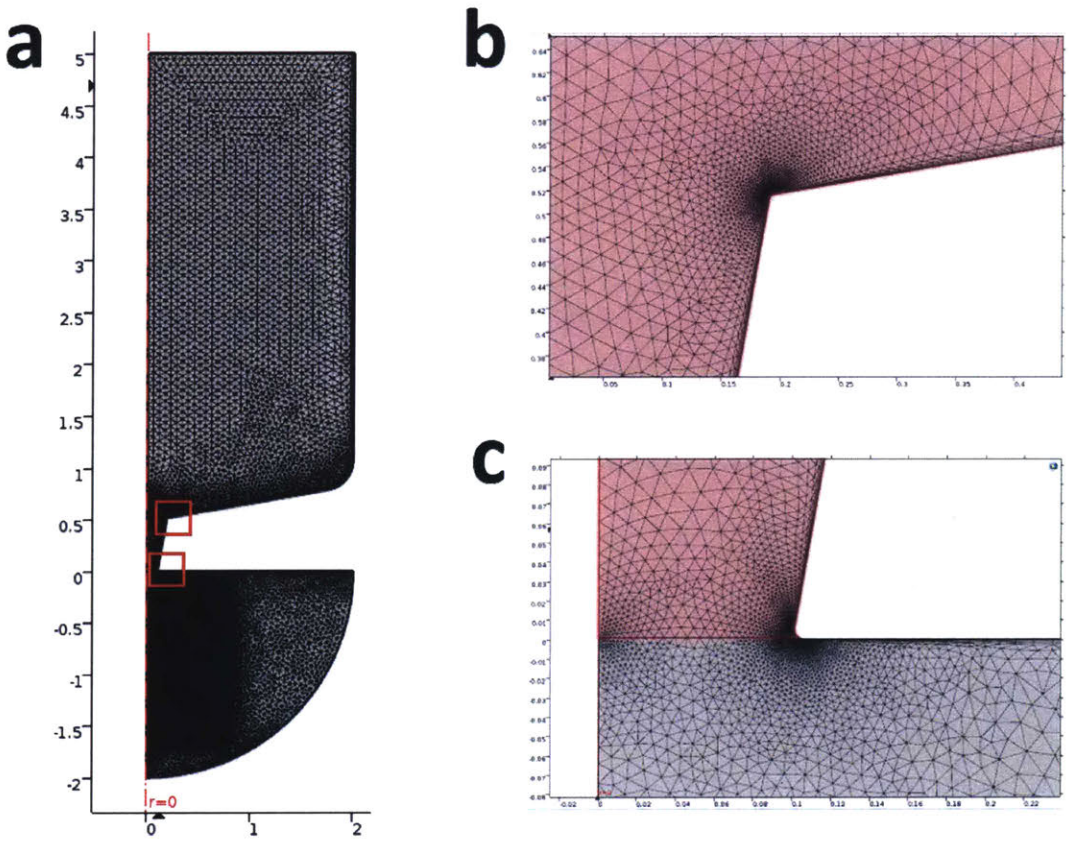

Figure 1-7: Representative meshing of the CFD model. b-c) Fillets were introduced at sharp corners and mesh elements in these regions were limited in maximum size to 0.5 μm or less.

1.6 Chapter Descriptions

Chapter 2 describes the development and fabrication of a rigid ampoule to house various nozzle inserts and two non-axial nozzle geometries that are developed and demonstrated to have potential for intradermal and intratympanic membrane injections.

Chapter 3 is an investigation of the effect of elements of axisymmetric nozzle geometry on fluid flow. Five different elements of cylindrical geometry are examined through parametric studies. Streamlines of the flow, velocity profile at the orifice exit, overall mechanical efficiency of the nozzle, and cavitation pressure regions within the interior of the nozzle are examined for each parametric study.

Chapter 4 presents the framework of optimization for the nozzle shape. Various computational tools are developed to provide residuals for optimization and are considered for the choice of an appropriate optimization function. A set of curves serve as a basis functions to capture the range of nozzle geometries of interest. Optimized nozzles are found using objective function composed of the residuals of velocity field, loss, and cavitation.

Chapter 5 describes the fabrication of axisymmetric nozzles for needle-free injection and planar nozzles for cavitation imaging. Residuals relating the structural integrity of manufactured nozzles are developed, yielding two manufacturing-informed optimized geometries.

Chapter 6 presents experimental and computational comparisons between commercially available nozzles and optimized nozzles.

Chapter 7 summarizes the contributions of the thesis and highlights areas of future work.

Chapter 2

Ampoule and Nozzle Development

2.1 Introduction

Current challenges associated with the Injex ampoule such as the poor controllability of the jet dynamics due to low system compliance and the lack of consistent collimated jet formation due to manufacturing tolerances of the nozzle geometry are detailed in Chapter 1 and present opportunities for innovation of the ampoule and nozzle. However, the opportunity to advance the state of needle-free injection is not limited to addressing specific limitations associated with the Injex ampoule.

In traditional jet injection, jets that issue from the nozzle travel parallel to the axis of the jet. While the "axial jet" can be used to deliver drug to a number of injection sites, there are a number of types of needle-free injections that are challenging to carry out with an axial jet.

Consider intradermal delivery of drug. Intradermal delivery can be challenging because the jet must puncture the tough stratum corneum but make sure the jet's axial momentum is not too great that it penetrates beyond the 1 to 3 mm thick dermal layer (Figure 2-1a). In a research context, intradermal delivery of drugs is readily achieved because the tissue can be cross-sectioned after injection and the pressure profile of injection can be calibrated accordingly until the jet primarily deposits the drug bolus within the dermal layer. In a clinical setting however, this calibration process is not possible. Because the fracture toughness and thickness of the skin varies

by person, the range of pressure profiles that can successfully achieve intradermal delivery is tight and varies from person to person, thus rendering intradermal delivery challenging in the clinic.

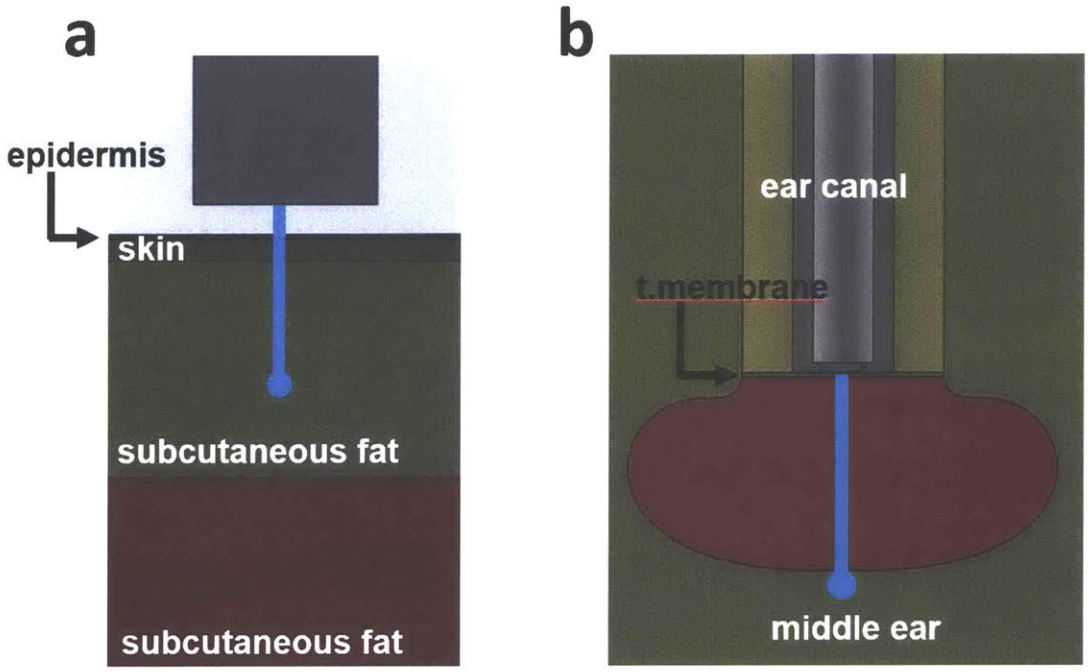

Figure 2-1: The axial jet is limited in its ability to perform a) intradermal injections in clinical settings and b) will likely damage sensitive auditory components in intratympanic injections.

Another situation of interest is for the jet to puncture a barrier but disperse immediately afterwards. In intratympanic injection for example, the eardrum acts as a barrier between the outer ear and the drug delivery site of the middle ear, where sensitive components such as the auditory ossicles lie. An axial jet would successfully puncture the eardrum but given its axial momentum would also likely continue to travel past the eardrum and damage sensitive components within the ear (Figure 2-1b).

The issues detailed in Chapter 1 and above motivate the development of a rigid ampoule and the design of nozzle geometries that broaden the modalities of jet injection. In this chapter, the development of an ampoule that offers increased jet consistency and functional flexibility is presented. A rigid, compact, multi-piece am-

poule has been designed and fabricated as a platform to conveniently house different nozzle inserts, one at a time. Three different nozzle geometries that respectively produce a single axial jet, radial jets, and intersecting jets are designed, fabricated, demonstrated, and compared to a commercial JI ampoule.

2.2 Ampoule Design and Machining

The multi-piece ampoule system (Figure 2-2) consists of four parts: 1) a body in which the drug is stored, 2) a piston that travels through the entirety of the ampoule body, 3) a nozzle insert, and 4) a hex head that attaches to the threads of the ampoule to create the necessary force against the O-ring to create a fluidic seal between the nozzle insert and ampoule body. The ampoule body, head, and nozzle are composed of 303 stainless steel, whereas the piston is machined out of W1 tool steel (cross section shown in 2-2 right inset).

The ampoule body is 40 mm long and has an inner diameter of 3.53 mm with a volume drug capacity of over 350 μL. The exterior features of the body are machined using a CNC lathe, and the body's cavity is machined via three steps: drilling, reaming, and three stages of honing (120, 340, and 600 grit). This yields a polished surface finish to enable the fluidic seal required between the piston and interior of the ampoule body. The interior of the hex head has inner threads 6.5 mm long that end with an inner relief of 1 mm—this means that the ampoule can easily host nozzle inserts of 1 to 5 mm in axial length, and lengths less than 1 mm if a spacer is placed between the nozzle insert and inner face of the ampoule hex head.

The piston composed of W1 tool steel has two Buna-N O-rings (durometer rating of 70A) that sit behind the head in grooves—the first O-ring serves as the primary fluidic seal while the second enables the piston's alignment to the axis of the ampoule body. Because the tip of the presented piston is rigid and cannot be deformed as can some of the commercial piston tips (e.g. Injex) the tip geometry was designed to match the interior geometry of the nozzle, to avoid introducing a bubble into the ampoule when drug is drawn into the ampoule. In this presentation (2-2 left inset)

the piston tip was designed to match the interior of the Injex nozzle.

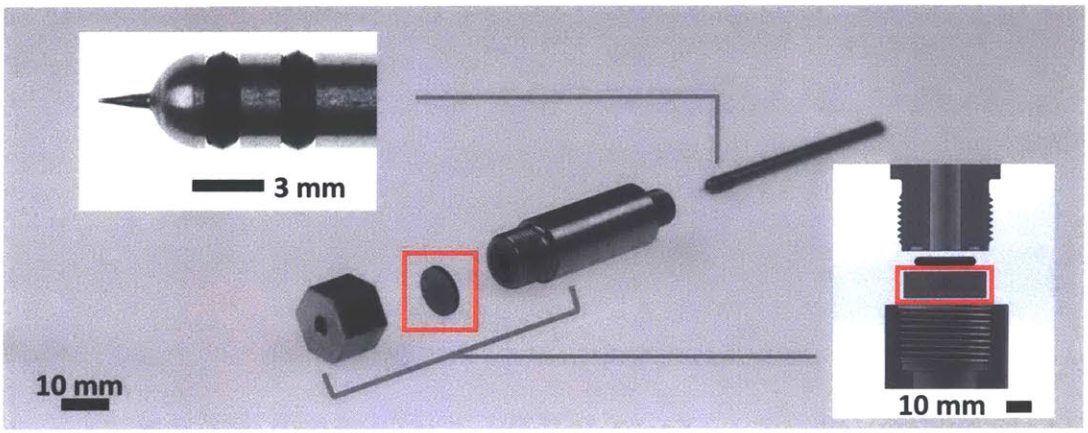

Figure 2-2: The multi-piece ampoule. A picture showing the four parts (left to right): head, nozzle insert (boxed in red), body, and piston with a close-up of its tip (left inset). A cross section (right inset) shows the ampoule body seats an O-ring in a circular groove, a nozzle insert (boxed in red) that is readily exchanged, and a head that attaches to the threads of the ampoule body and compresses the O-ring to form the fluidic seal. Figures adopted from [4].

2.3 Nozzle Geometry Function, Design, and Manufacturing

Three nozzles are designed and fabricated (Figure 2-3): the standard nozzle, the radial jets nozzle, and the intersecting jets nozzle. Because of the multi-piece ampoule design, each of these nozzles of different overall geometries are readily housed in the multi-piece ampoule without any additional adjustment.

The standard nozzle produces a single jet along the axis of the ampoule providing a standard of comparison to most commercially available nozzles (including the Injex) (Figure 2-3a). 0.5 to 1 mm thickness disks of 303 stainless steel were cut using a wire electrical discharge machine (wire EDM). The surfaces were polished either using a grinding wheel or finishing passes on the wire EDM. The orifice is created using a 200 μm diameter micro-drill and standard drill press (Servo, Model 1760).

The radial jets nozzle diagrammed in Figure 2-3b is designed specifically for intra-

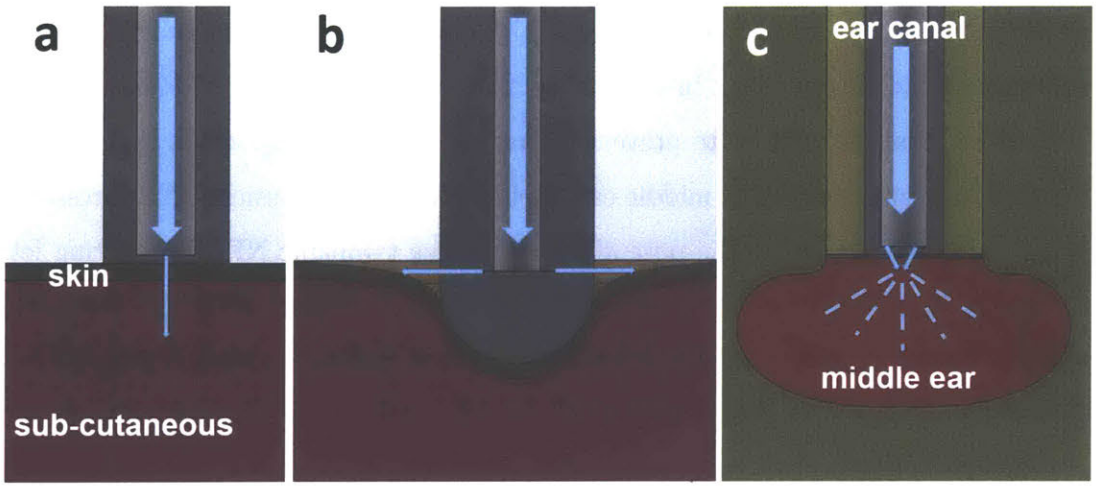

Figure 2-3: Three nozzles inserts are designed and fabricated to be housed in the ampoule one at a time: (a) the standard nozzle that produces a single jet along the axis of the ampoule for traditional NFI injections, (b) the radial jets nozzle for intradermal injection, and (c) the intersecting jets nozzle for intratympanic injection. (Blue arrows indicate direction of fluid flow, dotted blue signifies dispersed fluid.) Figures taken from [4].

dermal injection. Dermal therapeutics that may benefit from intradermal NFI include vaccine, anesthetic, and dermal filler delivery. Jets for intradermal injections must fulfill two conditions: 1) cause the drug to breach the dermis but 2) avoid depositing the bulk of the drug beyond the dermis. Because the human dermis ranges from 2 to 3.5 mm in thickness and the epidermal toughness ranges from location to location, the range of velocity profiles for traditional axial jets that will achieve both conditions is both tight and highly variable between site to site and person to person. The radial jets nozzle is machined out of carbon steel on a CNC lathe. The head is 5 mm in diameter and has the end of a sphere to match the profile of the skin when indented by the nozzle. Two orifices are created using a 150 μm diameter micro-drill on opposing sides of the nozzle right above the sphere end. When the nozzle is indented into the skin, the exiting jets are aligned with the plane of the skin. Thus, as long as the dermis is breached, a jet will generally remain traveling in the dermis regardless of a lower or higher velocity.

The intersecting jets nozzle is purposed for the general class of NFI applications where there exist areas beyond a certain distance that will be damaged by a high

velocity jet or a fixed depth is otherwise a high priority. In intratympanic injections, for example, an NFI jet must breach the tympanic membrane then suddenly lose the bulk of its axial momentum to prevent damaging sensitive components that lay just beyond the membrane in the middle ear, such as the auditory ossicles. The presented nozzle (Figure 2-3c) offers the potential to actualize tympanic NFI by shooting jets to breach the tympanic membrane, then intersecting with each other, thereby losing much of its kinetic energy. Intersecting jets has found application in debridement [17] but to the authors' knowledge, no such development exists for NFI application.

The intersecting jets nozzle is machined out of 303 stainless steel on a CNC lathe. The head is composed of a long and slender column 4 mm in diameter to travel through the ear canal until the nozzle face rests against the tympanic membrane. Two orifices 1.73 mm apart at 30 degree angles with respect to the ampoule axis are created using a 200 μm diameter micro-drill, producing two jets that intersect 1.5 mm from the exit. Because micro-drills will slip and eventually break if used to drill at a significant angle, a shallow 2 mm diameter conical recess is first machined, yielding an incline that presents a perpendicular surface for angled micro-drilling.

2.4 Materials and Methods

Jet Injector System

Experimentation was performed using the controllable Lorentz-force actuated jet injection device developed in the MIT BioInstrumentation Lab. The position control of the coil is achieved using a compact reconfigurable system consisting of a real-time controller (cRIO-9004, National Instruments, Austin, TX) embedded in a reconfigurable field-programmable gate-array (FPGA) chassis (cRIO-9113) as detailed in [1].

High-Speed Imaging

The ejections of fluid jets into air and injections into acrylamide gel were recorded by a high-speed CMOS video camera (Vision Research, Phantom V9) fitted with a

50 mm compact macro lens (Canon Compact Macro-Lens EF) at frame rates of 2000 to 6400 frames per second (fps) with exposure times of 155 to 500 μs. Lighting was provided by an arrangement of halogen LED lamps.

Injections

For injections into tissue analog, acrylamide gel (gel 10%) was prepared as described in [19] and injection into gels was visualized using 1:100 dilution of blue tissue marking dye (Polysciences). After injection, the acrylamide gels were photographed on a lightbox using a Canon 7D camera with a 100 mm compact macron lens (Canon Compact Macro-Lens EF). The same velocity profile was used across all acrylamide injections: jet velocity (v_{jet}) of 100 m/s, time at v_{jet} (t_{jet}) of 2 ms, follow through velocity (v_{ft}) of 50 m/s, with a volume per injection of 50 μL.

Two types of injections were additionally carried out to demonstrate the function of a radial jets nozzle and intersecting jets nozzle. For the radial jets nozzle, injections into *ex vivo* porcine abdominal tissue were carried out. For the intersecting jets nozzle, injections into *ex vivo* porcine tissue and tympanic membrane analog were done.

Post-mortem tissue was obtained through the MIT Tissue Harvest Program using procedures approved by the IUCAC and in accordance with the NIH Guide for the Use and Care of Laboratory Animals. Tissue was harvested from the abdomen of Yorkshire pigs (approximately 6 months) immediately after euthanasia and included skin and underlying subcutis and muscle. The tissue was trimmed, immediately vacuum sealed, and stored at -80°C. Prior to injection, each sample was thawed at 4°C and equilibrated to room temperature. The radial jets nozzle was placed in direct contact with the tissue and pressed in such a way that the bottom edge of the ampoule hex lightly contacts the skin. Porcine tissue samples were injected with tissue marking dye (as above), using a (v_{jet} of 160 m/s, (t_{jet} of 2 ms, (v_{ft} of 50 m/s, and volume of 50 μL, after which the tissue was frozen, medially sectioned, splayed injection side up, and photographed using a Canon 1D camera and 100 mm lens.

Tympanic membrane analog injections were set up by fixing a tympanic membrane analog over a vial of acrylamide gel (10%) in which the surface of the gel was more

than 2 mm below the top lip of the vial–the gel represents the sensitive auditory components beyond the tympanic membrane. A tympanic membrane analog was composed by fixing silicone rubber onto porous paper, yielding a sheet of 0.13 mm thickness. The face of the intersecting jets nozzle was placed in direct contact with the membrane. After injection, the acrylamide gel was photographed in the same way as described above for acrylamide injections.

Ejection Efficiency

The ejection efficiency is calculated as a ratio of the mechanical kinetic energy of the exiting jet over the electrical energy input to the coil of the Lorentz-force actuator. The electrical energy input is calculated by performing a discrete time integration of the product between the current and voltage profiles,

$$E_{in} = E_{electrical} = \sum_i P(i)V(i)\Delta t,$$

where P is power, V is voltage, and Δt is the time step.

To calculate the mechanical kinetic energy of the jet, the inlet velocity is first calculated by taking the discrete derivative of the position profile of the piston, then smoothed using a third order Savitzky-Golay filter. The outlet velocity, v_{outlet}, is then calculated using conservation of mass, in which the velocity profile of the jet across the diameter of the orifice has been approximated as uniform,

$$v_{outlet}(i) = \frac{A_{inlet}}{A_{outlet}} \frac{x(i) - x(i-1)}{\Delta t},$$

where A_{inlet} and A_{outlet} are areas of the inlet and outlet, respectively, and x is the position of the piston. The mechanical energy output is then calculated as the discrete time integration of the product between dynamic pressure and flow rate,

$$E_{out} = E_{kinetic} = \sum_i \left(\frac{1}{2}\rho(i)^2)(\pi r^2 v_{outlet}(i)\right)\Delta t,$$

where ρ is the fluid density and r is the orifice radius.

In all numerical integrations, Δt is 10 μs. Ten ejection trials were performed using the same velocity profile ((v_{jet} of 100 m/s, (t_{jet} of 2 ms, (v_{ft} of 50 m/s, and volume of 50 μL) to obtain the average efficiency and standard deviation. Nozzle radii were measured using a scanning electron microscope (SEM, TM3000 Hitachi).

2.5 Results and Discussion

Piston Trajectory

Figure 2-4 compares the performances of the Injex ampoule and multi-piece ampoule in a side-by-side plot comparison of representative trajectories of exit velocity of the fluid (Figure 2-4a-b) and piston position (Figure 2-4c-d) over time. In both cases, there are two instances of significant deviation from the desired exit velocity. The first is the spike up in velocity at the beginning of the (v_{jet} phase and the second is the spike down in the transition at the end of the (v_{jet} phase. The velocity spikes due to the rigid piston's travel in the multi-piece ampoule are significantly smaller in the case of the multi-piece ampoule–$\sim$80% and 65% less than those observed of the original velocity spikes in the Injex configuration. A significant decrease in ringing during the (v_{jet} phase of the ejection using the multi-piece ampoule is also observed. The presented system significantly improves the adherence of the actual velocity trajectories to the desired trajectories.

Jet Ejections

High speed imaging shows that jets ejected from the standard nozzle, radial jets nozzle, and intersecting jets nozzle are well collimated and not dispersed (Figure 2-5a-c). Unlike the often-observed defects in Injex ampoules introduced by commercial injection molding [3], the cylindrical orifices produced by micro-drilling do not generally have significant burrs or internal obstructions to flow and thus the manufacturing of the presented nozzles consistently yield nozzles that produce collimated jets. In the ejected jets from the intersecting jets nozzle, significant dispersion and fluid atomiza-

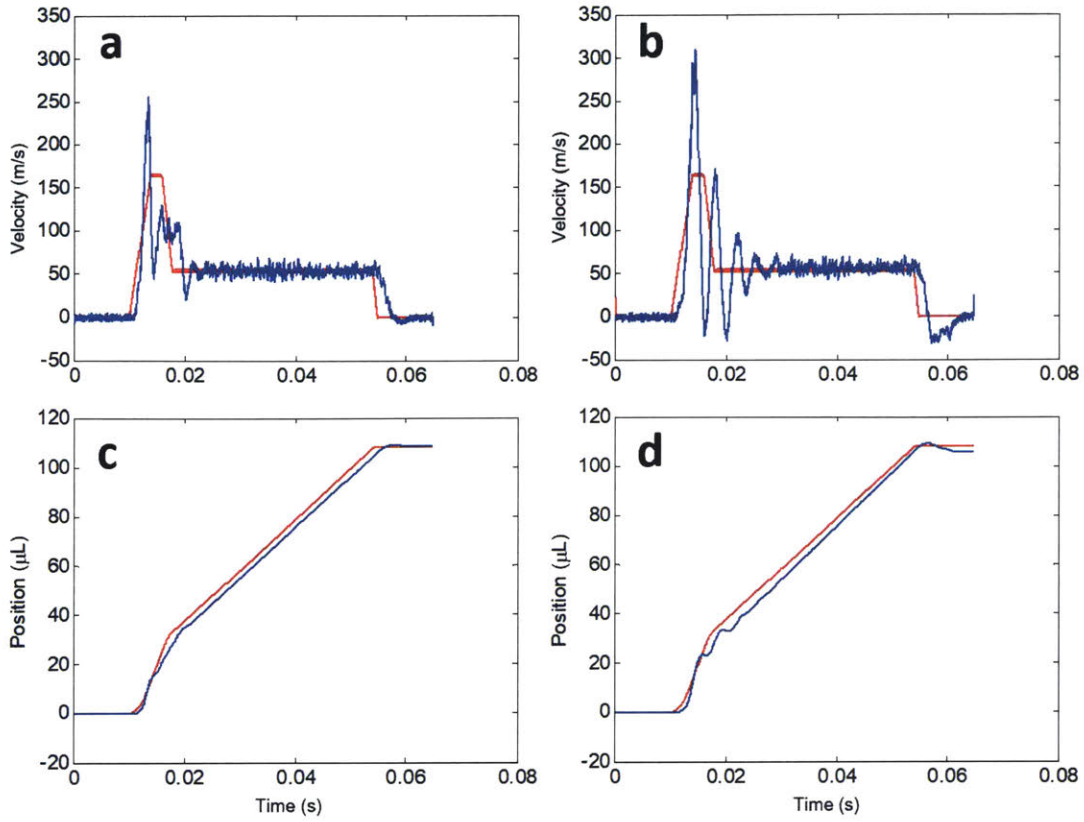

Figure 2-4: Representative plots of actual (blue) and desired (red) velocity and position trajectories of the multi-piece ampoule and Injex ampoule during jet ejection (vjet of 160 m/s, tjet of 2 ms, vft of 50 m/s volume of 110 μL). Fluid velocity trajectories of the (a) multi-piece ampoule and (b) Injex ampoule and piston position (volume) trajectories of the (c) multi-piece ampoule and (d) Injex ampoule. Figures taken from [4].

tion is observed 1.5 mm downstream. Because these nozzle inserts are machined out of stainless steel or carbon steel, the interior geometry will not deform over time and is therefore suitable for controlled experiments over many trials.

Standard Nozzle

Injection into acrylamide gel and *ex vivo* porcine tissue via a jet from a standard nozzle yields the commonly-observed channel and bolus (Figure 2-6a,c) [20, 21], similar to the injection shape caused by a jet from the Injex ampoule using the same injection parameters (Figure 2-6b,d).

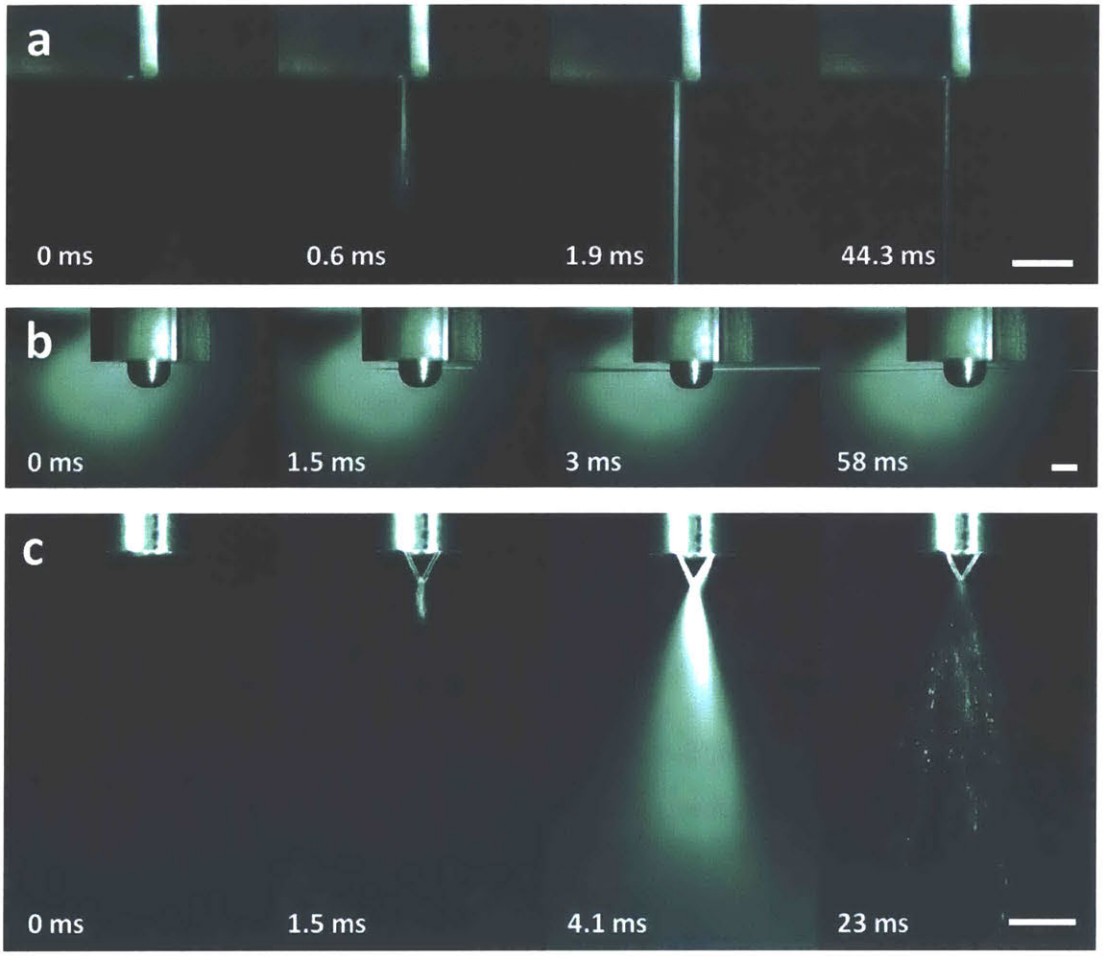

Figure 2-5: High-speed images of ejected jets of the (a) standard nozzle (6400 fps), (b) radial jets nozzle (2000 fps), and (c) intersecting jets nozzle (4000 fps). (Scale bars = 3 mm.) Figures taken from [4].

Radial Jets Nozzle

High speed imaging of injection using a radial jets nozzle into acrylamide gel shows jet penetration within a couple milliseconds and a fully formed bolus in 10 ms (Figure 2-7a). It is further observed that much of the injected dye escapes through the top side of the bolus at the gel surface. This is because the fracture plane occurs close to the surface of the gel, consequently breaking open the surface, unlike traditional axial jet gel injections. In the image of the acrylamide after injection (Figure 2-7b) the two erosion holes curve upwards towards the surface because the acrylamide gel that is previously indented by the spherical end of the nozzle during injection, is restored

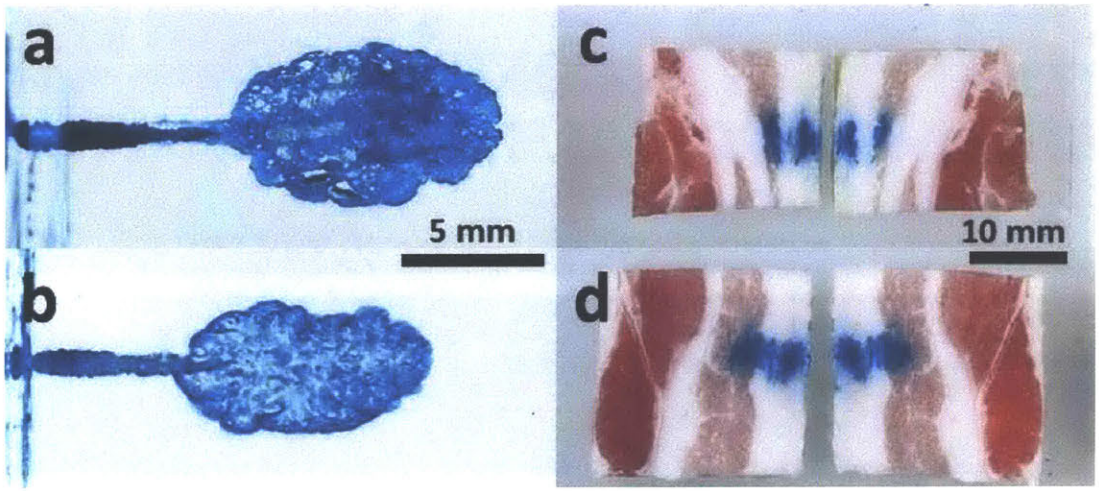

Figure 2-6: Acrylamide (left) and *ex vivo* porcine tissue (right) injections of single axial jets produced by the standard nozzle (top) and the Injex ampoule (bottom).Figures taken from [4].

upwards to its original flat surface post-injection. Injections into porcine tissue (Figure 2-7c) yielded injected boluses that remained within the dermis (injection depths of 1.1 and 1.3 mm).

Intersecting Jets Nozzle

High speed imaging of injection into acrylamide gel using intersecting jets shows the formation of a bolus when the jets intersect (Figure 2-8a). The center of the resultant bolus 2-8b) is shallower than that of single axial jets using the same injection parameters 2-6a-b). The two erosion holes are not visible after injection because they are subsumed by the growing fracture plane of the gel during the duration of the injection. When the same jets pierce the tympanic membrane analog, there is insufficient energy to puncture the acrylamide 2-8b) unlike an axial jet produced by an Injex ampoule 2-8c). These results suggest the potential of the intersecting jets nozzle for intratympanic membrane NFI.

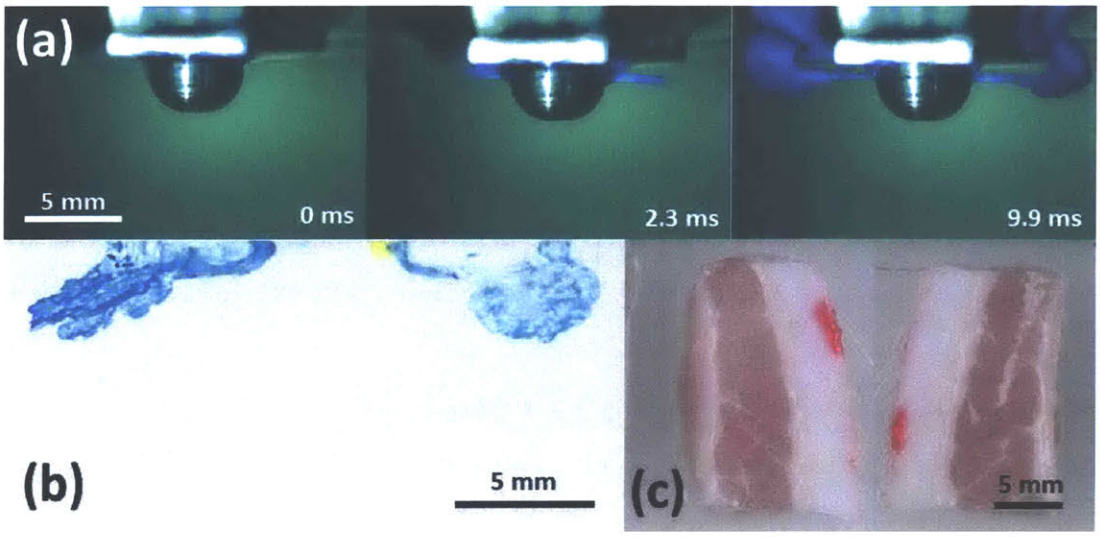

Figure 2-7: Injections of the radial jets nozzle. (a) High-speed images of an injection into acrylamide gel, (b) image of the erosion holes and boluses in acrylamide gel post-injection, and (c) midline cross section of injected *ex vivo* porcine tissue.Figures taken from [4].

Ejection Efficiency

The ejection efficiencies of the presented configurations range widely between 3% and 19%, with the intersecting jets nozzle exhibiting the highest efficiency and the radial nozzle the lowest efficiency 2-9). Because the power amplifier, controlling electronics, and jet injector are the same, differences in efficiency should primarily come from the differences of friction between piston and ampoule and fluid flow energy loss in the nozzle orifices. There is no statistical difference between the injection efficiencies using an Injex ampoule or that of a standard nozzle housed in a multi-piece ampoule—both produce single jets of comparable diameter (196 μm and 216 μm, respectively). This similarity may also suggest that the primary ampoule-specific energy loss is due to fluid flow losses and not piston-wall frictional losses, which merits further control studies.

We conjecture that the large difference between efficiencies of the nozzles that produce single axial jets and efficiencies of the radial jets and intersecting jets nozzle, are primarily due to head loss in the fluid flow. While the total orifice area of the radial jets nozzle is larger than the standard nozzle and Injex (42.7×10^{-9} m^2 compared

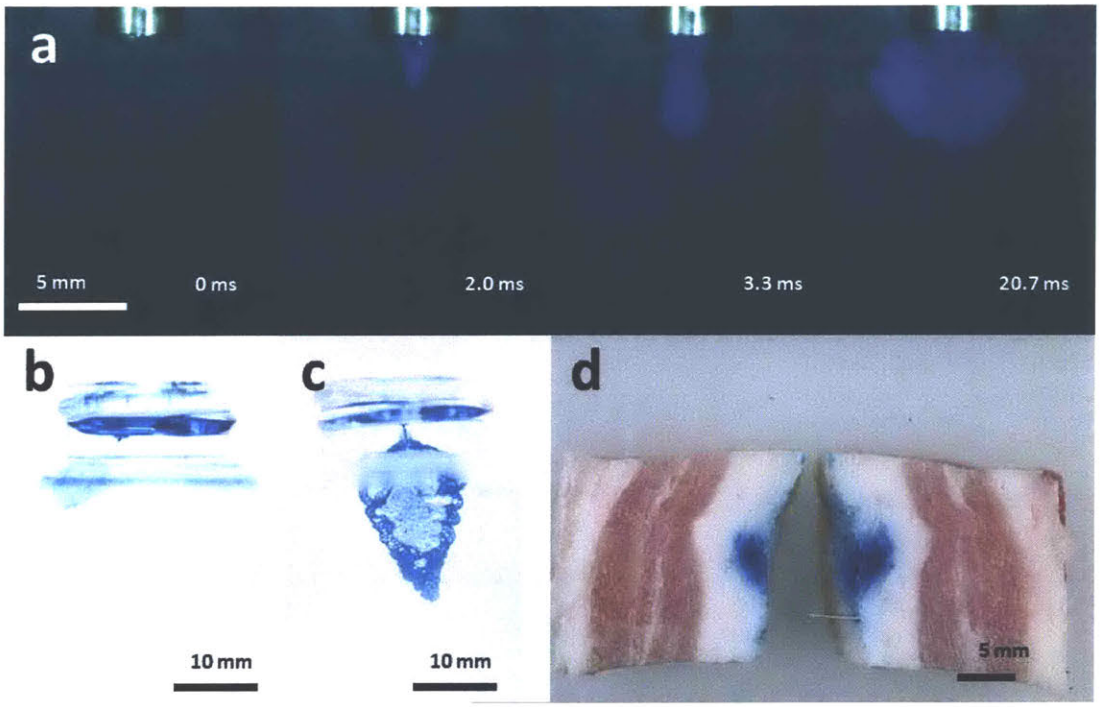

Figure 2-8: Injections of the intersecting jets nozzle. (a) High-speed images of an injection into acrylamide gel, images of acrylamide gels after tympanic membrane analog injection of (b) the intersecting jets nozzle and (c) the Injex ampoule, and (d) midline cross section of injected *ex vivo* porcine tissue.[4]

to 3.02×10^{-9} m^2 and 0.0366 $(mm)^2$, respectively), the diameter—and therefore characteristic length of flow—is up to 20% smaller, leading to a significant decrease in Reynold's number, thereby increasing its nozzle discharge coefficient. The diameter of the orifices of the intersecting jets nozzle (202 μm) are comparable in size with the nozzles that produce single axial jets, however two orifices yield a significantly larger total orifice area (64.1×10^{-9} m^2), thereby decreasing its effective resistance coefficient and decreasing losses. It is also conjectured that slight misalignment between the axes of the piston and ampoule lead to varying frictional losses from trial to trial. Future work will entail improving alignment to decrease variation in ejection efficiency.

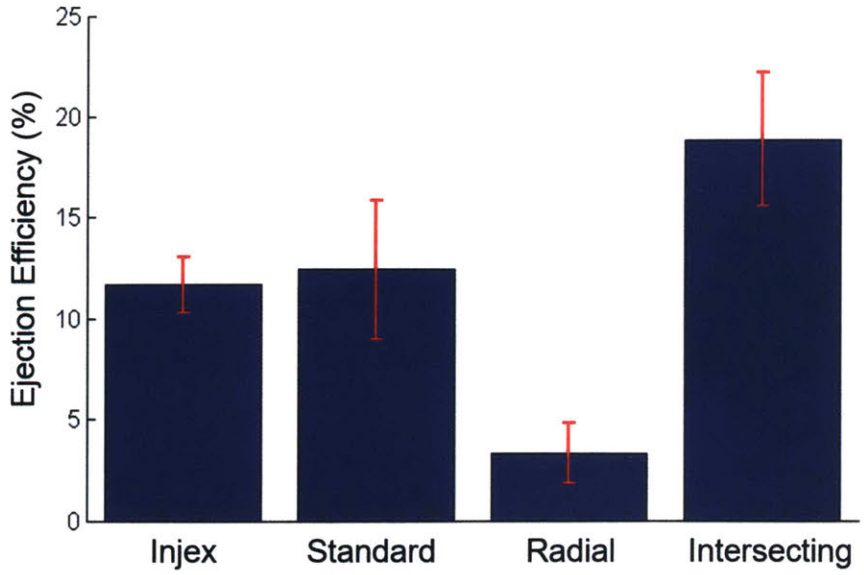

Figure 2-9: Ejection efficiencies of the studied ampoule configurations. Efficiency is calculated as the ratio between output mechanical kinetic energy of the jet and input electrical energy into the actuator. Figures taken from [4].

2.6 Summary

An ampoule platform that houses different nozzle inserts has been developed and demonstrated, enabling a concentration on the design and fabrication of the nozzle geometry instead of the entire ampoule. The ampoule and piston are rigid and therefore increase controllability and the manufacturing process consistently creates nozzles that produce collimated jets and do not deform over time. One nozzle is created to provide comparison with a commercial ampoule, and two other novel geometries are presented and demonstrated to have potential for intradermal and intratympanic membrane injections.

While three-dimensional geometry of the orifice plays a large role in jet creation, the presented work uses orifices of a constant circular cross-section. Subsequent chapters will entail understanding the effect of 3D orifice geometry on the jet's fluid flow, tissue injection, and efficiency and manufacturing methods to produce various three-dimensional nozzle geometries.

Chapter 3

Elements of Axisymmetric Nozzle Geometry

3.1 Introduction

Limitations of the Cylindrical Orifice

In Chapter 2, different nozzle geometries were developed by placing the nozzle orifice in different orientations and locations to increase needle-free injection modalities. In each different orientation, the nozzle orifice was created by micro-drilling and therefore the cylindrical orifice was always used as the nozzle shape. However, the cylindrical orifice may not be the ideal shape for needle-free injection.

First, consider the high-speed imaging of jets that issue from cylindrical orifice, such as that from the previously presented radial jets nozzle (Figure 3-1a). Recall that the exit geometry is circular and thus produces well-collimated jets. While collimated jets that travel at low speeds are relatively straight, dispersion is observed at high speeds (Figure 3-1b). As opposed to the dispersion of jets associated with the Injex ampoule where exit geometries were not axisymmetric, this type of dispersion is axisymmetric and is smaller in magnitude. It is conjectured that this dispersion is associated with an entirely different phenomenon, cavitation.

While cavitation has not been addressed in the needle-free injection space, it is

well studied in the research field of fuel injectors (Figure 3-2) [22, 23, 24]. Sou and colleagues established cavitation as a source of dispersion in the jets that issue from fuel injector nozzles, and demonstrated the positive relationship between the fraction of the total orifice length the cavitation region extends, L*, and the consequent dispersion angle of the jet [5]. In cavitation, geometries are developed to enhance cavitation, as cavitation helps to break up the jet, thus more finely dispersing fuel particles into the combustion chamber, and increasing the efficiency of combustion in the engine [23]. In needle-free injection however, the opposite is desirable; the more collimated a jet is, the greater the penetrating power. This provides motivation to find optimal geometries to minimize cavitation within the nozzle.

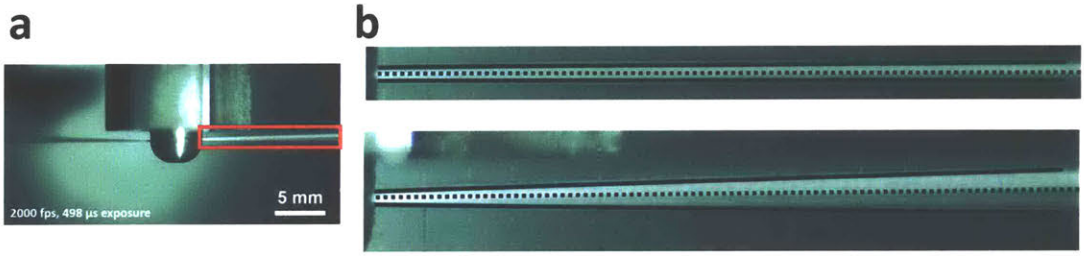

Figure 3-1: a) High-speed still of a collimated jet issuing from the radial jets nozzle. b) A close-up of the jet reveals a straight jet at lower speeds (top) and axisymmetric dispersion at high speeds (bottom).

Secondly, consider pipe flow, a well known topic of study and is used in higher education as a teaching model. The geometry of the pipe entrance plays a large role in the loss coefficient, K, of the pipe, because the entrance geometry dictates how much flow separation exists at the entrance (Figure 3-3). A large fillet geometry would enable a smooth transition and therefore little viscous losses, and a small fillet geometry would force a sharp transition of flow, flow separation, and therefore great viscous losses. Because the nozzle can be considered a convertor of static to kinetic energy, it is paramount to find a nozzle geometry to minimize viscous losses and thereby increase efficiency.

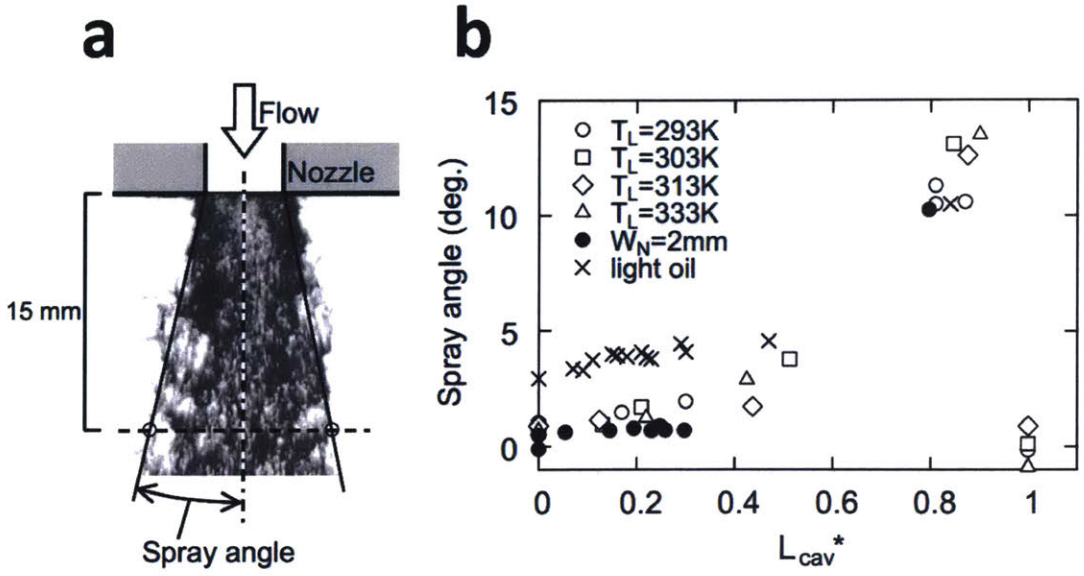

Figure 3-2: a) Dispersion in jets that issue from fuel injector nozzles is caused by cavitation within the injector nozzle. b) The farther the cavitation extends down the orifice, L*, the larger the spray angle of the jet. Figures taken from [5].

NFI Fluid Dynamics and Tissue Mechanics

A number of groups have addressed various aspects of the fluid dynamics and tissue mechanics in needle-free jet injection [25, 20, 21, 26, 27, 28, 29, 30, 31, 32, 33]. The literature can be summarized and grouped into four major groups based on its associated physical location in needle-free injection: the fluid flow within the interior of the nozzle, the fluid flow at the orifice exit, the tissue fracture, and dispersion through the bulk of the tissue (Figure 3-4). It is apparent that little work has studied the fluid flow within the interior of the nozzle.

No current work studies the effect of three dimensional nozzle geometry on injection. Portaro and colleagues did perform a three-dimensional CFD simulation where the orifice was considered a cylindrical orifice, but this geometry was kept as a constant [34, 35].

Secondly, it is common in the NFI experimentation to calculate the measured velocity of the jet based on the lossless Bernoulli equation [36, 3], which assumes no viscous losses in the nozzle. One study of NFI injection of viscous fluids [16]

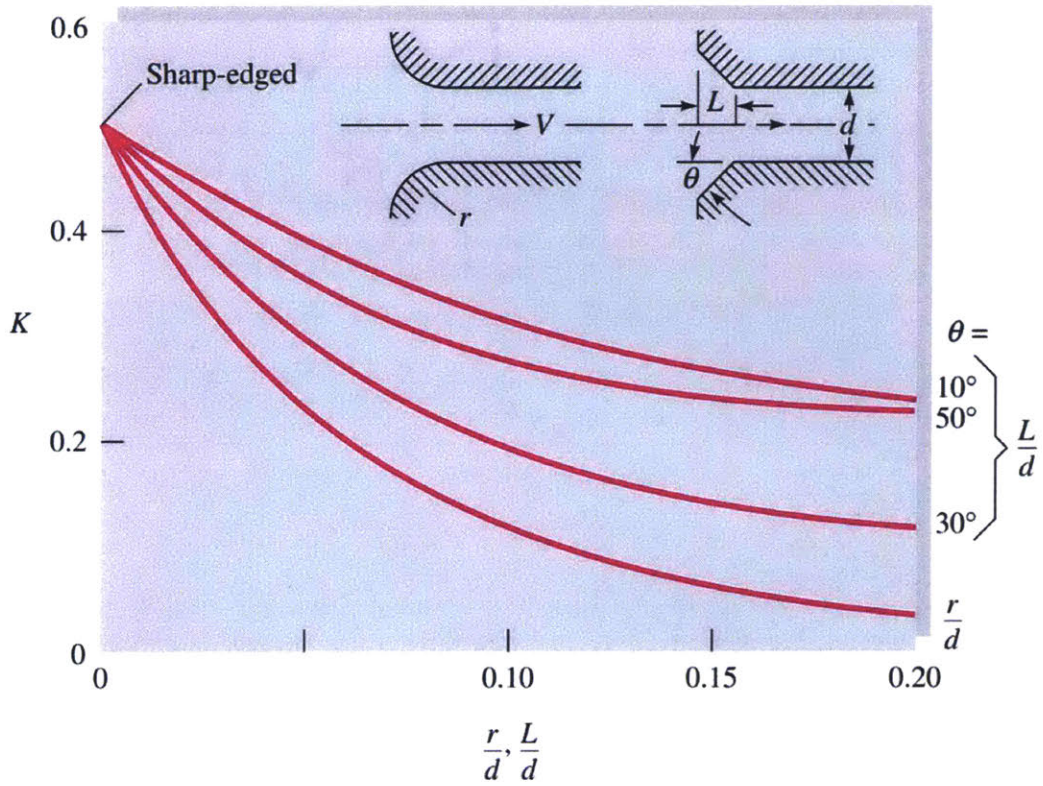

Figure 3-3: Pipe losses associated with pipe entrance geometry. Figures taken from [6].

does include loss in its full Bernoulli equation, but the loss component is a lumped parameter that is empirically determined. Simulation work in the NFI literature currently demonstrates an observable increase in energy dissipation with a decrease in nozzle diameter [34]. This work analyzed the most simple of geometries, the straight cylinder (sharp edges, no chamfer), and performed a parametric sweep with only one varied parameter–nozzle diameter. Because the ultimate goal of NFI is to develop a handheld injection device, an understanding of the efficiency of all processes is crucial. The more efficient each process is, the more portable and acceptable to the user the end product will be. No analysis has been done on the relation between 3D nozzle geometry and viscous losses to date.

Finally and most notably, cavitation within the nozzle is entirely unaddressed in the needle-free injection space.

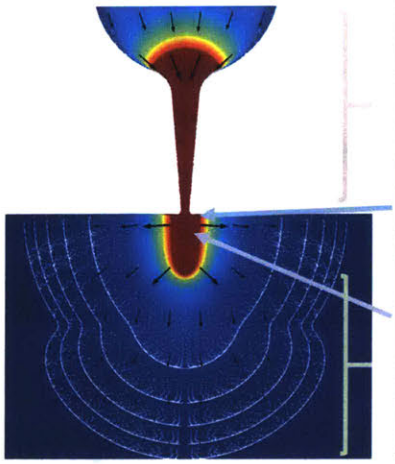

	Baker/Sanders	Chen	Nakayama	Williams	Barry	Shergold/Comley/Fleck	Schramm-Baxter/Mitragotri
3D geometry			o				
Viscous nozzle losses		o		o			
Cavitation							
Velocity field			o				
Nozzle diameter (1D geom)	o	o	o	o		o	o
Pressure at impact			o	o			
Pressure at fracture tip		o					o
Penetration depth		o					o
Porous flow					o	o	
Effect on compression/permeability					o		

Figure 3-4: An overview of the key issues of fluid dynamics and tissue mechanics accounted for in the needle-free injection space.

Thus, before finding the optimal shape for needle-free injection, it is important to first lay a working understanding of how nozzle geometry affects fluid flow. In this chapter, five major elements of the cylindrical orifice geometry are identified and their effects on fluid flow within the nozzle and exiting jet are studied.

3.2 Model Setup

A sample geometry and set of boundary conditions used for finite element analysis are shown in Figure 3-5a. The nozzle geometry consists of two primary regions: the cylindrical ampoule and nozzle orifice. The inlet (side a) condition is a uniform velocity that matches the piston's travel of 0.562 m/s. Side b is the axis of symmetry around which the rest of the 2D geometry is revolved to form the 3D geometry of the nozzle. A no-slip condition is imposed on the ampoule wall (side c), the orifice walls (sides d), and the outer face of the nozzle (side e). The nozzle ejects water into a semi-hemisphere reservoir of water, the boundary outlet of which is set at atmospheric pressure (curve f).

The cylinder will serve as the base geometry to start from, as it is the most

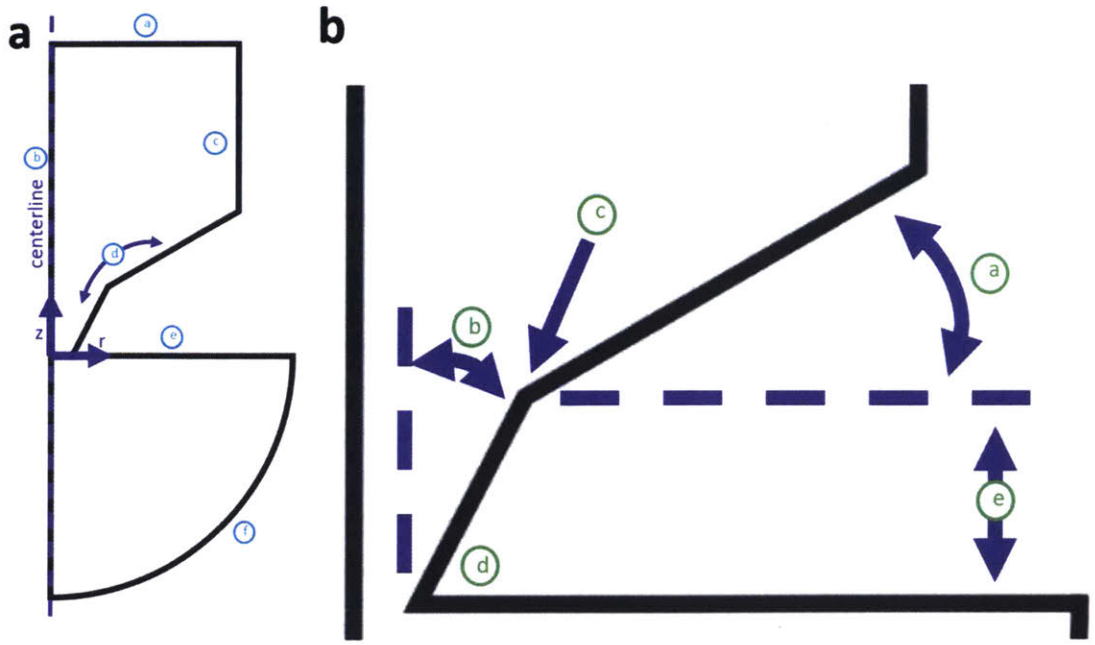

Figure 3-5: Set up with a) boundary conditions and b) elements of axisymmetric geometry for parametric study.

basic of nozzle geometries–the simple drilled hole. How flow is shaped from the ampoule diameter to the orifice diameter is of interest and thus motivates a study of the entrance geometry. Two elements are chosen, the entrance fillet and angle of entrance. Because the jet is formed at the exit and is of interest, the exit fillet will be studied. Additionally, it is currently unclear whether the nozzle should be short or long, and thus orifice length will be studied. Finally, how the fluid is accelerated to its final velocity is of interest, and thus the orifice angle will be studied.

In summary, the five elements of base geometry that will be studied are (Figure 3-5b): a) entrance angle, b) orifice angle, c) entrance fillet, d) exit fillet, and e) orifice length. Setting the values of all other elements as constant default values (Table 3.1), one element of the cylindrical geometry will be parametrically swept to discover how these elements of the geometry influence fluid flow.

Element of Geometry	Value
Entrance fillet	5 μm
Angle of entrance	0 or 60 degrees
Exit fillet	5 μm
Orifice length	1 mm
Orifice angle	0 degrees

Table 3.1: Default values for cylindrical geometry parametric studies.

3.3 Fluid Flow Analysis

In each of the parametric studies the flow will be analyzed by examining the overall mechanical efficiency of the nozzle, the cavitation pressure regions in the interior of the nozzle, and the velocity field at the exit.

Efficiency

The efficiency of a nozzle geometry is of great importance because one of the goals for NFI development is to be a handheld technology. Because the greater the losses the higher the power requirements and the larger the actuator and energy storage needs to be, there is great interest in making the nozzle as efficient as possible. One can view the nozzle to be an energy converter between static energy and kinetic energy and calculate the efficiency as such.

The total power, P(z), passing through a surface perpendicular to the nozzle axis at a point z along the axis can be expressed as the integration of the stagnation pressure with respect to the flow rate,

$$P(z) = \int_0^{R(z)} P_{stag}(z, r') v_a(z, r')(2\pi r') dr',$$

where v_a is the axial velocity, z is a distance along the nozzle axis, r is the radial distance from the axis, and R is the wall radius. P_{stag} is the stagnation pressure,

$$P_{stag}(z, r) = \frac{1}{2}\rho v(z, r)^2 + P_{stat}(z, r),$$

where ρ is the fluid density, v is the total velocity, and P_{stat} is the static pressure.

Then we define efficiency as the power flowing through the outlet divided by the power flowing through the inlet:

$$E = \frac{P(z_{outlet})}{P(z_{inlet})}.$$

Thus if there are viscous losses in the nozzle, the total power flowing into the inlet should be less than the total power flowing out of the outlet.

Cavitation

Upon examining the pressure fields of the flows in the interior of the nozzle, it is apparent that there often exist regions of pressure below atmospheric, particularly where streamlines bend drastically or expand. When a fluid experiences pressures below its vapor pressure, the fluid will experience a phase change and bubbles will form, a phenomenon called cavitation [37]. For example, in the cylindrical nozzle there exists a small region of very negative pressure starting at the sharp corner and a lesser negative pressure that occupies much of the orifice (Figure 3-6).

In the similar field of fuel injector nozzle design, cavitation within the nozzle is advantageous because the produced bubbles help break up the freestream jet, thereby dispersing the fuel particles for increased efficiency in combustion. Previous experimental work found that for the cylindrical geometry, varying amounts of cavitation caused jet spray angles that varied from nearly 0 to 15 degrees as measured from the nozzle axis [5].

In the context of needle-free injection however, cavitation is undesirable. The creation of bubbles implies of a loss of energy to the creation of liquid-gas interfaces. Secondly, an increase in jet dispersion leads to a decrease in penetration power and therefore penetration depth. Because different nozzle geometries create flows of different pressure fields, how regions of cavitation regions are changed by nozzle geometries is of interest.

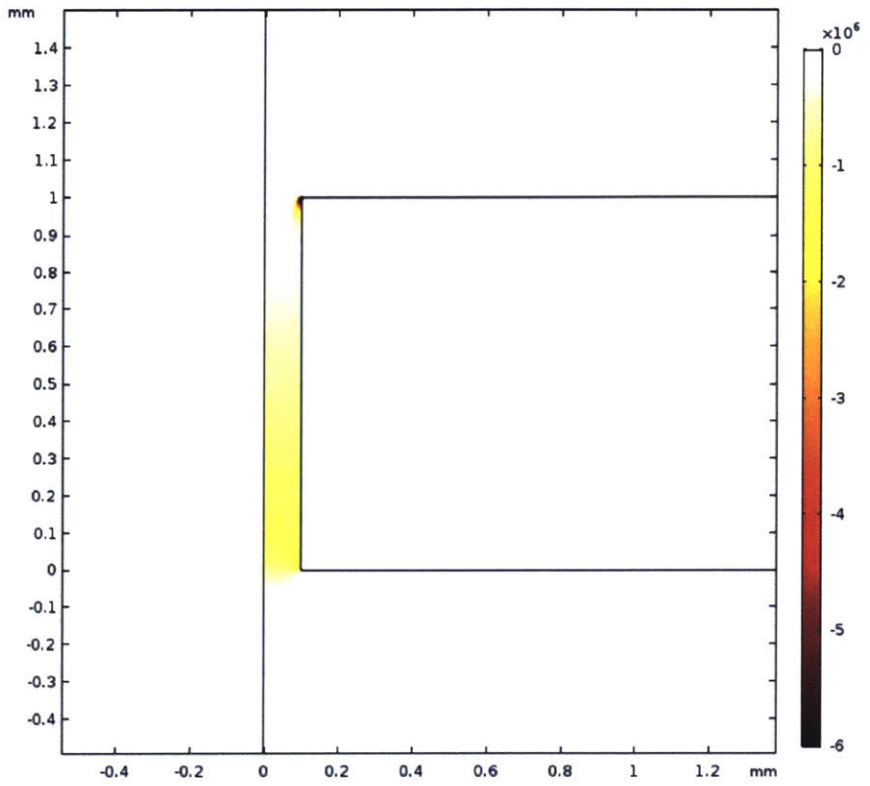

Figure 3-6: Pressure field of the orifice of a cylindrical nozzle. A large negative pressure exists at the sharp corner (z = 1 mm) and and larger downstream region of lesser negative pressure. The lower limit to the shown pressure is -6 MPa and the upper limit is 3.169 kPa, the vapor pressure of water at 25 °C.

Streamlines

Streamlines are a useful tool in fluid flow analysis because they reveal how the fluid will behave in the interior of the geometry. Flow expansion will be of particular note because of the associated viscous losses and the implied existence of negative pressure regions. Streamline plots will entail 20 streamlines that begin at points equally spaced across the inlet and track through the region of flow.

Velocity Field

The velocity field at the orifice exit is of interest because of its potential impact on jet injection. Velocity field of a jet influences jet break-up distance [38] and different

velocity profiles at the orifice exit also yield different mechanical powers at the orifice exit. For example, in laminar flow, poiseuille flow contains double the kinetic energy as plug flow of the same flow rate. In turbulent flow, the difference between plug flow and developed flow will be less prominent, but still of interest.

3.4 Entrance Fillet

Sharpness of transition between the ampoule radius and to the nozzle radius was alluded to in the previous section as a likely explanation for flow separation. Thus, the entrance fillet garners interest because it can give direct insight on the relation between flow separation and the geometric transition. For the study on entrance fillet, all elements of the geometry were kept constant except the entrance fillet, which was swept from 0.1 μm to 50 μm.

Streamlines

Figure 3-7 shows the regions of streamlines at the orifice entrance of each entrance fillet. Examination of the streamlines reveals that for fillets of radii 2 μm and less, the streamlines curve away from the wall at the orifice entrance, indicating a complete separation of the boundary layer at the entrance. For entrance fillet radii of 5 μm and more, flow separation is relatively insignificant, or at least unperceivable by inspection of streamlines.

Velocity Field

There exist two clear groups of axial velocity profiles (Figure 3-8a). The axial velocity profiles of larger entrance fillets (50 to 5 μm), exemplify the expected turbulent flow profile, with a slight curving upwards as the fillet radius decreases. There is a large change of curvature between the velocity profiles of fillet radii 5 μm and above versus fillet radii of 2 μm and below, when the boundary layer has completely separated (Figure 3-8). The second group of axial velocity profiles are curved upwards and

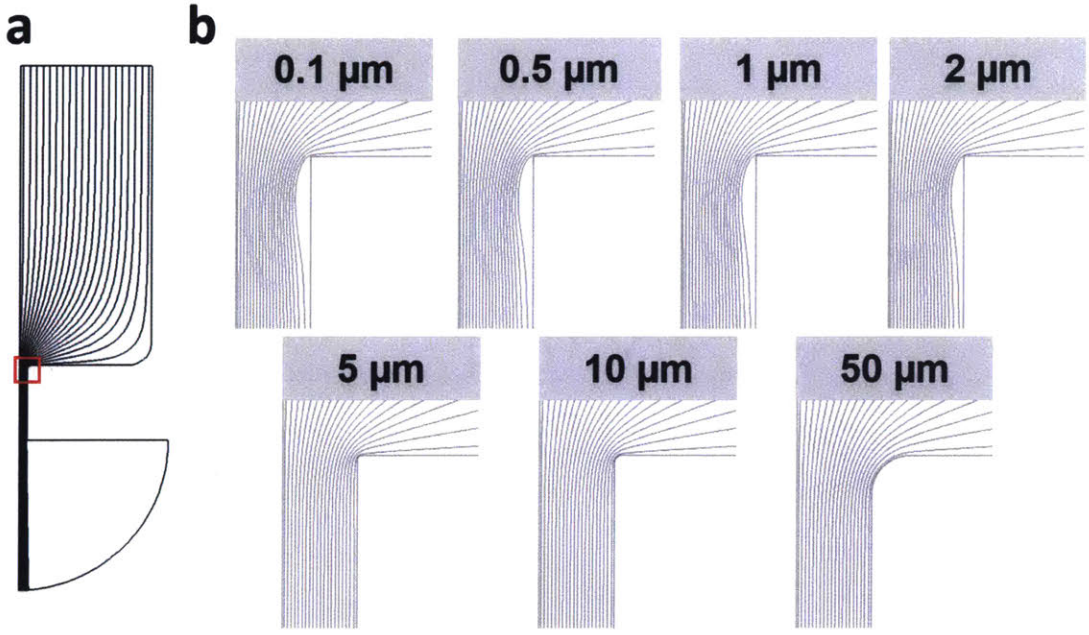

Figure 3-7: a) Streamlines of flow in geometries where entrance fillet is swept from 0.1 to 50 μm. The red box indicates the area of b) magnified streamline plots.

grow in curvature with decreasing fillet radius and increasing flow separation.

There is no significant difference in the curvature of radial velocity profiles, likely because the geometry at the exit is constant.

The maximum difference between all of axial velocity profiles and between all of the radial velocity profiles was slightly below 20% of each other.

Efficiency

Figure 3-9 shows the efficiencies of the fillet radius sweep. Flow separation for entrance fillets of 2 μm and less causes a subsequent flow expansion inducing significant viscous loss. Decreasing the entrance fillet radius decreases efficiency until a plateau of about 68%. As the fillet radius increases, the flow follows the wall more closely, decreasing viscous loss, and increasing efficiency until a plateau of 90%. There is a steep increase of efficiency between the fillet radii of 2 and 5 μm, when the flow no longer separates at the orifice entrance, thereby significantly decreasing viscous loss.

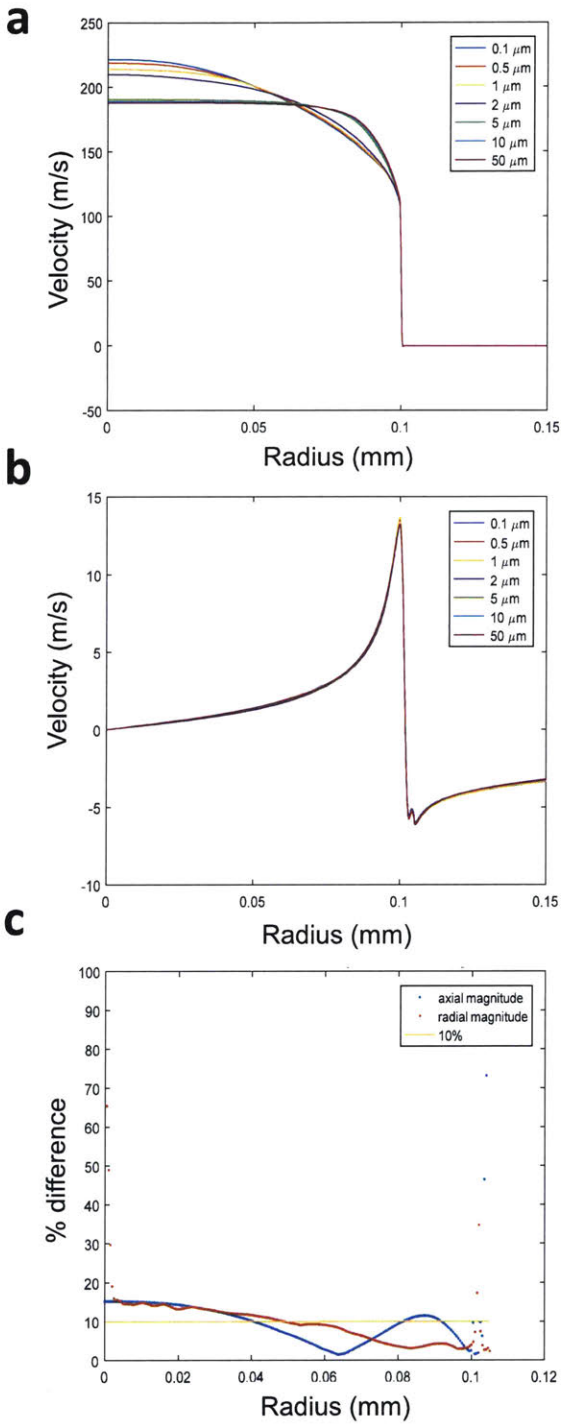

Figure 3-8: Velocity profiles of geometries where entrance fillet is swept: a) axial velocity magnitude, b) radial velocity, and 3) maximum % difference between the set of velocity profiles.

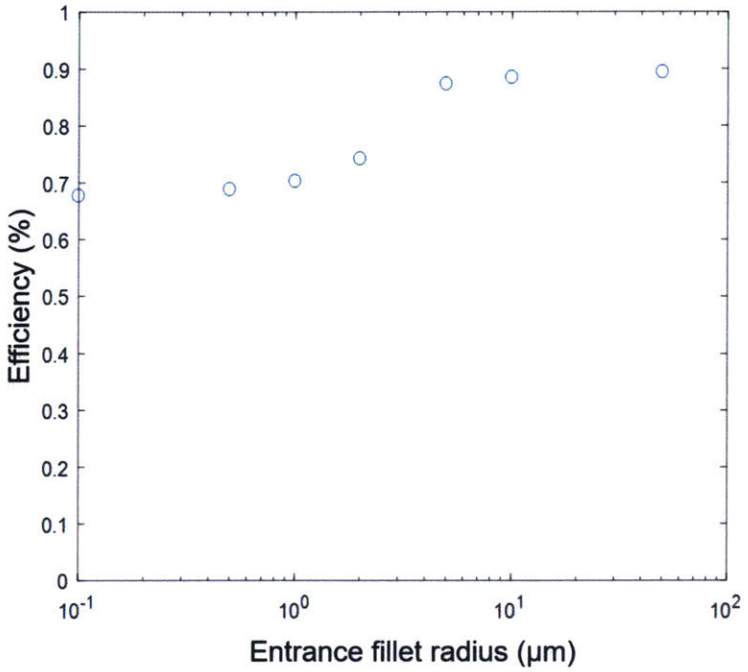

Figure 3-9: Mechanical efficiencies of geometries where entrance fillet is swept.

Cavitation

Large regions of negative pressure of similar structure and size exist for flows of entrance fillets of 2 μm and less (Figure 3-10). Because the flow separates from the wall and then experiences flow expansion, this region experiences large negative pressures. In geometries where flow separation is negligible, entrance fillets of 5 μm and more, the cavitation region is greatly decreased.

We make the preliminary conclusion that increasing the entrance fillet prevents flow separation at the orifice entrance, thereby decreasing viscous loss and the regions of cavitation pressure. A transition is sharp on the order of 5 μm is sufficient to cause flow separation. While flow separation causes the axial velocity profiles to peak at higher values, the efficiency is decreased significantly and unlikely to be advantageous.

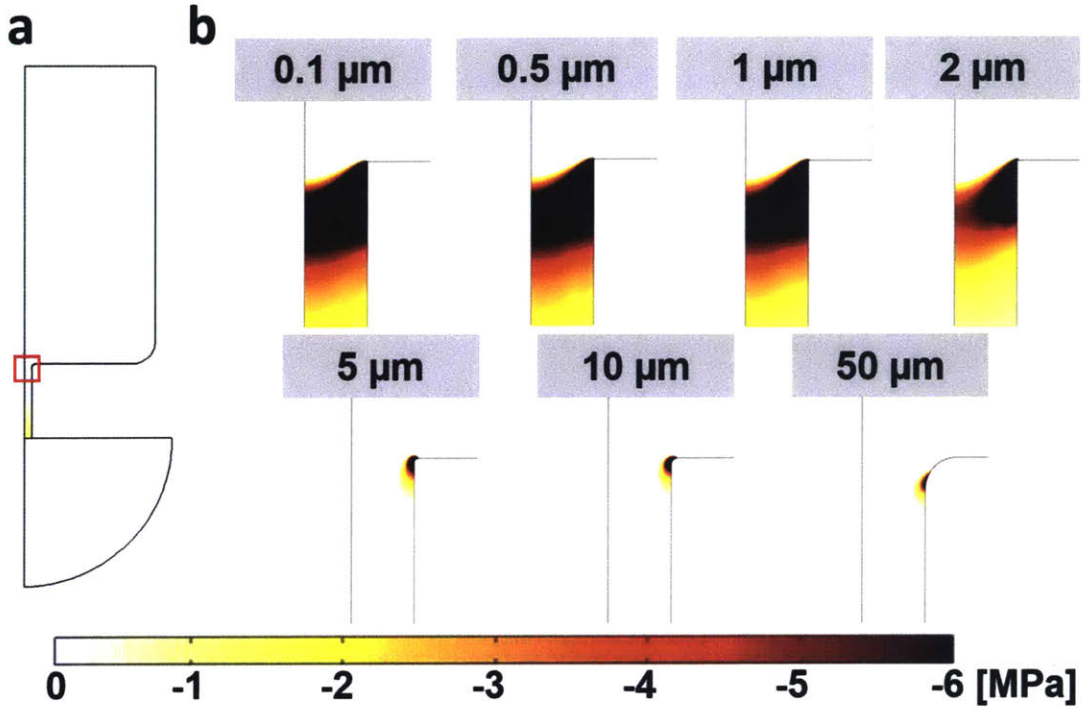

Figure 3-10: a) Cavitation pressure regions of geometries where entrance fillet is swept from 0.1 to 50 μm. The red box indicates the area of b) magnified plots.

3.5 Angle of Entrance

By control volume arguments, one may at first expect that upstream geometry has little effect on the behavior of flow at the orifice. The transition from the ampoule radius to the orifice radius was examined by varying the incline of transition. The angle of entrance (as measured from the plane perpendicular to the nozzle axis) was swept from 0 degrees to 60 degrees and its effect analyzed.

Streamlines

Figure 3-11 shows the regions of streamlines at the orifice entrance of each entrance fillet. Examination of the streamlines reveals a slight flow separation at 0 degrees that decreases as the entrance angle increases.

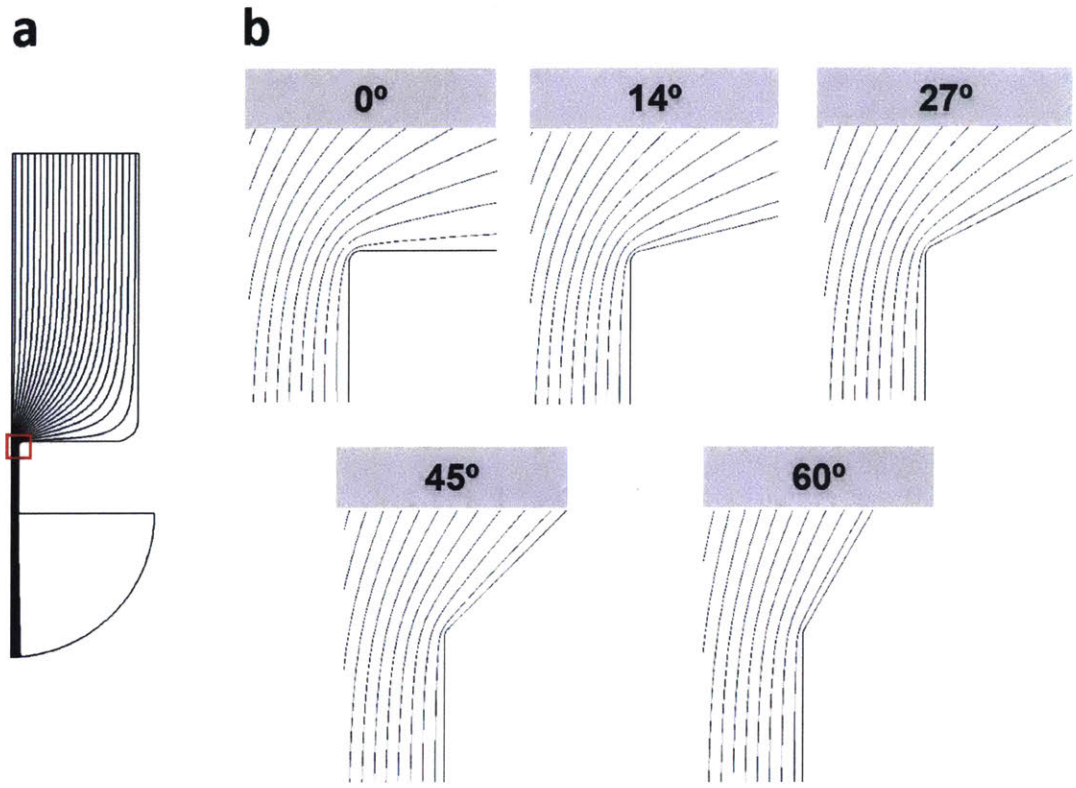

Figure 3-11: a) Streamlines of flow in geometries where entrance angle is swept from 0 to 60 degrees. The red box indicates the area of b) magnified streamline plots.

Velocity Field

While almost all of the axial velocity profiles of different angles of entrance are similar in curvature, the axial velocity profile of the geometry of 0 degrees entrance angle deviates slightly from the rest (Figure 3-12a). The 0 degrees angle of entrance may cause a contraction of flow that is sharp enough to induce minor flow separation. Thus, in parametric studies of other geometric elements where entrance geometry is not a focus of the study, the entrance angle is set at a non-zero angle (60 degrees) to avoid inducing flow separation at the orifice entrance.

Radial velocity profiles experience a large increase in velocity near the orifice edge (Figure 3-12b) because of the fluid flow around the exit fillet. The radial velocities are an order of magnitude lower than the axial velocities, two orders of magnitude lower in energy, and thus likely of secondary importance in injection performance.

There is little difference in both the axial and radial components of the velocity fields (Figure 3-12c). The maximum percent difference between all of axial velocity profiles remains within 5% of each other, similar to the maximum percent difference between all radial velocity profiles.

Efficiency

The flow in the nozzle loses at least 13% of its initial energy due to viscous loss (Figure 3-13). From 60 degrees to 14 degrees, there is only a 1.5% decrease in efficiency, but from 14 to 0 degrees there is a 2.4% decrease. This is likely also due to the flow beginning to separate at the orifice entrance.

Cavitation

Increasing the entrance angle causes a slight decrease of the region of cavitation near the orifice entrance (Figure 3-14). Because the contraction of flow is more gradual with increasing entrance angle, less of the boundary layer separates from the wall, leading to smaller regions of negative pressure.

We make the preliminary conclusion that the sharpness of transition from ampoule diameter to orifice diameter will dictate whether there is flow separation or whether the flow remains connected to the nozzle walls as it enters the contraction. If there is no flow separation however, upstream geometry may have little effect on the velocity profile, efficiency, and cavitation.

3.6 Exit Fillet

Recall that flows in geometries of non-zero entrance angle or of exit fillets of sufficiently large radii differed little in velocity field and efficiency. In situations where flow separation and significant regions of cavitating pressure do not occur, control volume arguments can be used to argue that geometry significantly upstream from the orifice exit do not substantially influence the flow at the orifice exit. The geometry near

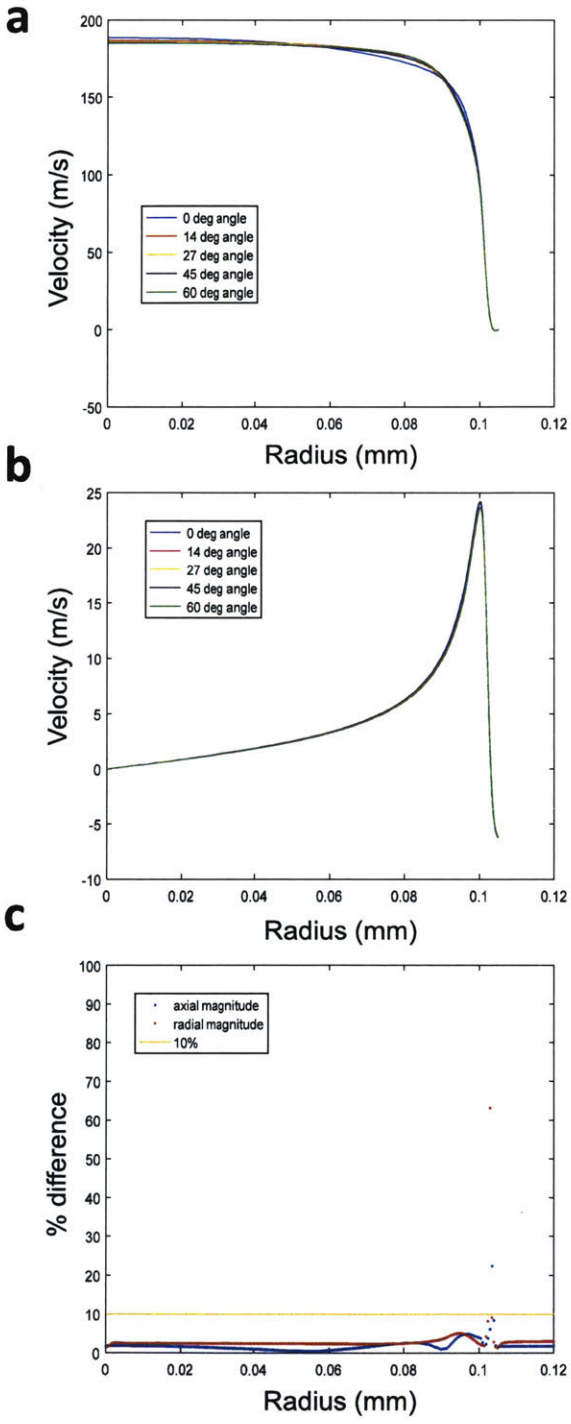

Figure 3-12: Velocity profiles of geometries where entrance angle is swept: a) axial velocity magnitude, b) radial velocity, and 3) maximum % difference between the set of velocity profiles.

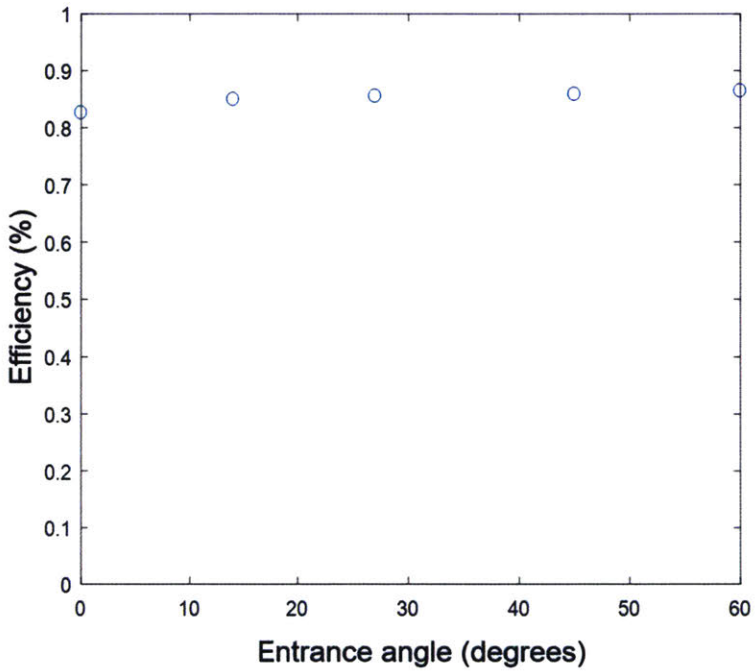

Figure 3-13: Mechanical efficiencies of geometries where entrance angle is swept.

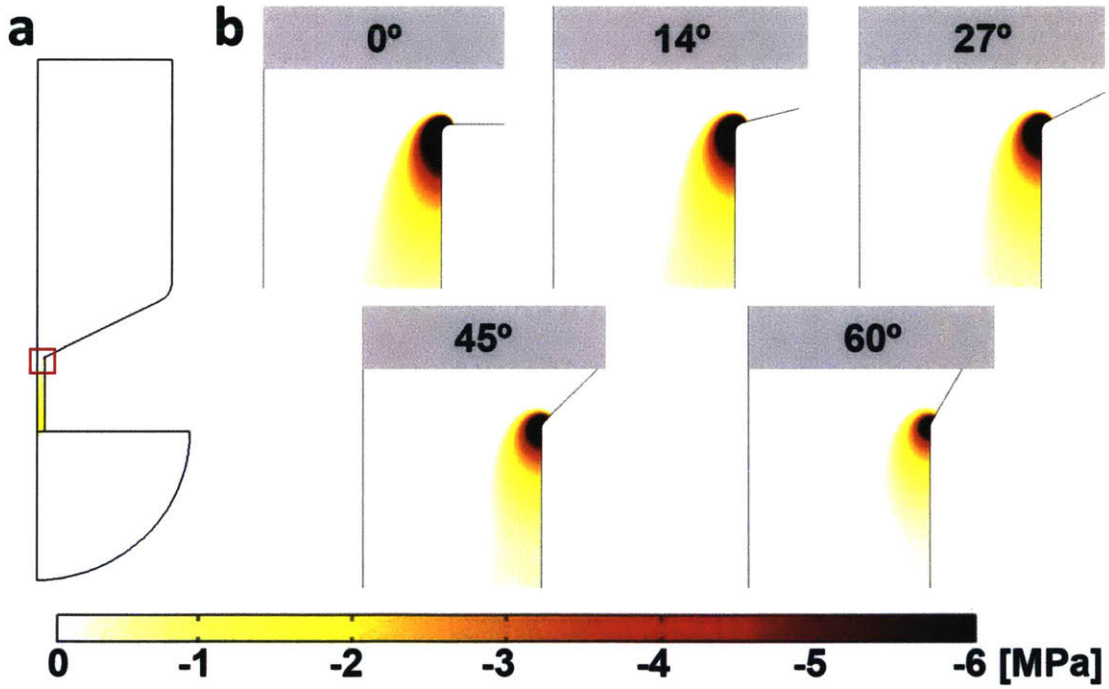

Figure 3-14: a) Cavitation pressure regions of geometries where entrance angle is swept from 0 to 60 degrees. The red box indicates the area of b) magnified plots.

the orifice exit however should always be influential. Exit geometry is examined by a study on the influence of exit fillet size on the flow. Because flow separation at the orifice entrance is not of interest, the entrance angle was set at 60 degrees instead of 0 degrees. All elements of the geometry were kept constant except the exit fillet, which was swept from 0.1 to 50 μm.

Streamlines

Figure 3-15 shows the streamlines at the orifice exit of each exit fillet. Examination of the streamlines reveals that starting at exit fillets of radii 2 μm and less, the outer streamlines begin to curve outwards at the orifice exit, indicating flow expansion. For entrance fillet radii of 1 μm and less, flow expansion is relatively insignificant, or at least unperceivable by inspection of streamlines.

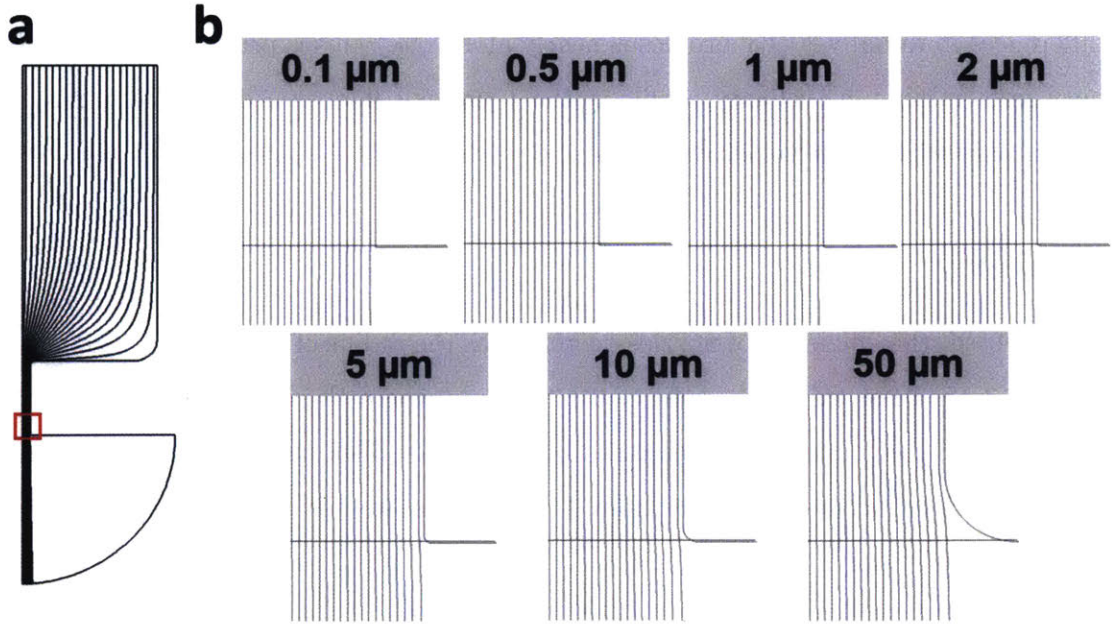

Figure 3-15: a) Streamlines of flow in geometries where exit fillet is swept from 0.1 to 50 μm. The red box indicates the area of b) magnified streamline plots.

Velocity Field

The axial velocity profiles become flatter and the profile's decrease from the velocity at the center to the orifice wall becomes more gradual as the fillet radius increases. The general curvature is maintained through the entire sweep.

The radial velocity profiles changes in both magnitude and curvature when exit fillet radius is changed. For smaller exit fillets, the radial velocity grows slightly negative further from the axis, then sharply increases to a positive radial velocity at the nozzle radius. The larger the fillet radii, the less negative the overall radial velocity, with the profile of the 0.5 μm fillet radius with the least radial flow. In exit fillets of radii greater than 1 μm, flow separation occurs before the flow reaches the nozzle exit (Figure 3-16b), leading to a radial velocity that is positive at radii less than the nozzle radius and negative at radial distances greater than the nozzle radius.

Different exit fillet geometries do not significantly influence axial velocity profiles but do greatly influence radial velocity profiles (Figure 3-16c). The maximum difference in axial velocity profiles remains around less than 10% whereas the maximum differences in radial velocity profiles is nearly at 1000%. This is primarily because the near-zero "minimum" velocity profile of the 1 μm exit fillet is used as the minimum to compare with other velocity profiles.

Efficiency

As expected, the efficiency of nozzles decreases as the radius of the exit fillet increases (Figure 3-17). For exit fillet radii of 0.1 to 1 μm where there is no significant flow expansion, the efficiency only decreases by 0.2%. For fillet radii greater than 1 μm, flow separation occurs and thus from 1 to 50 μm, we see a decrease of 3.6% in mechanical efficiency.

Cavitation

For small exit fillets, regions of cavitation pressure are limited to the region near the orifice entrance and are dependent on the orifice entrance geometry (Figure 3-18).

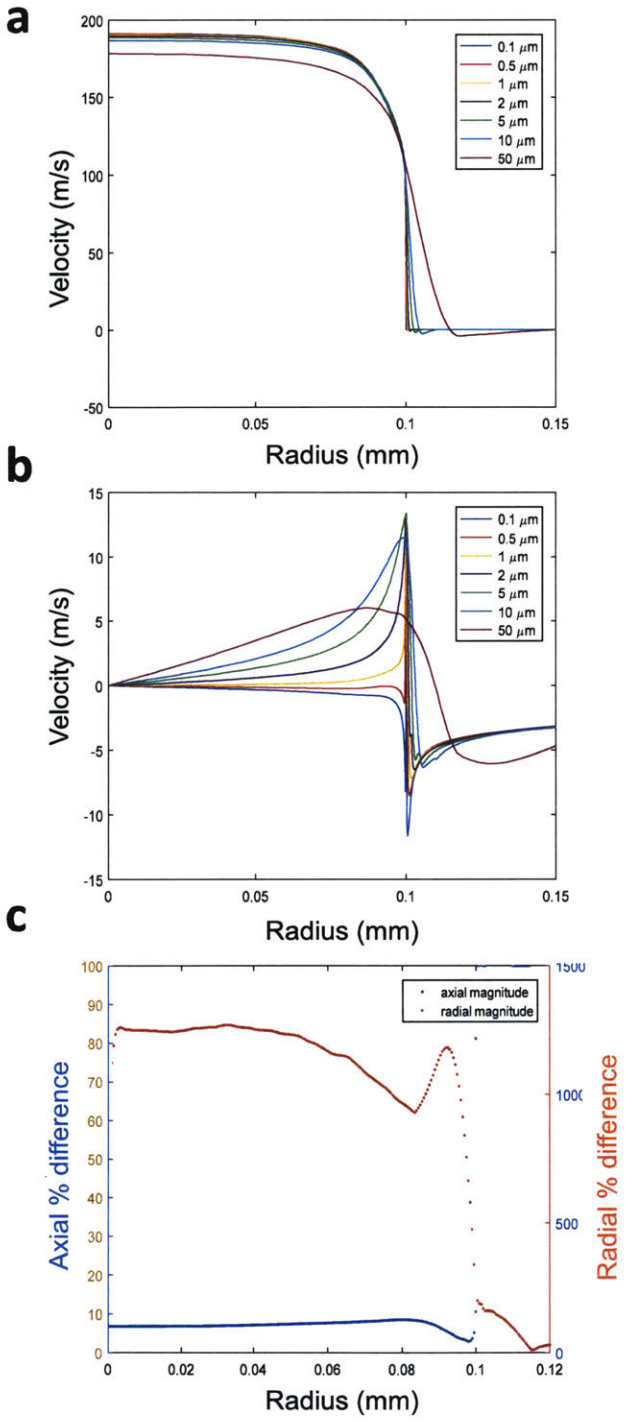

Figure 3-16: Velocity profiles of geometries of different exit fillet radii: a) axial velocity, b) radial velocity, and 3) maximum % difference between the set of velocity profiles.

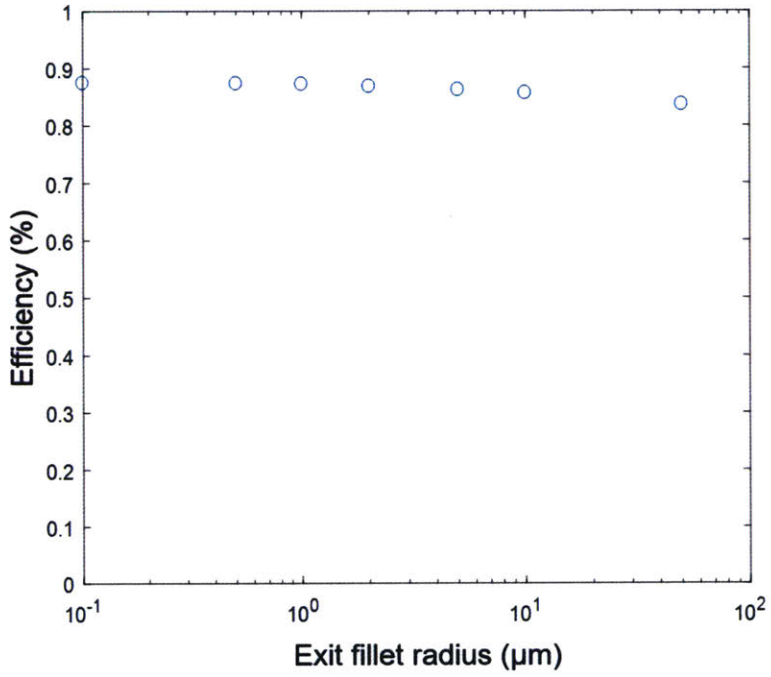

Figure 3-17: Mechanical efficiencies of geometries where exit fillet radius is swept.

When the exit fillet increases to a point to induce flow expansion at the exit, the regions of cavitation pressure begins to increase in magnitude and size, starting at the 2 μm exit fillet increasing until the maximum exit fillet geometry of 50 μm radius.

We make the preliminary conclusion that the smaller the exit fillet the higher axial velocity which should be advantageous. An exit fillet that is sufficiently large will cause flow separation upstream from the orifice exit. This flow separation does not significantly affect viscous loss but does significantly increase the regions of cavitation pressure.

3.7 Orifice Length

Because flow separation at the orifice entrance is not of interest, the entrance angle was set at 60 degrees instead of 0 degrees. All elements of the geometry were kept constant except the orifice length, which was swept from 0.0625 to 2 mm.

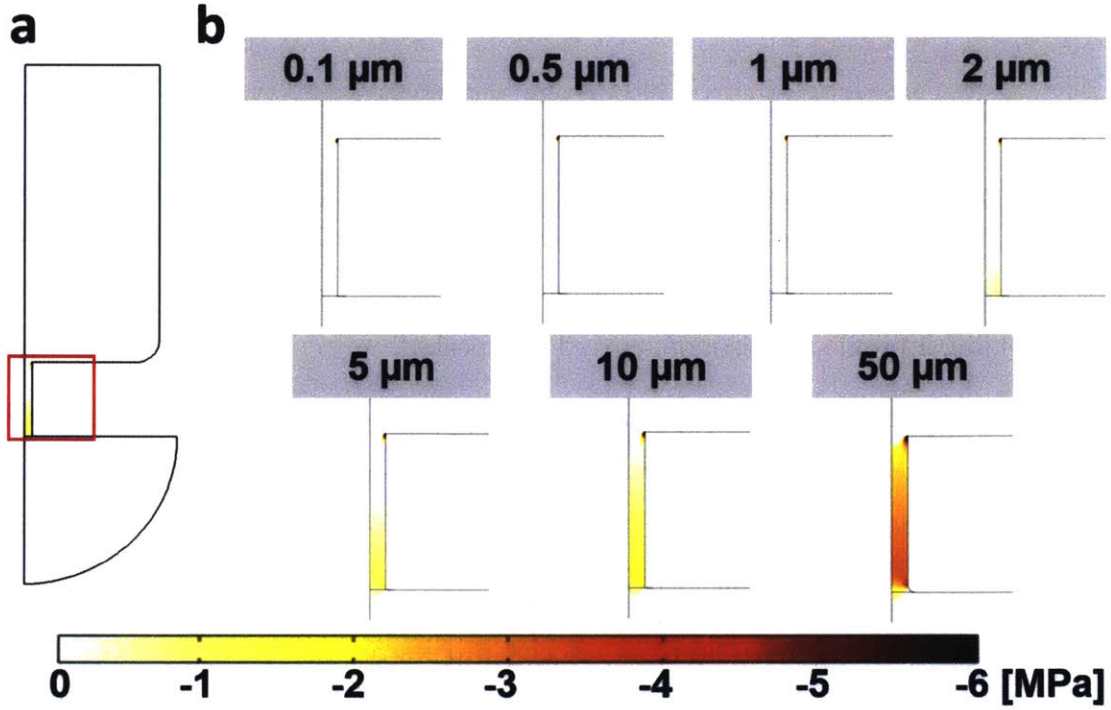

Figure 3-18: a) Cavitation pressure regions of geometries where exit fillet is swept from 0.1 to 50 μm. The red box indicates the area of b) magnified plots.

Streamlines

Streamlines within the nozzle interior were lengthened but did not change in curvature with changing orifice length because neither entrance nor exit fillet geometries changed (Figure 3-19).

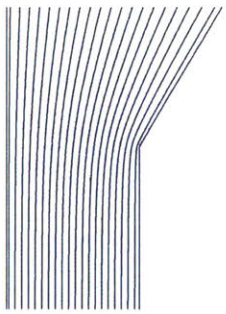

Figure 3-19: Representative image of streamlines at the orifice entrance for the orifice length sweep.

Velocity Profile

The axial velocity profiles become more arched and the peak velocity increases as orifice length is increased (Figure 3-20a). The entrance geometry is kept constant and thus the change is not due to flow separation. The boundary layers at the walls of nozzles of greater orifice lengths grow further, causing a flow that is more developed and yielding a profile that is more curved and peaked.

The radial velocity profiles maintain the same general curvature as the orifice length is swept. The velocity profile of the 0.0625 mm is slightly different in curvature because the 5 μm fillet is no longer "small" in comparison to the orifice length and the flow can no longer be considered pipe flow.

The maximum difference in axial velocity profiles remains decreases from about 15% whereas the maximum differences in radial velocity profiles is nearly at 1000%. This is primarily because the near-zero "minimum" velocity profile of the 0.0625 mm orifice length is used as the minimum to compare with other velocity profiles.

Efficiency

The Darcy-Weisbach equation expresses pressure loss due to viscous losses in the pipe of turbulent flow [6]:

$$\frac{\Delta p}{L} = f_D \frac{\rho}{2} \frac{\langle v \rangle^2}{D},$$

where Δp is the pressure drop, L is the length of the pipe, f_D is the Darcy friction factor, ρ is the density of the fluid, v is the average velocity of the bulk, and D is the diameter. According to Darcy-Weisbach, pressure drop along the pipe directly scales linearly with the length along the pipe. This is linear decrease is generally observed in the efficiency (Figure 3-21) as well.

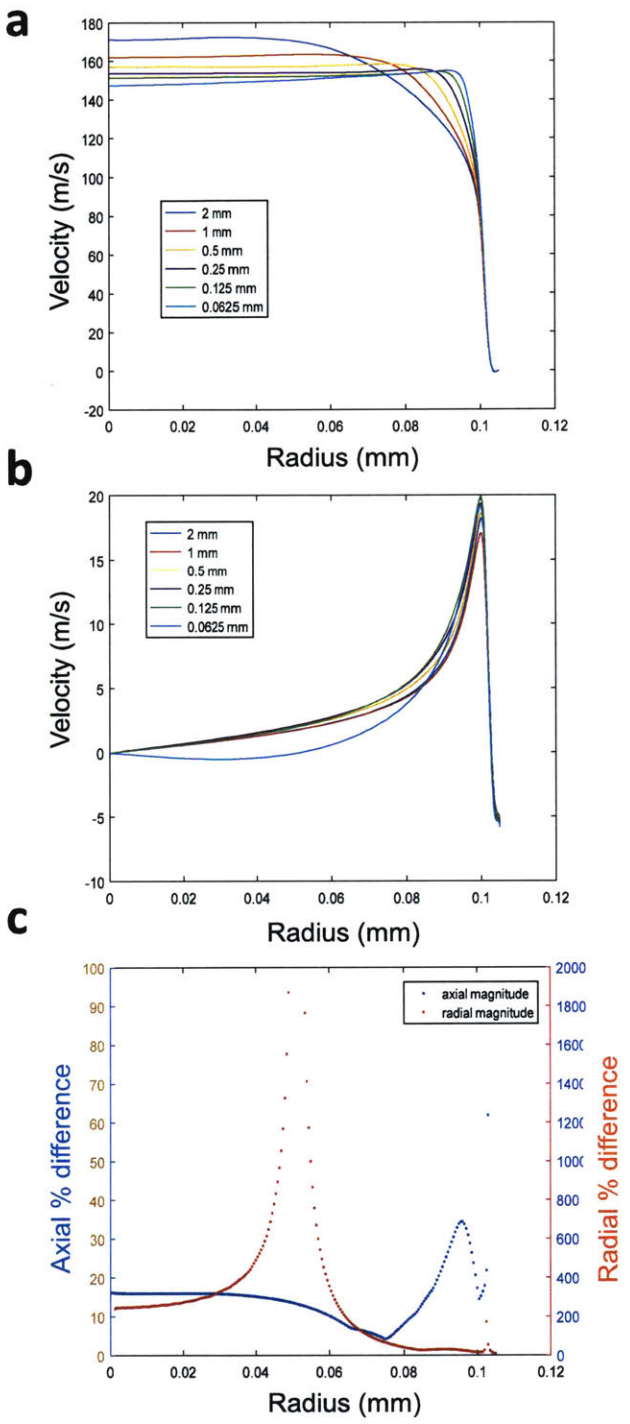

Figure 3-20: Velocity profiles of geometries of different orifice lengths: a) axial velocity, b) radial velocity, and 3) maximum % difference between the set of velocity profiles.

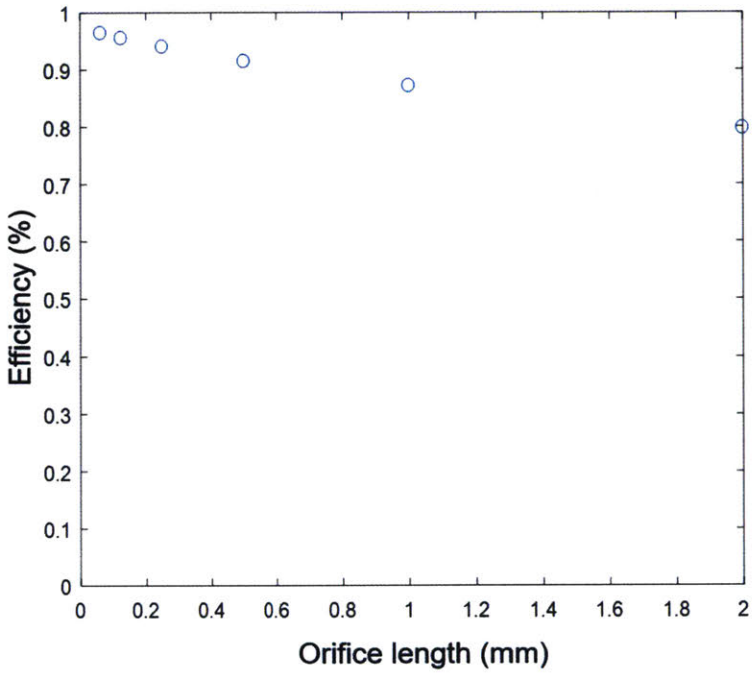

Figure 3-21: Mechanical efficiencies of geometries of different orifice lengths.

Cavitation

Because orifice entrance and exit geometry are not changed, the streamlines of flow do not change in contraction or expansion. Thus, the regions of cavitation pressure do not change in magnitude or contour, but do increase in length as the orifice length increases (Figure 3-22a). The area of greatest negative pressure at the orifice entrance remains the same across all geometries as the orifice entrance geometry is constant (Figure 3-22b).

We make the preliminary conclusion that increasing the orifice length increases the peak of the axial velocity profile and therefore the kinetic energy of the jet. However, the overall mechanical efficiency of the nozzle decreases with increasing orifice length. Whether more developed flow is advantageous for needle-free injection is unclear at this point and will thus be examined in Chapter 3.

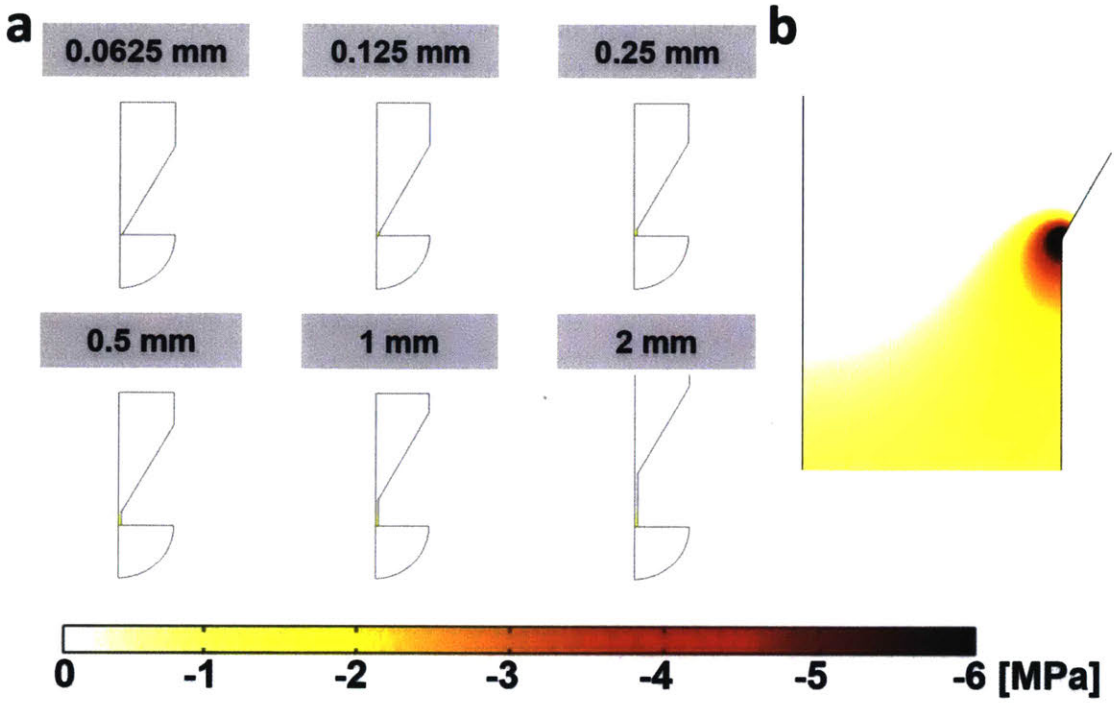

Figure 3-22: a) Cavitation pressure regions of geometries where entrance fillet is swept from 0.1 to 50 μm. b) Representative pressure plot at the orifice entrance.

3.8 Orifice Angle

Having established an understanding of how entrance geometries, exit geometries, and orifice length influence flow, it is now appropriate to examine the effect of the orifice angle on fluid flow. A change in orifice angle changes all three of the aforementioned elements of the flow. For the study on orifice angle, the orifice geometry was changed from the initial cylinder to steeper and steeper conical geometries. All elements of the geometry were kept constant except the orifice angle (as measured from the nozzle axis), which was swept from 0 degrees to 60 degrees.

Streamlines

Examination of the streamlines at the orifice exit reveals a subtle but important point (Figure 3-23). In the cylindrical geometry, there is a slight expansion of flow at the exit due to flow curving around the exit fillet. Because infinitely sharp corners do

not exist and the exit fillet will always be something non-zero, an expansion of flow is inevitable when the walls are straight at the exit. However, the streamlines of non-zero orifice angle continue to travel towards the axis implying the flow does not expand but contracts just beyond the exit. The implications of this difference are explained in the following sections.

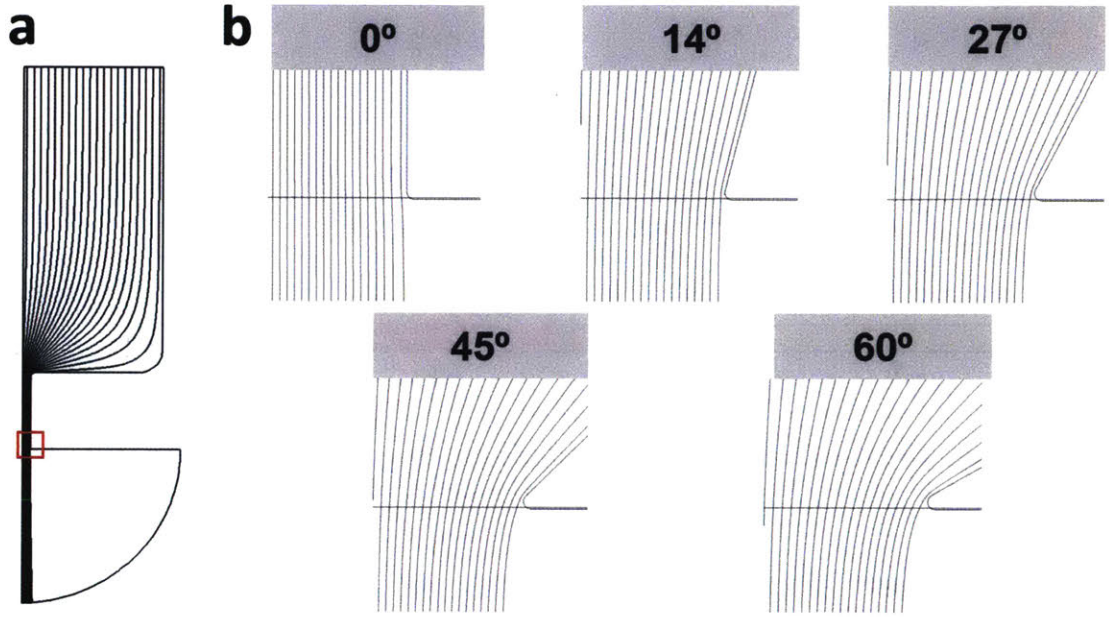

Figure 3-23: a) Streamlines of flow in geometries where orifice angle is swept from 0 to 60 degrees. The red box indicates the area of b) magnified streamline plots.

Velocity Field

The curvature of the axial velocity profiles of geometries with non-zero orifice angle differ significantly from that of the standard cylindrical orifice (zero degrees) (Figure 3-24a). In geometries with non-zero orifice angles, the axial velocity of non-zero orifice angles increase as radius increases, instead of a steady decrease from a maximum at the center. The greater the orifice angle, the flatter and more spread out the axial velocity profile.

Similarly, the curvature of radial velocity profiles of non-zero orifice angles also differ significantly from that of the standard cylindrical orifice (Figure 3-24b). Because

flow is directed along the angled orifice walls, flow is directed towards the axis at the exit, resulting in a radial profile that is primarily negative. In the radial velocity profile of the 14 degree orifice angle, we can see most clearly the interplay between the effects of the orifice angle and the 5 μm fillet: the flow is first radially negative then spikes up near the end. As the the orifice angle increases, the velocity profile becomes more negative and the positive spike due to the exit fillet is less prominent.

There are significant differences in both the axial and radial components of the velocity fields (Figure 3-24c). Because increasing the orifice angle slightly widened the effective radius of the orifice exit, we ignore the % difference beyond about 100 μm. The maximum % difference between all of axial velocity profiles remains at about 30% of each other, whereas the maximum % difference between all radial velocity profiles remains at about 100%.

Efficiency

The efficiencies of non-zero orifice angled geometries are significantly higher than that of the cylindrical geometry (Figure 3-25). From 60 degrees to 14 degrees, there is only a 0.8% decrease in efficiency, but from 14 to 0 degrees there is a 14.4% decrease. There are three factors responsible in increasing the efficiency. First, the flow in geometries with non-zero orifice angles do not separate from the wall at the entrance transition. Second, the greater the orifice angle, the greater the angle of effective diameter of the orifice. Because pressure drop in pipes scales inversely with the diameter, the greater the angle the greater the effective diameter of the orifice, the lower the pressure drop across the length of the nozzle, and the higher the efficiency. Thirdly, the flow does not expand at the exit and therefore decreases viscous losses.

Cavitation

Because the flow does not expand in any part of the interior of nozzle in geometries of non-zero orifice angle, regions of cavitation pressure are drastically decreased (Figure 3-26).

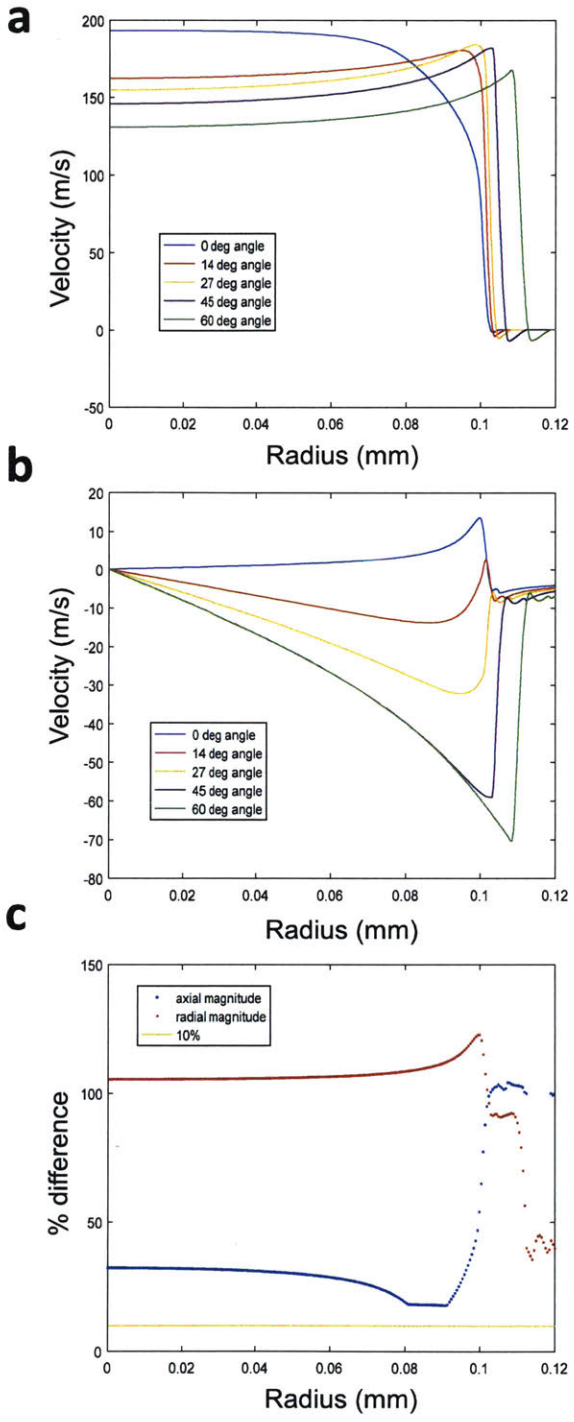

Figure 3-24: Velocity profiles of geometries where orifice angle is swept: a) axial velocity magnitude, b) radial velocity, and 3) maximum % difference between the set of velocity profiles.

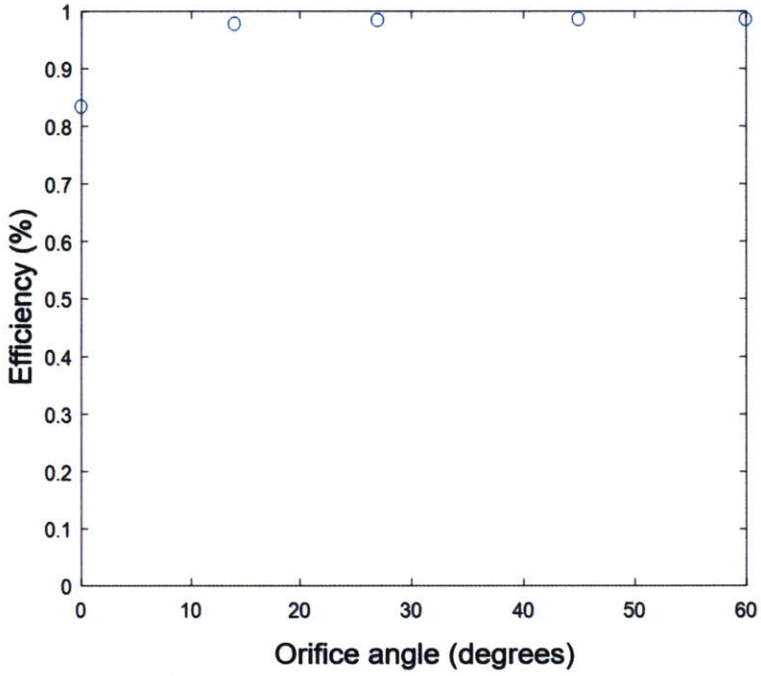

Figure 3-25: Mechanical efficiencies of geometries where orifice angle is swept.

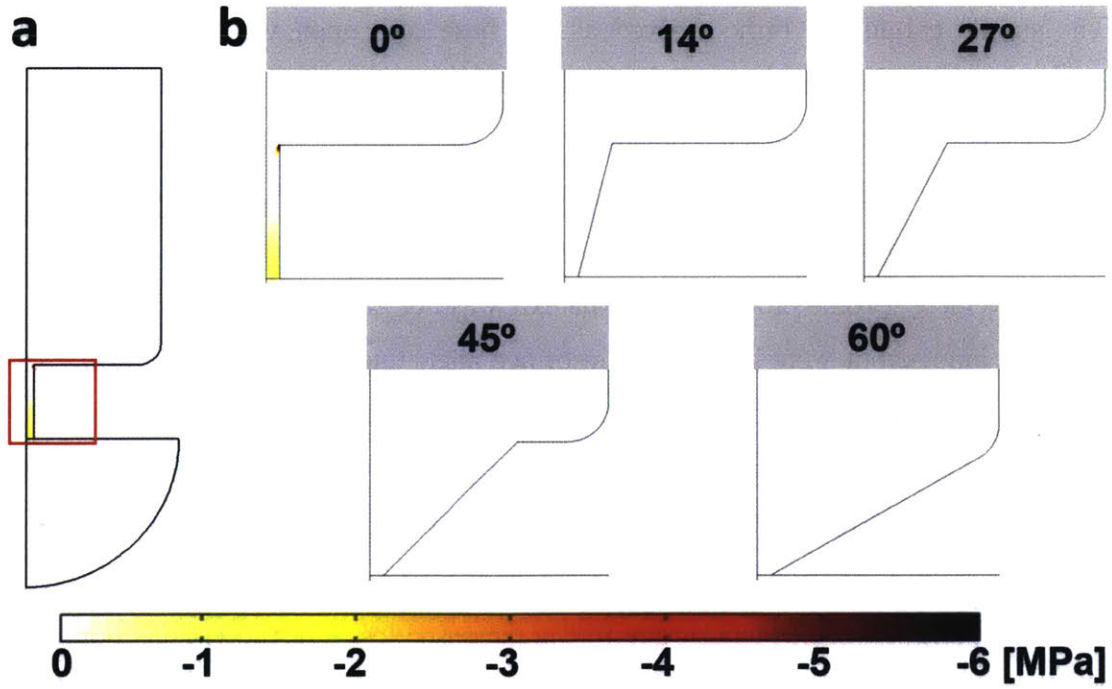

Figure 3-26: a) Cavitation pressure regions of geometries where orifice angle is swept from 0 to 60 degrees. The red box indicates the area of b) magnified plots.

This is the only set of geometries where radial velocity profiles of primarily negative values exist. If the primary goal of the nozzle is to convert static pressure to axial momentum, large orifice angles are not advantageous because of their smaller axial velocity profiles. A non-zero orifice angle is still advantageous however; because of the inward radial momentum at the exit, the jet does not expand at the exit. Because non-zero orifice angle eliminate flow expansion, the area of cavitation pressure near the orifice exit is drastically decreased and efficiency is increased because of decreased viscous loss.

Therefore, we make the preliminary conclusion that the optimal angle at the orifice exit is likely the smallest orifice angle such that flow contracts at the exit, given the size of the given exit fillet.

3.9 Summary

The simple cylindrical orifice served as the base case upon which five geometric changes were made: entrance angle, orifice angle, entrance fillet, exit fillet, and orifice length. These five elements of the geometry were parametrically swept and their influence on fluid flow were analyzed, namely: mechanical efficiency of the nozzle, cavitation pressure regions, streamlines, and velocity fields at the orifice exit.

The velocity profile of a nozzle at the exit was not greatly affected by changes in entrance angles, but were by changes in orifice angle due to directing the flow itself, changes in entrance fillet because of flow separation, and changes in exit fillet, and changes in orifice length because of how close the flow was to being fully developed.

The nozzle efficiency was not greatly influenced by changes in entrance angle or orifice angle, but was influenced by the entrance fillet and the exit fillet due to flow separation and the orifice length due to the increased losses of the viscous boundary layer.

The amount of cavitation was not greatly influenced by changes in orifice angle or orifice length, moderately influenced by entrance angle and significantly by the entrance fillet and exit fillet because these changes greatly changed the pressure field

and direction of the streamlines.

From these five parametric studies, four summary insights for the nozzle geometry design are drawn: A transition from ampoule diameter to the orifice diameter that is too sharp (<5 μm) causes flow separation at the orifice entrance, necessitating flow expansion in the interior of the nozzle, and thereby inducing increased viscous loss and largened regions of cavitation. Decreasing the size of the exit fillet decreases the opportunity for flow separation just upstream of the orifice exit, significantly decreasing the region of cavitation pressure near the orifice exit. The shorter the orifice length, the less energy loss to the viscous boundary layer, but also the flatter the velocity profile. A non-zero orifice angle prevents flow expansion at the exit, decreasing viscous loss and the region of cavitation pressure near the orifice exit, but increasing orifice angle also increases the radial velocity and decreases the axial velocity at the exit.

These insights will guide principles in nozzle shape optimization in the next chapter.

Chapter 4

Nozzle Shape Optimization

4.1 Introduction

In Chapter 3, the relationships between nozzle geometry and different aspects of fluid flow was established. These insights will inform the optimization of the nozzle shape for needle-free injection.

Shape optimization for fluids is a field of active research that lies at the intersection of fluid dynamics and computational and applied mathematics [39]. For the sake of this work, shape optimization can be classified into three general areas (Figure 4-1): 1) an objective function that encapsulates the criteria of what to optimize for, 2) a class of shapes that capture the elements and constraints of geometry that influence the objective function, and 3) a choice of an optimization method that is cost-effective and yields a solution of sufficient specificity.

4.2 Objective Function

The nozzle can be considered as the creator of the jet to carry out tissue injection and a converter of energy. To find the optimal shape of the nozzle therefore, it is necessary to lay a framework of metrics to capture these different aspects.

The first metric to take into account is a jet's ability to penetrate tissue of a given nozzle shape. However, penetration power is difficult to simulate or quantify. Velocity

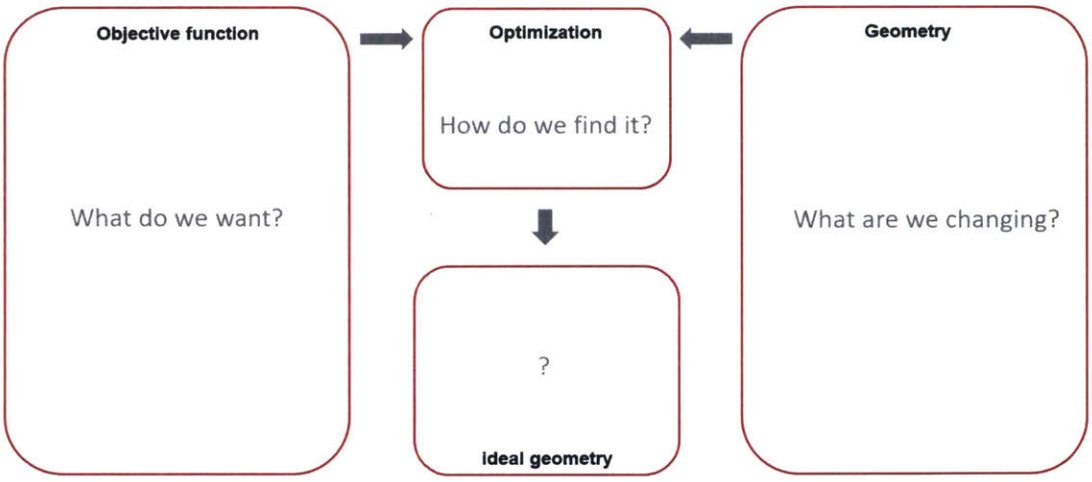

Figure 4-1: Three general areas of shape optimization - objective function, geometry space, and optimization method.

field and cavitation are possible metrics for use in the objective function. Previous work in the needle-free injection space generally took into account the velocity averaged across the entire surface area of the nozzle orifice, otherwise known as the "bulk velocity". However, it is possible that jets of different velocity profiles across the orifice diameter could differ in ability to penetrate tissue. Secondly, because cavitation increases the dispersion of a jet and therefore decreases the penetration power of the jet, cavitation is also a promising metric for jet penetration.

The cost of a jet of a given nozzle shape is the second overarching metric. Because jet injectors are developed for hand-held, portable use, the less energy it requires to produce a jet, the more miniaturized the device can be.

4.2.1 Fully Developed Flow

Penetration Ability of Developing Flow

We hypothesize that given the same overall flow rate, a flow that is more fully developed has higher penetration power than plug flow. While it is straightforward to analyze the velocity field at the orifice exit through CFD simulations, the study of the effect of velocity field on tissue injection is challenging because fracture models

are not readily available in FEA simulations. As such, we need to look at simplified models of tissue fracture. We seek to gain insights on the effect of velocity field on tissue injection using two simplified models: 1) the stress field induced in tissue using a first-order model of stress-strain and 2) the travel of a jet of fluid through a more viscous fluid. To isolate the issues of length, developing flow, and energy from other issues such as cavitation or viscous losses due to the contraction of flow, we simplify the nozzle geometry to the pipe geometry.

Stress-field in Tissue

Finite element modeling packages are currently limited in their ability to model fracture mechanics of non-linear anisotropic material such as tissue. Instead of modeling fracture, we thus examine the stress field that a jet may cause in tissue before fracture. COMSOL Multiphysics 5.3 was utilized to generated a first-order model of the stress-field induced in the tissue as the jet contacts the surface of the tissue for velocity fields of the two limiting cases for pipe flow: plug flow and Poiseuille flow.

For a first-order model, we assume that the jet does not travel appreciably from the orifice to the surface of the tissue and therefore the velocity field of the jet right at the orifice is the same as the velocity field of the jet right before impacting the tissue. We also make the approximation that all of the kinetic energy stored in the axial momentum of the jet is converted to static energy (Figure 4-2). Thus, the lossless Bernoulli's equation:

$$P_{orifice} + \frac{1}{2}\rho v_{orifice}(r)^2 + \rho g h_{orifice} = P_{tissue}(r) + \frac{1}{2}\rho v_{tissue}(r)^2 + \rho g h_{tissue},$$

can be simplified to the approximation of

$$\rho v_{orifice}(r)^2 \approx P_{tissue}(r),$$

where P is pressure, ρ is density of the fluid, v is radius-dependent velocity field of the jet, g is acceleration of gravity, h is the distance between orifice and tissue surface,

and $P_{tissue}(r)$ is a force per unit surface area.

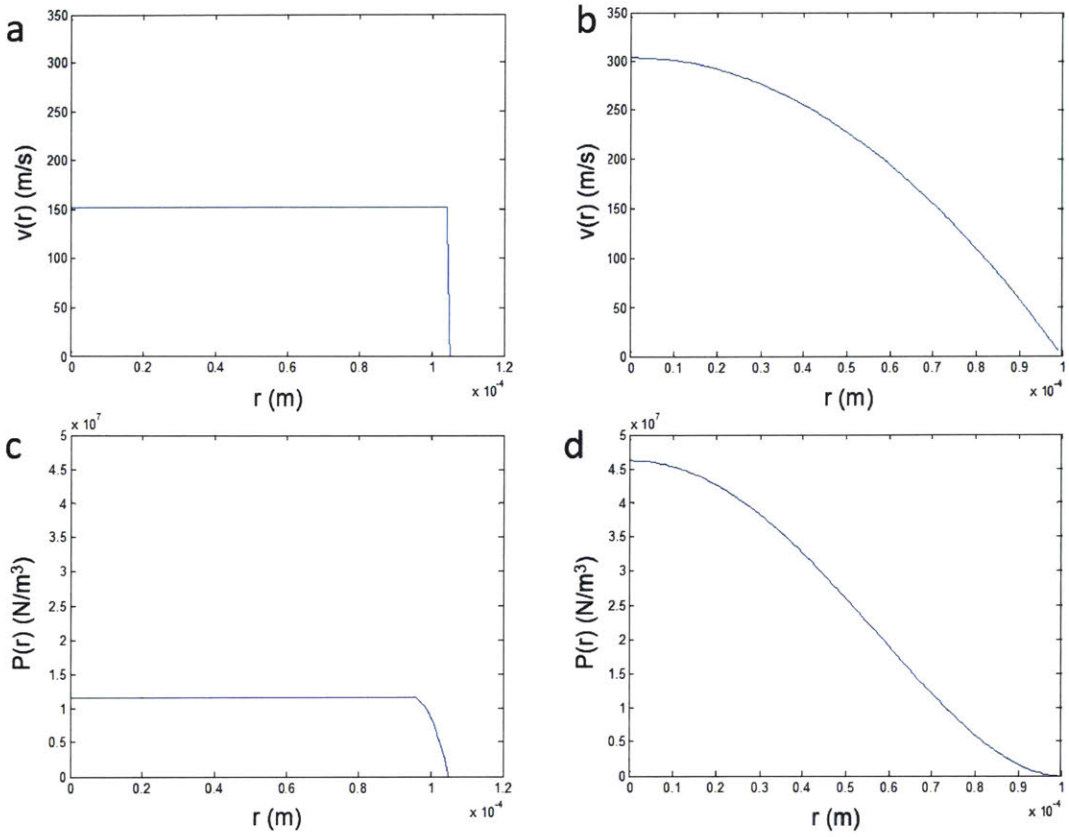

Figure 4-2: The force exerted onto tissue using jets of two types of flow of the same flow rate are compared: plug flow (left) and Poiseuille flow (right). For a first-order model, the approximation is made that all of a jet's kinetic energy is converted into static energy upon impinging the tissue surface. Thus the velocity profile (top row) is used to derive the axial force per unit surface area exerted on the tissue surface (bottom row).

A velocity profile of a uniform axial velocity of 150 m/s is used to simulate the velocity profile of plug flow (Figure 4-2a) and the parabolic profile is used to simulate the velocity profile of Poiseuille flow of the same flow rate (Figure 4-2b). These velocity profiles were used to calculate to first-order the axial force per unit surface exerted by jets of both flows (Figure 4-2c-d). Skin and subcutaneous fat were modeled in this simulation. The density, Young's modulus, and shear modulus [40] were assigned to a 1 mm thick layer of skin and 10 mm layer of subcutaneous fat (Figure 4-3). The axial force per unit surface area, $P_{tissue}(r)$, can then be used as a load on the boundary

of the tissue surface, denoted as side a. Side b is the centerline, around which the axisymmetric geometry is revolved. Side c is set to be fixed and immobile and side d is an arbitrary boundary, free to move.

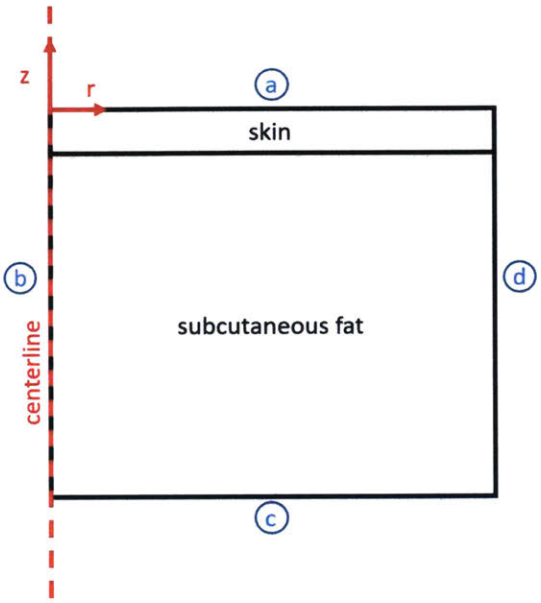

Figure 4-3: The geometry and boundary conditions used to simulate the stress field caused by a jet impinging on the surface of skin. An axisymmetric geometry with side b as the centerline was used.

The first principal stress fields were plotted (Figure 4-4) with the stress at maximum range set at the yield stress of skin, 20 MPa [26]. While the radius of the area of stress induced by a jet of plug flow (Figure 4-4a) is about the same as that induced by a Poiseuille flow jet of the same flow rate (Figure4-4b), the depth is smaller. The red, dotted line indicates a depth of 100 μm, the average thickness of the toughest and first layer of the skin, the epidermis.

This observation suggests that the increased penetration power of a fully developed jet could be significant given the structure of the tissue. However, because the velocity profile of turbulent flow is flatter (less peaked) than that of Poiseuille flow, we expect the difference in stress fields caused by plug flow and fully developed to be less pronounced when considering turbulence. Overall, this study demonstrates the simple but important point of the greater penetration power of a more fully de-

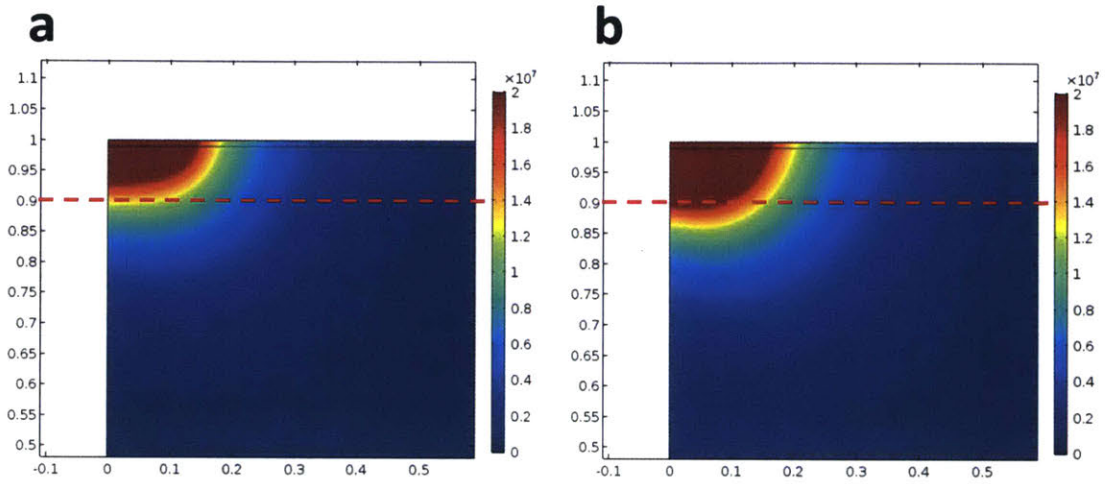

Figure 4-4: First principal stress fields induced in tissue by a) a jet of plug flow at 150 m/s and b) a jet of Poiseuille flow of the same flow rate (color bar represents stress in Pascals).

veloped flow. Because this first-order model greatly reduces the complexity of the fracture model of tissue, other methods of understanding the effect of developing flow on penetration were sought out.

Ejection into Viscous Fluid

Tissue is a visco-elastic material, so ejection into another more viscous fluid may also help us understand the effect of developing flow on penetration power. The model setup is shown in Figure 4-5.

- Geometry: Pipe geometry, length of orifice swept from 0.2 to 5 mm.
- Semi-spherical outlet.
- Boundaries:
  - inlet (side a) was ramped velocity: 0 to 152 m/s in 1 μs 4-6.
  - centerline of axisymmetric geometry is side b
  - no-slip was set at the walls (side c and d)
  - outlet (side e) was set to atmospheric pressure (gauge).

- initial interface between water and glycerol is right at the orifice exit (segment f)

- Two phase flow: water and viscous fluid (glycerol)
- Time transient study: 0 to 25 μs
- Examined depth of ejection by measuring maximum water travel (z-direction) at 25 μs (Figure 4-7.

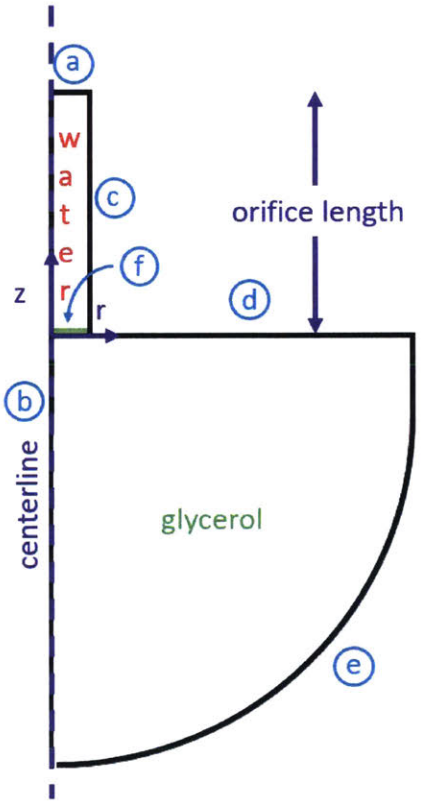

Figure 4-5: The geometry and boundary conditions used to simulate a water jet ejected into a a glycerol reservoir. An axisymmetric geometry with side b as the centerline was used.

The relationship between injection depth versus orifice length of these demonstrate there is a slight increase with more fully developed flow (Figure 4-8).

The simulations of these two simplified analogs of jet injection demonstrate that increasing the development of the flow within a nozzle increases the jet's ability to

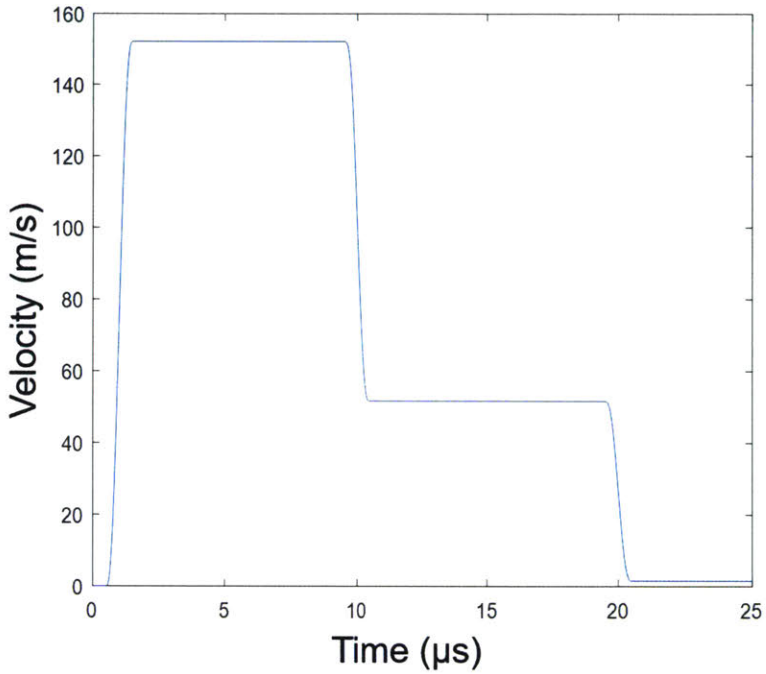

Figure 4-6: Inlet boundary condition was set to a velocity field uniform over the inlet radius (plug flow) that varied over time. The velocity time profile has a high velocity phase v_{jet} designed to breach the tissue followed by a lower velocity phase v_{follow} designed to deliver the bulk of the drug [1].

penetrate tissue. However, given that these two studies seem to indicate that this increase may not be significant and we will explore the energy cost of developing flow in the next section.

Velocity Profile Residual

While we have not yet made a conclusion whether fully developed flow is overall advantageous in injection, it may be useful to define a metric to evaluate velocity profiles for use as a residual in optimization. If we have a desired velocity profile, we can quantify how similar a flow is to the desired velocity profile by calculating the flow rate of the deviation of the velocity profile and normalizing by the total flow rate. That is, given a desired velocity profile, $V_{desired}(r)$, and the velocity profile $V_{actual}(r)$, we first define the deviation velocity profile, $V^*(r)$ as the L2 norm of the two velocity

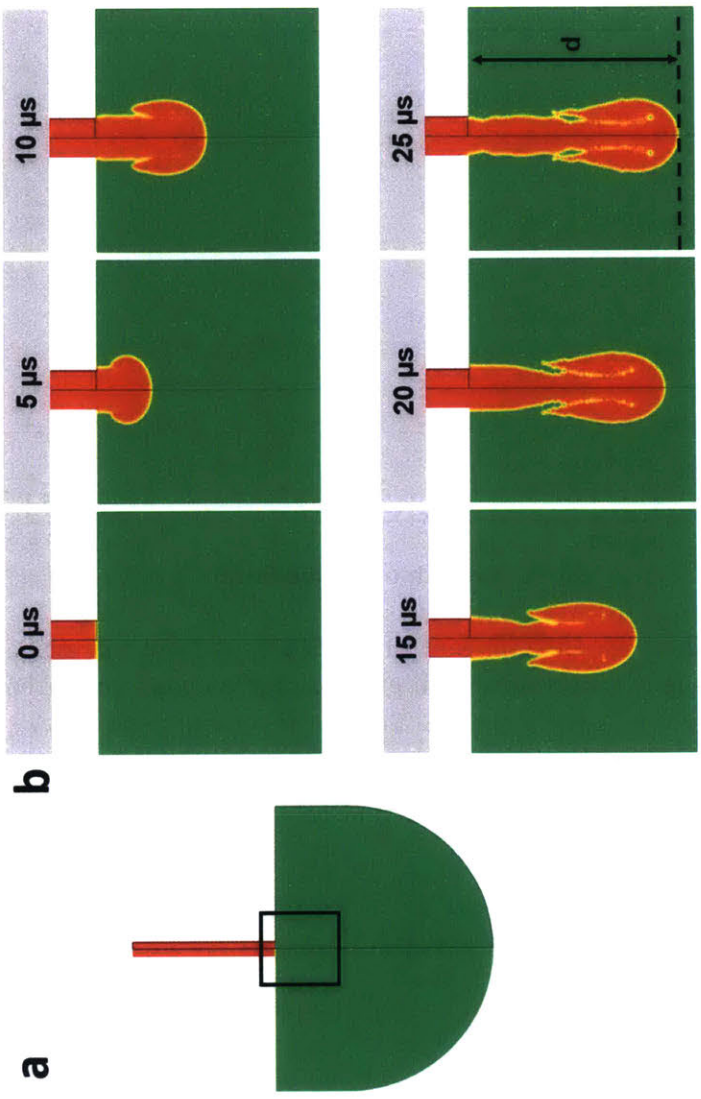

Figure 4-7: Simulation of an ejection of a jet of water into glycerol. Regions of red are occupied by water and regions of green are occupied by glycerol, a) where the black box indicates the window of zoom for the b) time-lapse snapshots from 0 to 25 μs. Depth of ejection, d, is defined as the maximum distance in the axial direction the boundary of the water travels within 25 μs.

profiles (Figure 4-9),

$$V^*(r) = \sqrt{|V_{desired}(r)^2 - V_{actual}(r)^2|}.$$

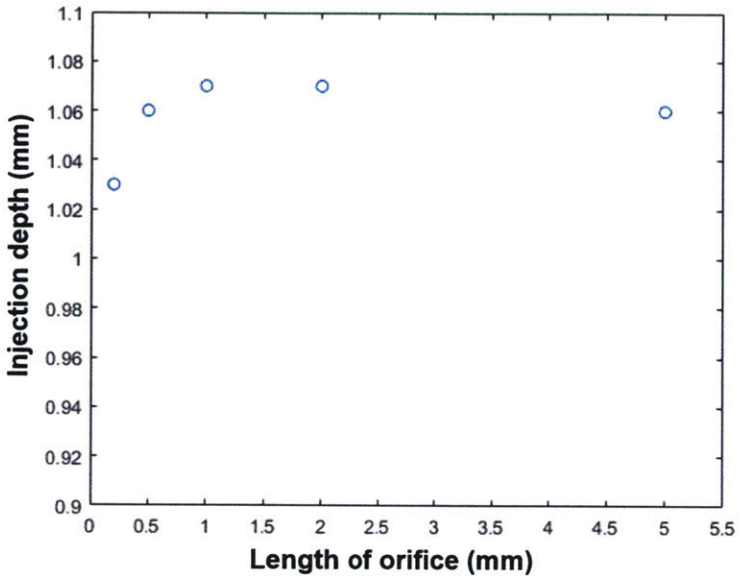

Figure 4-8: Depth of jet ejection into glycerol versus length of orifice. The depth of injection only slightly increases with greater orifice length and greater more fully developed flow.

Then flow rate associated with the deviation velocity profile, Q^* is

$$Q^* = \int_0^R V^*(r)^2(2\pi r)dr,$$

and we can define a residual, Res_{VP}, as the deviation normalized with the total flow rate, Q_{TOT}:

$$Res_{VP} = \frac{Q^*}{Q_{TOT}}.$$

Energy Cost of Developing Flow

Because one of the primary aspects of needle-free technology development is for a portable device, it is important to also analyze velocity field from the perspective of energy.

To study the issues of length, developing flow, and energy we need to isolate these relevant issues from other issues such as cavitation due to adverse pressure gradients or viscous losses due to contraction of flow. Thus, we examine the simple case of

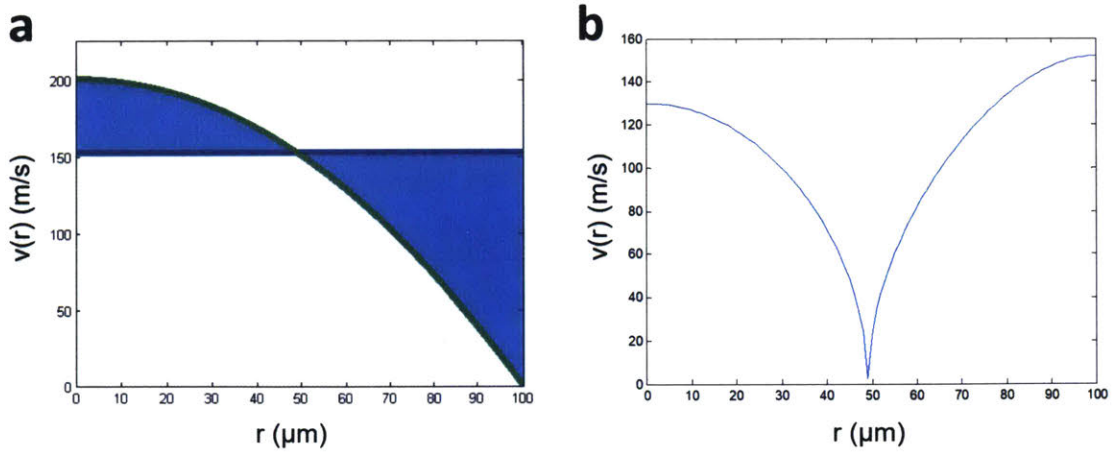

Figure 4-9: a) Given a desired (green) and actual (blue) velocity profile, we can define $V^*(r)$ as the L2 norm of the two velocity profiles.

turbulent flow in a pipe of 200 μm diameter. This pipe would represent the most narrow part of the nozzle geometry, such as the orifice of the cylindrical geometry, where the effects of the boundary layer are most pronounced. Plug flow (uniform velocity across the radial dimension) of a particular velocity is set at the inlet and atmospheric pressure is set at the outlet.

In the first parametric study, the cost associated with fully developed flow is examined. The inlet is set at a uniform velocity of 200 m/s and the pipe length is swept from 0.25 to 10 mm. The inlet power is linearly related with pipe length (Figure 4-10a). This relation is consistent with the Darcy-Weisbach equation (Chapter 3).

As the flow becomes more developed, the velocity profile curves and increases in magnitude near the center (Figure 4-10c). There is no significant change in velocity profile at the outlet when the pipe length exceeds the distance required for the flow to develop in a pipe. This distance is also known as the entrance length, L_h, and for turbulent flow is expressed as [41]:

$$L_{h,turbulent} = 4.4D(Re)^{1/6},$$

where D is the diameter of the pipe, and Re is the Reynolds number.

Because the velocity profile does not significantly change at the outlet with fur-

ther increases of pipe length, the outlet power should be constant at pipe lengths greater than the entrance length. Given the given parameters, the entrance length is calculated to be about 5 mm, after which the outlet power indeed does not further increase (Figure 4-10a).

The efficiency of flow starts near 100% for pipes of lengths much smaller than the entrance length, decreases to 70% at pipe lengths for which the flow is just fully developed at the outlet, and continues to decrease as flows in pipes of greater length require greater input power but output a flow of unchanging power (Figure 4-10b). When comparing turbulent plug flow and fully developed turbulent flow, there is a large increase in required inlet power but only a small increase in output power. This energy analysis challenges the notion of whether fully developed flow is advantageous in a portable NFI injector.

A second study is carried out to investigate the energy of partially developed flow. In this parametric study, the pipe length is fixed at constant 1 mm, and the uniform inlet velocity is swept from 150 to 240 m/s. A pipe length of 1 mm will yield flow that is partially developed. When the inlet velocity is increased, both inlet and outlet power increases at an increasing rate yielding an upward curve (Figure 4-11a). Because pressure drop scales with the square of velocity and energy, the square of the velocity and pressure at the inlet increases at the same rate as the square of the velocity of the inlet, yield a constant efficiency across the range of inlet velocities (Figure 4-11b)). In this case, because the length is constant, the shape of the velocity profile does not change, instead increasing velocities effectually scales the velocity profile by a larger constant (Figure 4-11c).

A flow of 200 m/s at the inlet in a 5 mm length pipe (a length such that the flow is just fully developed at the outlet), peaks at about 235 m/s, requires 199 W at the inlet, and yields 132 W at the outlet. We observe that a flow of 230 m/s at the inlet in a pipe of 1 mm length peaks at about 246 m/s, requires 197 W at the inlet, and yields 219 W at the outlet. We now make the point that for similar input energy, flows more similar to plug flow yield similar peak velocities in its velocity profile and significantly increased output power when compared to that of fully developed

flow. This comparison should be general across all inlet velocities as long as the flow is turbulent and only the loss considered is the viscous loss due to the growing boundary layer at the orifice walls. Because the efficiency of a flow in a pipe of a chosen length is preserved across different inlet velocities of the relevant ranges, there should always exist a number of partially developed flow that is more advantageous than fully developed.

It should also be noted that once the constraint of the nozzle wall is removed, velocity profile relaxation occurs within the jet. The tendency for the velocity profile to relax by a mechanism of momentum transfer between circumferential layers of the jet significantly decreases the stability of the traveling jet [38]. Earlier work has shown that the break-up length of glycerol jets traveling through water decrease as the flow at the orifice exit is more fully developed [42].

We conclude that fully developed flow is less advantageous than partially developed flow and plug flow. The degree to which flow is developed is positively correlated with energy lost to viscous losses, and thus a nozzle of less developed flow is also a nozzle of lower loss.

It is possible of course, to still include the velocity profile residual in the objective function and simply dictate plug flow as the target velocity. However, the efficiency residual already prioritizes plug flow because a priority on decreasing viscous losses in the nozzle would translate to decreasing the orifice length (decreasing the length of the boundary layer along the pipe walls) and thus favoring less developed flow. Therefore, to avoid double-counting, in the new version of the objective function (starting with Z_2), efficiency but not velocity field was included.

4.2.2 Cavitation

In Chapter 3, the effect of geometric elements on regions of cavitation pressure in the interior of nozzles was examined. We now set out to study the behavior of a cavitating bubble along a given streamline in the flow of the nozzle with the goal of developing a quantitative metric for use as a residual in the objective function.

The Rayleigh-Plesset is a 2nd order ordinary differential equation that describes

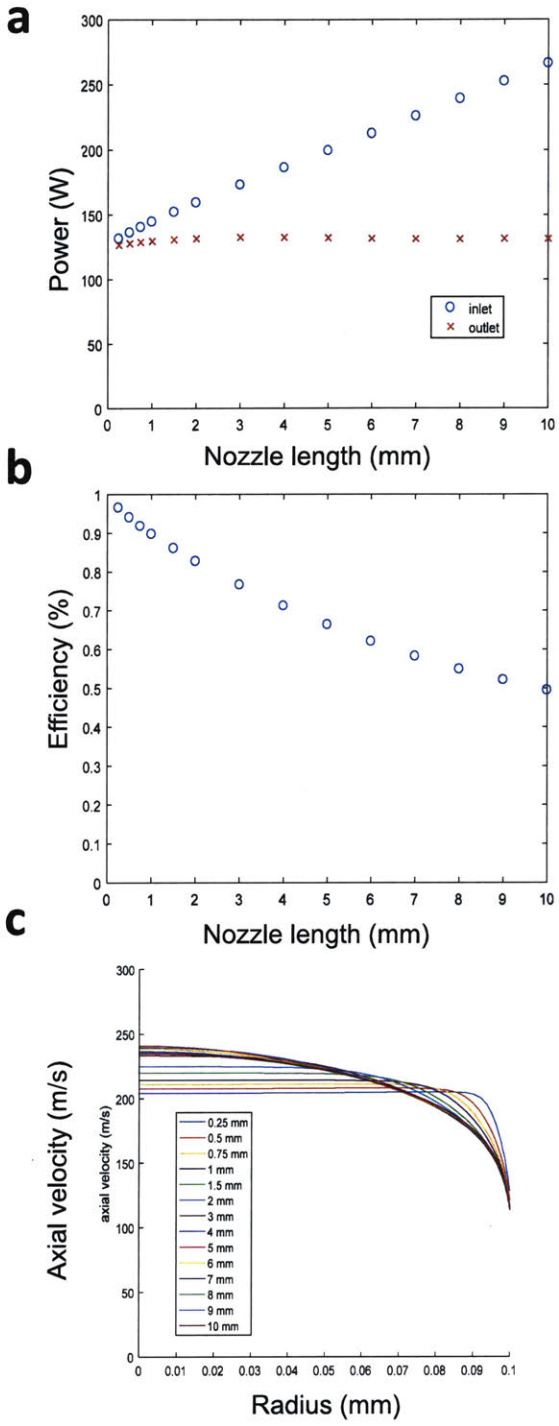

Figure 4-10: a) Inlet power and outlet power, b) mechanical efficiency, and c) axial velocity profiles (at outlet) of pipes of length that ranges from 0.25 to 10 mm and constant inlet velocity of 200 m/s.

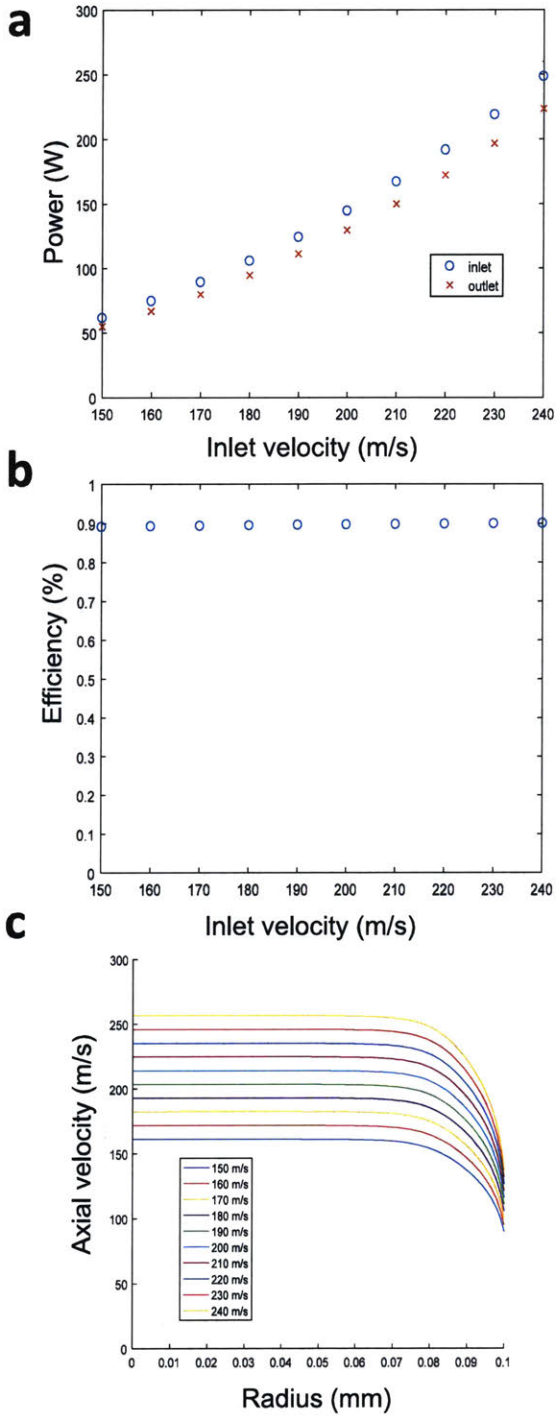

Figure 4-11: a) Inlet power and outlet power, b) mechanical efficiency, and c) axial velocity profiles (at outlet) of pipes of constant length 1 mm and inlet velocities that ranges from 150 to 240 m/s.

how a bubble will grow or shrink in a changing pressure field,

$$\rho\Big[R\ddot{R} + \frac{3}{2}\dot{R}^2\Big] = \Big[p_v(t) - p_\infty(t)\Big] - \frac{2S}{R} - 4\mu\frac{\dot{R}}{R},$$

where ρ is the density of the surrounding liquid, R is the radius of the bubble, p_v is the time-dependent vapor pressure of the surrounding liquid, p_{infty} is the time-dependent pressure of the surrounding liquid, S is the surface tension of the gas-liquid interface, and mu is the viscosity of the liquid.

To make a first-order estimate, we make a few simplifying assumptions. First, we assume that the temperature does not change significantly from room temperature and therefore the vapor pressure is relatively constant. Of primary interest then are regions of flow where the pressures dip below the vapor pressure of water at room temperature (25 °C): 3169 Pa. Second, we make the approximation that the bubbles will not affect the overall flow and will follow the flow. Then we can analyze the pressure along a streamline and analyze how a bubble seed will behave as it travels along that streamline (Figure 4-12a). Third, we will assume that a seed bubble of radius 1 μm is placed at the beginning of the streamline is is common in tap water at room temperature [37]. Finally, we will assume that the cavitating bubbles are fairly sizable compared to the nozzle radius, greater than 1% of the nozzle radius, that is, larger than 1 micron. If so, then the dominant force on the bubble is the pressure it experiences and we will ignore the surface tension and viscosity terms on the right hand side to yield the simplified expression:

$$\rho\Big[R\ddot{R} + \frac{3}{2}\dot{R}^2\Big] = \Big[p_v(t) - p_\infty(t)\Big].$$

We can thus track the pressure versus distance along a streamline 4-12b), integrate the velocity along that streamline to find the pressure as a function of time instead of distance, solve the simplified Rayleigh-Plesset equation to find the radius of the bubble as a function of time, then use our known time to distance mapping to find a first-order estimate of the radius of the bubble as a function of the distance it travels along the streamline 4-12c). By plotting the cavitation along 50 streamlines that

span the radius the nozzle, one can estimate where the cavitation will occur in entire region of flow 4-12d).

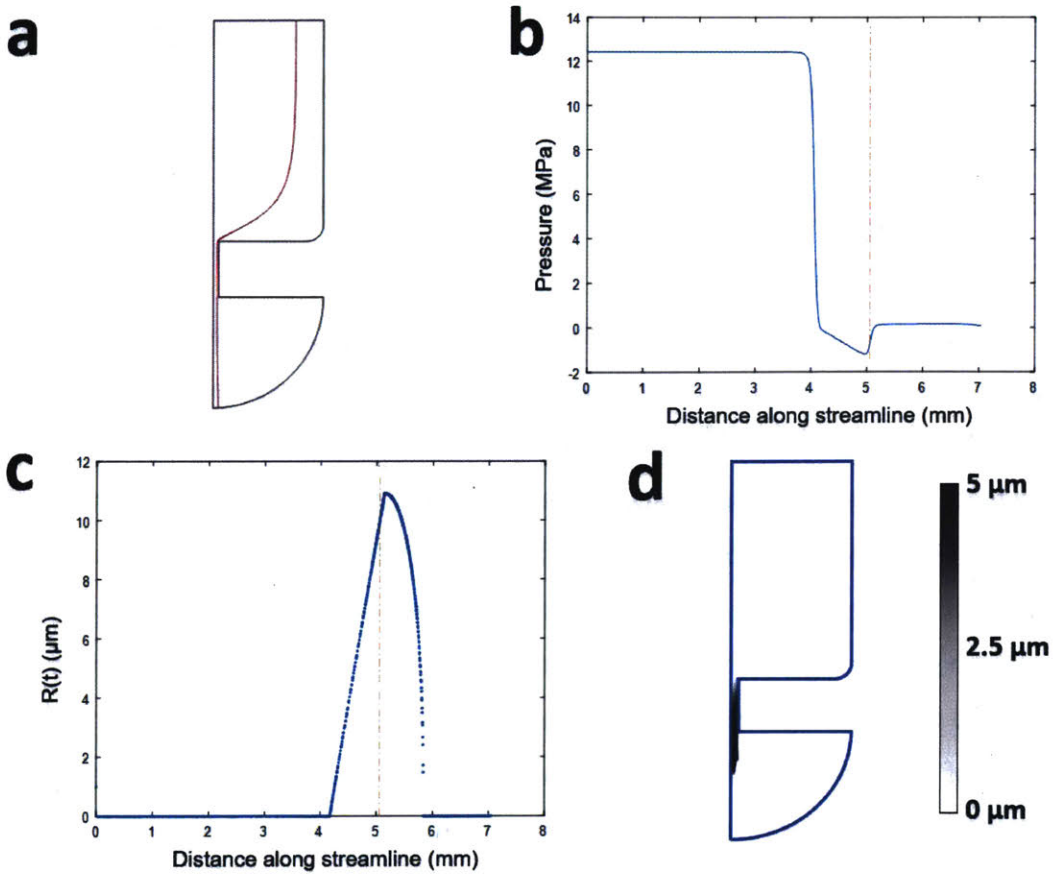

Figure 4-12: By tracking a seed bubble down many streamlines that span across the nozzle, one can estimate the amount of cavitation a nozzle will produce and the regions where cavitation will occur. a) A sample streamline of the flow in a cylindrical nozzle. b) The pressure along the sample streamline a fluid particle or bubble will experience. c) A first-order estimate of the radius of the bubble as it travels along the streamline. d) By plotting 50 streamlines spanning the entire nozzle, one can predict where the cavitation will occur in the region of flow. The flow region is represented by a grayscale plot, where white is assigned to no bubble and fully black is assigned to a bubble of 5 μm radius.

One limitation to this approach is readily apparent. First, the pressure of the majority of the ampoule is on the order of millions of Pascals, sufficiently high such that the model predicts a seed bubble of 1 μm radius will soon collapse after little travel down the streamline 4-12b). Because the Rayleigh-Plesset equation predicts

that a bubble of an initial radius near 0 μm will remain near zero, the model fails to take into account the beginning growth of the bubble when the fluid first passes through the cavitation region. As an approximation, we use the last (and smallest) radius of the bubble right before collapse as the radius of the bubble seed that enters into the cavitation region. While the seed radius is well below 1 μm where surface tension and viscosity should compete with pressure, we continue to ignore these terms because the majority of the duration of the bubble's growth and collapse is spent above 1 μm.

Examination of streamlines in cases of flow separation reveal a second limitation to this approach of simulating cavitation. Because this approach relies on calculating bubbles along the streamlines that begin at the inlet, there exist some geometries for which this streamline approach to simulating cavitation will be less accurate. In the cylindrical geometry for example, a decreased fillet radius at the entrance to the cylindrical orifice yields a larger region of pressure below vapor pressure cavitation but also a greater region of flow separation, as seen by the streamlines bend away from the sharp corner. Because streamlines that begin at the inlet do not pass through the regions of flow separation, predicting cavitation regions and calculating the amount of cavitation will be less accurate in these cases. In cavitation analysis by streamlines, the streamlines must therefore first be visually inspected to see if there are regions of flow separation. In the example of the cylindrical geometry, the streamline approach to calculating cavitation is most accurate for the geometries with fillet radii of 5 μm and above, for which there is little flow separation.

Taking these two limitations into account, the streamline approach to calculating cavitation may be a useful tool for many nozzle geometries of interest.

One possible residual could be based on capturing the loss of energy due to the creation of bubbles. We can define a cavitation residual to capture the volume of bubbles within the region of flow as:

$$Res_{cav1} = \sum_i \int_{s_{i,start}}^{s_{i,end}} R(s_i')^3 r(s_i') ds_i',$$

where i is the index of the streamline (in our cases i = 1 to 50), s is the streamline distance, R is the radius of the cavitation bubble, and r is the radial distance of the point s from the axis.

Cavitation within the NFI nozzle may also influence the dispersion angle. In the field of fuel injector design, the dispersion angle of jets issuing from 2D planar nozzles ranged from 0 to 14 degrees, greatly enhancing the break-up of the jet, depending on whether the cavitation within the nozzle reached the orifice exit. Thus, we define a cavitation residual to capture the flow rate of bubbles that leave the orifice exit:

$$Res_{cav2} = \int_0^R R(r', s_{outlet})^3 r(s_{outlet}) v(r') dr',$$

where v is the total velocity at point r in the orifice.

We will choose the first residual for optimization. A cavitation residual that more accurately captures the criteria of NFI should be informed by experiments.

4.2.3 Efficiency

In both versions of the objective function, we will choose to include efficiency in the objective function. Calculating efficiency takes into account both the viscous loss due to the boundary layer along the nozzle wall and any potential viscous loss due to flow separation. Because we seek a residual to minimize and we thus define a residual to encompass energy loss, Res_L:

$$Res_L = 1 - E = 1 - \frac{P(z_{outlet})}{P(z_{inlet})},$$

where E is efficiency, $P(z_{inlet})$ and $P(z_{outlet})$ is the mechanical power that flows through the inlet and outlet, respectively, and have been defined in Chapter 3. Because the loss residual is already normalized to one, it is well-behaved and can be readily used in conjunction with other residuals to form an overall objective function.

4.3 Geometry

A profile that is revolved around the axis to form the nozzle geometry can be split into two general categories: shape and its length. By shape, we mean an outline that is length-independent. We define length-independent as the following: two given shapes are length-independent from each other, if there is no way one shape can be linearly stretched to yield the other. (An ellipse and a circle for example would not be considered length-independent.)

4.3.1 General Basis Functions

We first seek a basis of functions that is able to form the entire range of nozzle shapes we are interested in. Chebyshev functions garner interest because of their frequent application in curve-fitting. Two such polynomials, normal Chebyshev polynomials of the 1st kind and rational Chebyshev polynomials are defined as follows:

$$T_0(x) = 1$$

$$T_1(x) = x$$

$$T_2(x) = 2xT_n(x) - T_{n-1}(x)$$

and

$$T_{p,q}(x) = \frac{p(x)}{q(x)} = \frac{c_0T_0(x) + ... + c_nT_n(x)}{c_{n+1}T_0(x) + ... + c_2nT_n(x)},$$

respectively.

A target nozzle profile is chosen. Regular and rational Chebyshev polynomials are used to fit to the target nozzle profile (Figure 4-13.

Figure 4-14 shows the maximum difference (in microns) between the sample nozzle curve and fit of rational and normal chebyshev. 5 μm is set as a sample minimum tolerance. While the minimum order of rational chebyshev polynomials fit is nearly an order magnitude less than that of normal chebyshev polynomials, the order is still high. A minimum polynomial order of 18 translates to an optimization requiring 18

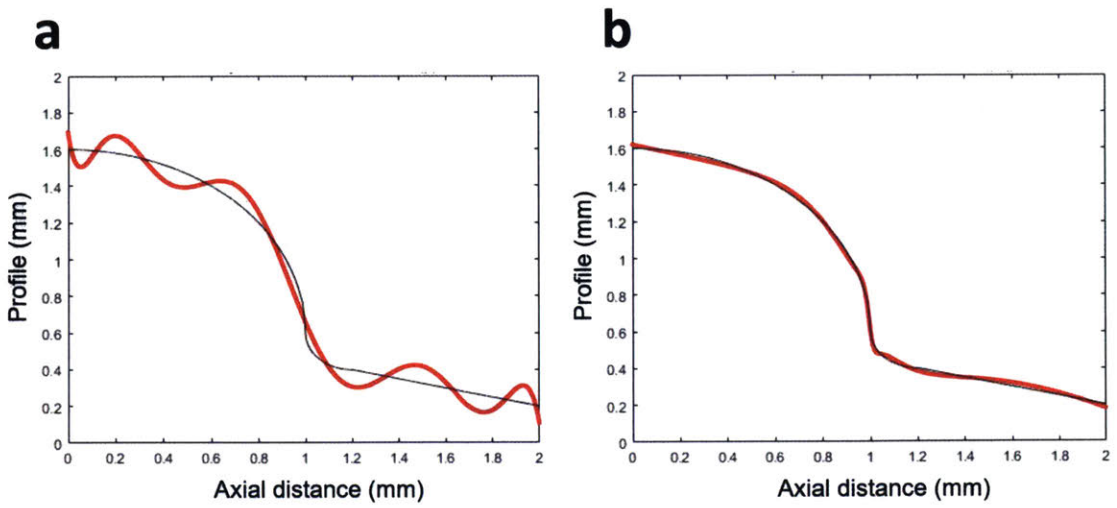

Figure 4-13: 10th order Chebyshev and 10th order rational Chebyshev polynomials fit to a given nozzle shape. Red is the fit and black is the target nozzle shape.

independent degrees of freedom, which is computationally costly.

4.3.2 Physics Informed Basis Function

Curve-fitting polynomials assume little about the situation *a priori*. We seek to decrease the number of degrees of freedom in the basis function by picking a basis function informed by physical intuition.

We first consider the nozzle as a tool to convert pressure into kinetic energy or momentum. The overall momentum and kinetic energy is related to the average velocity through the surface perpendicular to the axis at a given point ("bulk velocity") or the square of the bulk velocity ("bulk velocity squared"), respectively.

Given particular profiles of bulk velocity or bulk velocity squared, such as linear, squared, or cubic profiles, we can directly compute by conservation of mass the nozzle shape that would produce such a profile (Figure 4-15).

For simplicity sake, we will choose bulk velocity.

Using polynomials to produce a range of bulk velocity profiles will yield the familiar problem of large numbers of degrees of freedom leading to high computational cost. In seeking a set of curves to classify the range of bulk velocities, where the nozzle exit is placed at x = 0 and the nozzle inlet is located somewhere on the positive

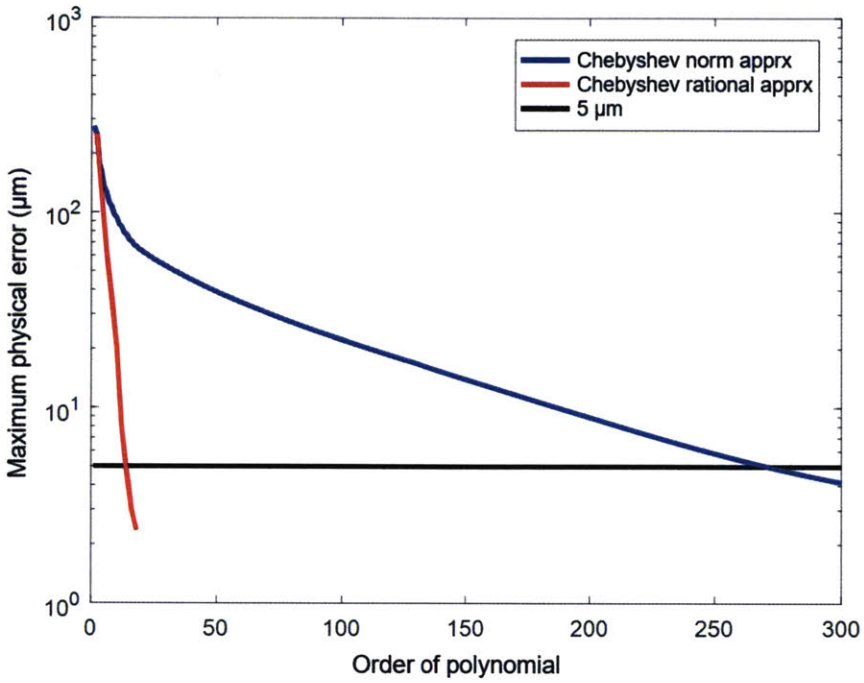

Figure 4-14: Maximum difference between sample nozzle shape and their normal and rational Chebyshev polynomial fits.

x-axis. Informed from insights from chapter 3, we want the set of curves to have the following characteristics:

1. *Curves must be at least C2 continuous.* In Chapter 3, we made the observation that the geometry with the smallest entrance fillet radius (the sharpest orifice entrance) induced the largest flow separation and cavitation. To avoid abrupt changes in the curve or discontinuities in the first derivative, we impose a requirement of C2 continuity or higher.

2. *The exit fillet will be set at 5 μm.* Smaller exit fillets decrease the risk of flow separation at the exit.

3. *Orifice length will be kept a parameter.* Decreasing orifice length decreases viscous loss, and increases efficiency, but the nozzle cannot be infinitely short.

4. *Curves must be monotonically decreasing in the direction of flow.* A curve that increases in the direction of flow leads to flow expansion, which induces flow

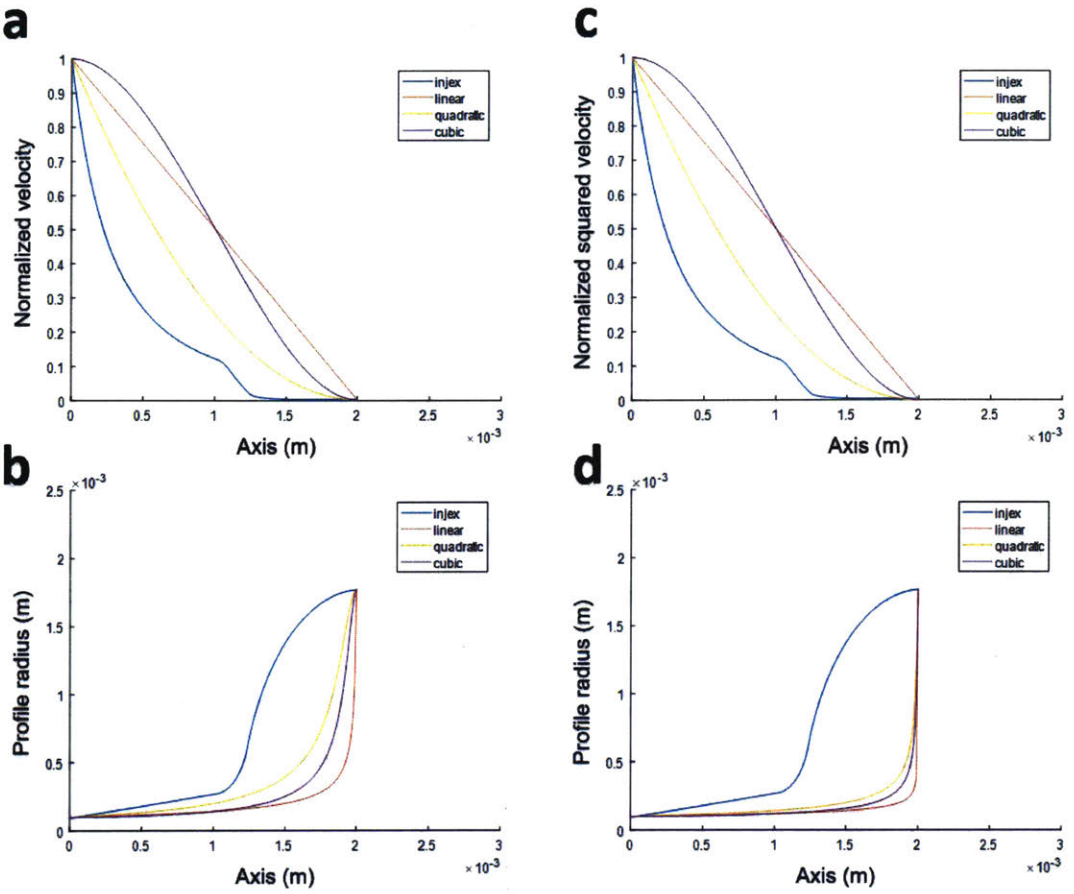

Figure 4-15: Given profiles of a) bulk velocity or c) bulk velocity squared such as linear, quadratic, or cubic, the b, d) nozzle shapes to produce such bulk shaping can be directly computed.

separation and eddies, unfavorable in NFI.

5. *Curves must be monotonically decreasing in the direction of flow.* A curve that increases in the direction of flow leads to flow expansion, which induces flow separation and eddies, unfavorable in NFI.

6. *The set must cover a wide range of curves, including convex and concave, with as few degrees of freedom as possible.* We seek to capture the largest possible curves with the smallest computational cost.

The convection-diffusion equation without sources or sinks,

$$\frac{dc}{dt} = D\frac{d^2c}{dx^2} - v\frac{dc}{dx},$$

can be repurposed by replacing c(x) with the bulk velocity, v(z), of a nozzle, and the general coordinate x can be replaced by z, the distance along the nozzle axis:

$$\frac{dv}{dt} = c1\frac{d^2v}{dz^2} - c2\frac{dv}{dz}.$$

The solutions to the 1D heat convection-diffusion equation presents a promising set of curves for bulk velocity shaping because of each curve is at least C2 continuous and monotonically decreasing. We define a parameter $t_{frac} \in (0, 1)$ such that $t_{frac} \times t_{max} \in (0, t_{max})$.

When c1 = 10, c2 = 100, and $t_{max} = 0.01$ (Figure 4-16a) a wide range of curves is covered when t_{frac} is swept from 0 to 1. These solutions can then be mapped to bulk velocity that begins at the piston velocity at the inlet and the desired outlet velocity (Figure 4-16b). The resultant nozzle shapes can then be calculated by principle of conservation of mass (Figure 4-16c). These shapes can readily be inputted into the COMSOL interface for CFD solve (Figure 4-17).

Because the entrance length of a pipe of 200 μm is 5 mm, we select the maximum possible orifice lengths to be to be 5 mm. The two geometry categories of shape and length can each be characterized by a single parameter, t_{frac} and length, respectively. The geometry space for optimization has thus been reduced from an 18-degree problem to a two-degree problem.

4.4 Optimization

Because we have managed to express the optimization problem with two degrees, the computational cost is drastically decreased, obviating the need for sophisticated optimization algorithms. Because a single simulation requires only 180 to 600 seconds to complete, we can perform a two-dimensional sweep to view the contour of each

residual, the overall objective function, and find the approximate minimum.

We define two objective functions, Z_1 and Z_2:

$$Z_1 = res_L + res_{VF},$$

and

$$Z_2 = res_L + res_{cav1}.$$

For Z_1, we perform a 20 $\times$ 20 sweep, where t_{frac} is swept from 0.001 to 0.999 and length is swept from 0.5 to 4.8 mm. The loss residual increases with increasing length because of increased viscous loss in the boundary layer and increases with increasing t_{frac} because there is greater flow separation at an increasingly sharper point of flow contraction (Figure 4-18a). The velocity field residual increases with decreasing length because the flow is less developed and increases with decreasing t_{frac} because less of the geometry is at radii close to the outlet radius and is thus less developed as well (Figure 4-18b). In the overall objective function, while there is a valley that runs from the corner of maximum length and minimum t_{frac} to the corner of minimum length and maximum t_{frac}, the overall contour is slight (Figure 4-18c).

For Z_2, we perform a 19 $\times$ 20 sweep, where t_{frac} is swept from 0.025 to 0.95 and length is swept from 0.5 to 5 mm. The loss residual behaves as described previously (Figure 4-19a). The cavitation residual increases with increasing length because the cavitation bubble exists for increasing distances in the nozzle and increases with increasing t_{frac} because of the larger and more greater negative pressure region around the point of flow contraction (Figure 4-19b). In the overall objective function, there is a clear minimum near the corner of the space: minimum length and minimum t_{frac} (Figure 4-19c). We thus yield the optimized nozzle where length = 0.5 mm and t_{frac} = 0.025 (Figure 4-20).

4.5 Summary

The work of shape optimization is split up into three categories and its overview presented: a choice of an appropriate optimization function, basis functions to capture the range of nozzle geometries of interest, and method to optimize. From the perspectives of energy and penetration ability, it is argued that less developed flow is more advantageous for NFI. We create residuals capturing viscous loss, velocity field, and cavitation, and use them to form two possible objective functions. Because a general basis of function requires many degrees of freedom, we take solutions of the convection-diffusion equation to form profiles of the bulk velocity, and use these profiles to generate nozzle curves. This approach reduces the degrees of freedom of the optimization from over 18 to two, drastically reducing the computational cost for optimization. The optimized nozzle is found by taking 2D sweeps of the nozzle shape space of each objective function, one combining loss and velocity field and another combining loss and cavitation. Given that less developed flow is advantageous, the optimized nozzle found using an objective function of the residuals of loss and cavitation is presented as the final optimized nozzle.

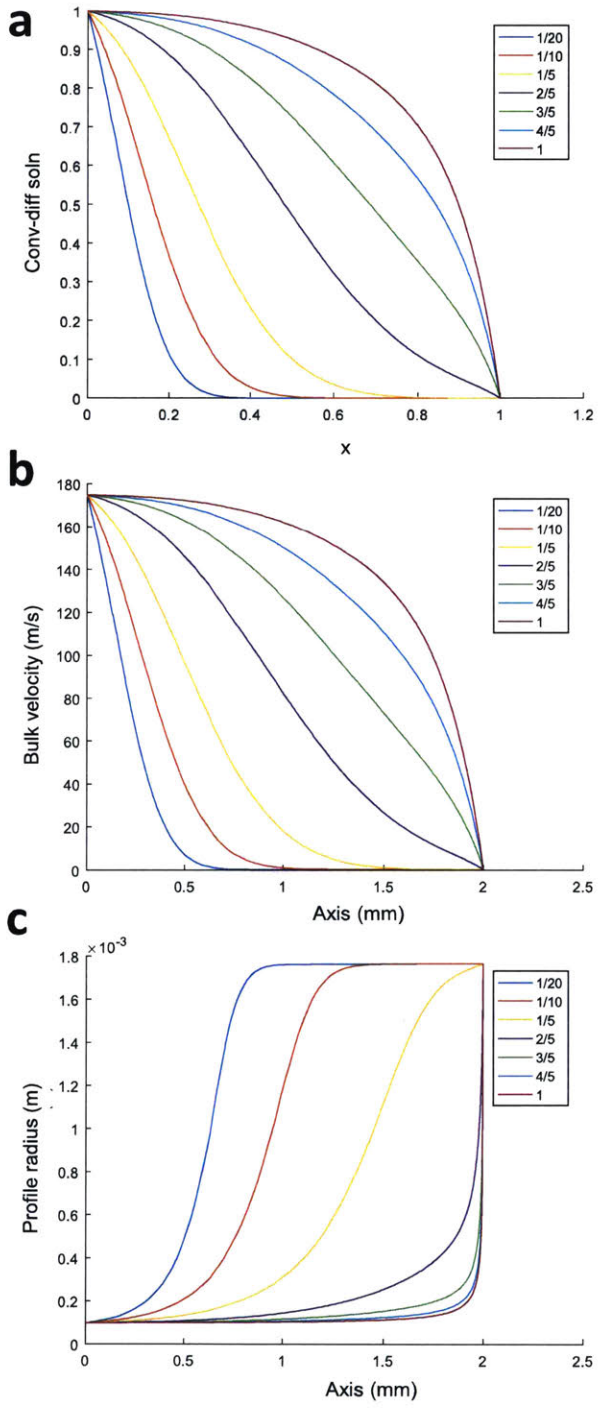

Figure 4-16: a) Solutions to the 1-D convection diffusion equation at different values of "time", shown here a range of 1/20 to 1. b) Given average inlet and outlet velocity, and length, mapping the the solutions form profiles of bulk velocity. c) Using conservation of mass flow, nozzle shapes are calculated from the bulk velocity profiles.

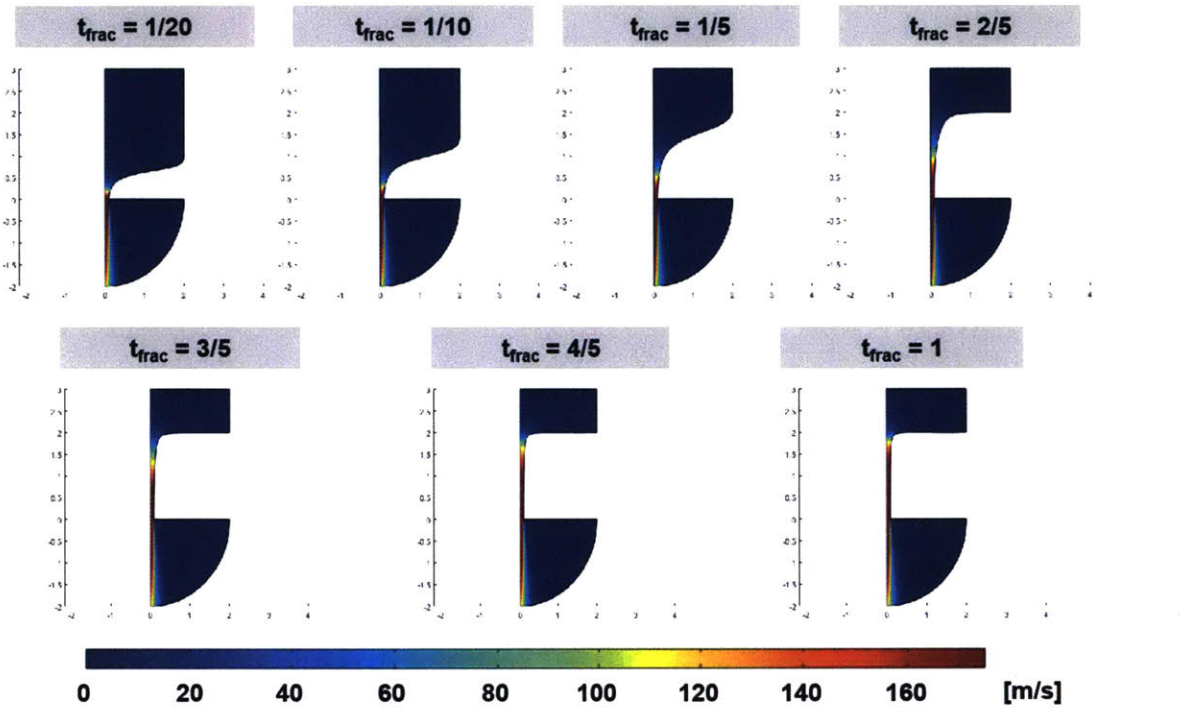

Figure 4-17: CFD solves of sample geometries generated by the bulk shaping approach. Total velocity is shown here as a 2D surface plot. Sweeping the one parameter, non-dimensional "time", yields a range of nozzle shapes.

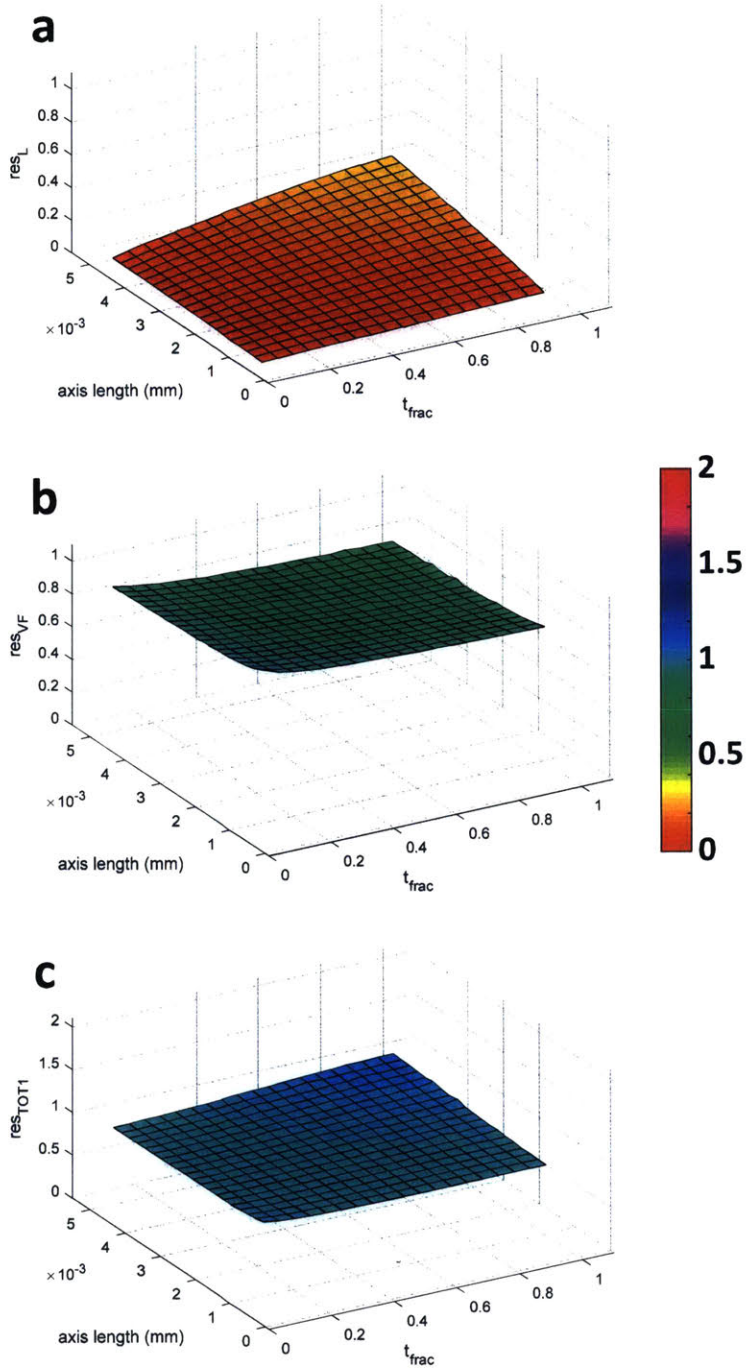

Figure 4-18: Results of optimization using objective function Z_1: a) loss residual, b) velocity field residual, and total residual.

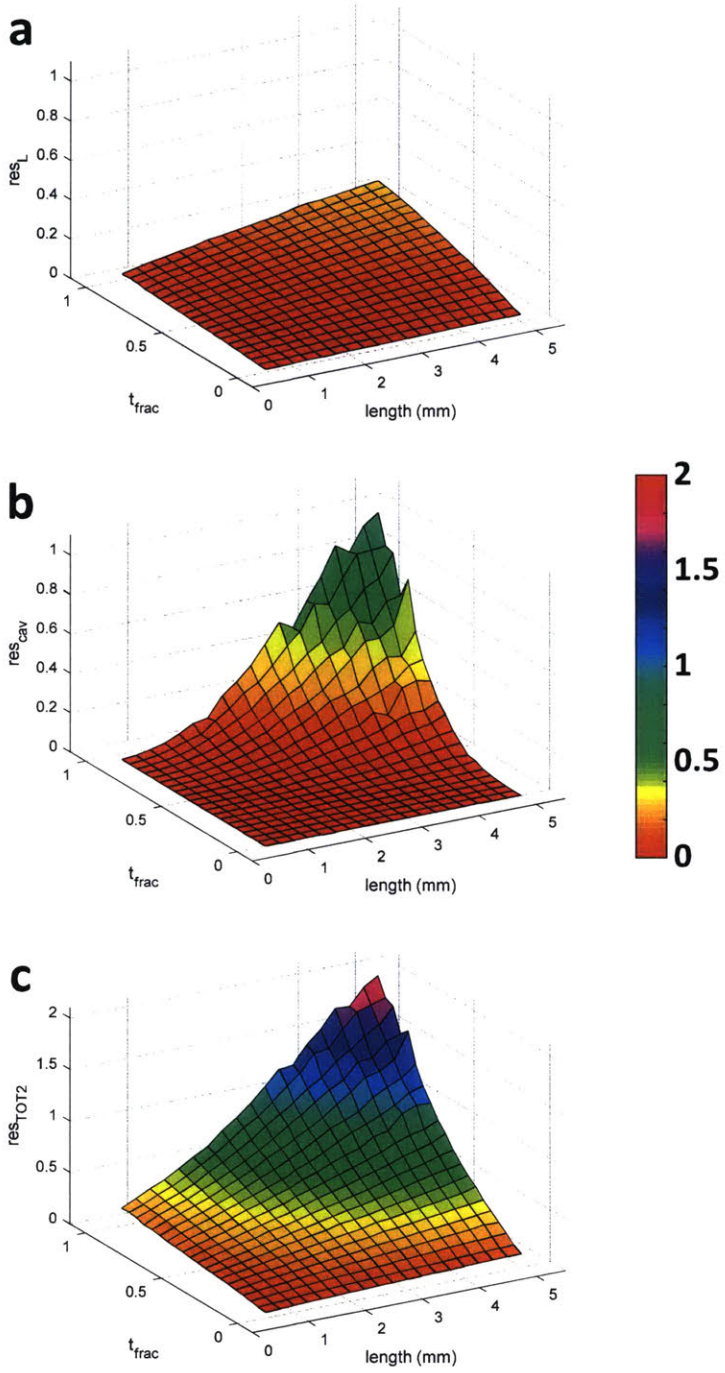

Figure 4-19: Results of optimization using objective function Z_2: a) loss residual, b) cavitation residual, and total residual.

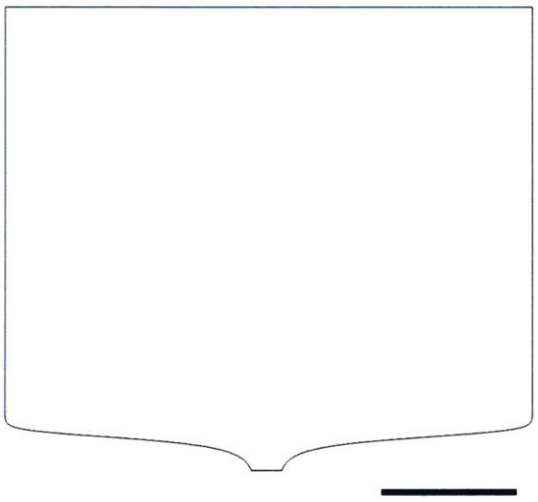

Figure 4-20: The optimized geometry of the Z_2 objective function: length = 0.5 mm, TF = 0.025. (Scale bar = 1 mm.)

Chapter 5

Nozzle Orifice Fabrication

5.1 Introduction

In Chapter 4, an optimization framework is presented that is composed of an objective function informed by residuals relating to the fluid flow, a geometry space informed by the physics of fluid flow, and a two-dimensional sweep to find the optimized nozzle shape. This chapter presents the fabrication of axisymmetric nozzle orifices for needle-free injection and planar nozzle orifices to examine via high-speed imaging the cavitation within nozzles of different shapes. The structural integrity of the manufactured nozzles will inform the creation of an additional type of residual to improve on the objective function from Chapter 4.

5.2 Fabrication of Axisymmetric Nozzles

A number of techniques exist to fabricate nozzle orifices (Table 5.1). Micro-drilling is readily available, demonstrated in Chapter 2, and can produce orifices with diameters as small as 50 μm. However, micro-drilling is limited to producing the cylindrical orifice. Similarly, a lapping procedure has been developed in in the industry, such as Bird Precision, to produce fine geometries in tough materials such as sapphires for use in waterjet cutting. However, lapping is also limited to producing cylindrical and conical orifices. Both ceramic and injection molding can consistently yield 3D

axisymmetric geometries, but the equipment required is often expensive or not suited for fast prototyping.

Sink EDM (also known as sinker EDM) is a promising machining method to fabricate the desired nozzles because of its ability to create cavities of small, complex 3D shapes to machining tolerances on the order of microns, accessibility and cost [7].

Method	Cost	3D shapes	Rapid-prototyping
Micro-drilling	low	no	yes
Lapping	low	no	yes
Ceramic molding	medium	yes	yes
Injection molding	high	yes	no
Sink EDM	low	yes	yes

Table 5.1: Overview of manufacturing methods for nozzle orifices.

5.2.1 Background on Electrical Discharge Machining

Electrical discharge machining (EDM) is a method of non-contact machining that has gained traction over the years because of its ability to cut a wide range of shapes and metals. As such, EDM machining is commonly used in a range of industries such as medical devices, aerospace, and mold-making [7]. While the physics underlying spark erosion is still an area of research [43, 44, 45], the process operates on the principle of erosion of metals by spark discharges, EDM uses electrical energy turned into thermal energy instead of shear stress. When hundreds of volts are applied across a liquid dielectric filled gap between the electrode (also called "tool") and workpiece, thousands of sparks per second are controllably generated, creating an ionizing channel between the workpiece and electrode. Each spark produces a tiny crater by melting and vaporizing, thus eroding the workpiece to the shape of the tool (Figure 5-1). As such, EDM is one of the most accurate manufacturing processes for creating shapes that are complex, cutting hard materials such as tool steel or tungsten carbide, or cutting fragile materials that cannot withstand the stresses induced by traditional manufacturing techniques such as milling, turning, and grinding [7].

Two general types of EDM exist: wire and sink. The wire EDM uses a thin

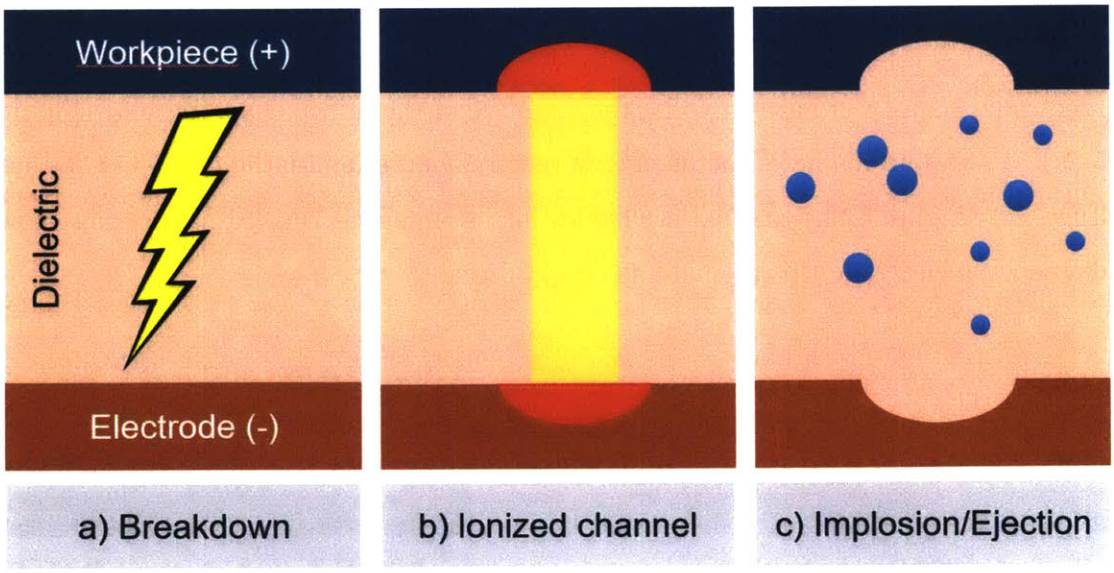

Figure 5-1: Electrical discharge machining operates on the principle of spark erosion [7]. a) Hundreds of volts are applied across a liquid dielectric filled gap between the electrode and workpiece, generating thousands of sparks per second and b) forming an ionized channel between workpiece and electrode. c) Each spark produces a tiny crater by melting and vaporizing, thus eroding the workpiece to the shape of the tool.

single-strand wire on the order of 20 to 400 μm in diameter, fed through a top and bottom wire guide that can be individually controlled to move in the X-Y plane to cut through metal plates as thick as 300 mm. The sink EDM uses an electrode to erode a workpiece away, with possible machining movements such as vertical, orbital, vectorial, directional, helical, conical, and rotational [7]. The resulting cavity in the workpiece is generally the volume mapped out by movement of the electrode. Thus, in the simple case of a vertical motion, the eroded cavity in the workpiece is in very shape of the electrode.

5.2.2 Developing a Nozzle Fabrication Method

Some of the crucial issues in sink EDM machining include workpiece and electrode material choice and tool removal wear [7]. These issues will guide the development of an appropriate method to fabricate nozzles.

Electrode Fabrication

Electrode shapes were drawn to be the negative of the orifice shape desired (Figure 5-2a). 3 to 5 mm diameter metal rods were turned on a mini-lathe (EMCO Concept Turn 55) (Figure 5-2b) to yield electrodes for use in sink EDM. SEM imaging show diameter of electrode tips as small as 20 to 30 μm.

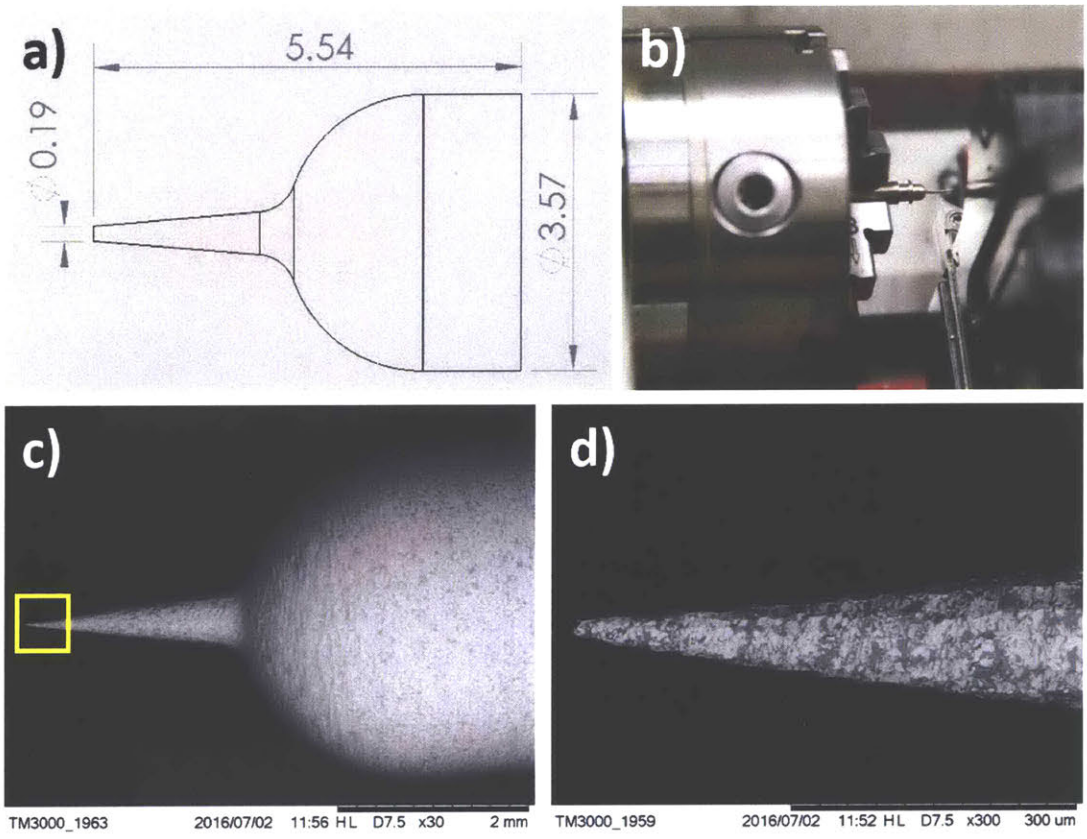

Figure 5-2: Metal machining of electrodes. a) CAD drawing of an electrode, the shape of which is the modeled after the interior of the injex ampoule. b) Electrodes are turned on the EMCO lathe, yielding c - d) electrodes with tips with diameters as small as 30 μm.

Machining graphite electrodes requires an additional setup for air evacuation, because the graphite particles produced during machining can present a health hazard. The mini-lathe was outfitted with an custom-built air evacuation system (Figure 5-3a) and HEPA filter that provided the industry standard flow rate for evacuation of graphite particulates [46]. The inlet tube holder provided two-axes of motion to

vacate debris directly from the tip region of the turning tool (Figure 5-3b). Graphite electrodes were thus readily machined using this method and imaged on the SEM (Figure 5-3c-d).

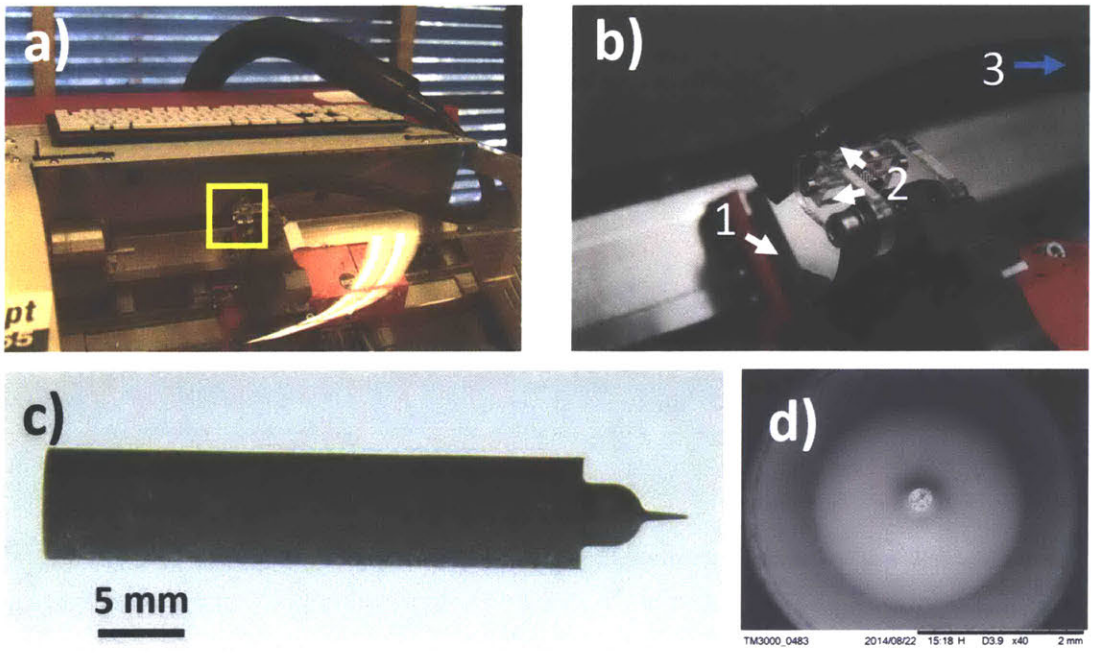

Figure 5-3: Graphite electrode machining. a-b) The EMCO mini-lathe was outfitted with a custom air evacuation and HEPA filter system to clear the air of graphite debris, yielding c-d) graphite electrodes.

Electrode Material Choice

Graphite, copper, tungsten, copper tungsten were assessed and tested for their suitability for nozzle machining. Characteristics relevant to sink EDM machining are summarized in Table 5.2.

Graphite is one of the most popular choices of electrode materials, due to their high resistance to heat in the spark gap, low thermal expansion, and absence of burrs in electrode machining. When graphite electrodes were used to machine nozzles however, little of the tip remained after one cycle because of the high tool removal rate (Figure 5-4). Because the shaft of electrodes are on the order of hundreds of microns and the tip is often on the order of tens of microns, the tip is composed of little material. As

such, a material with higher tool removal rate and higher density is advantageous.

Copper is also a popular choice in electrode materials. However, given its low modulus of elasticity 5.2, the electrode tip deforms easily during machining (Figure 5-4), rendering the electrode unusable.

Tungsten is favorable because of its high density, high melting point, and low thermal expansion. However, tungsten electrodes had a tendency to melt and re-solidify on the electrode tip, drastically changing the geometry of the electrode.

Copper tungsten was finally chosen because of its favorable melting point, high density, and low tool removal rate (Figure 5-4).

Workpiece Material Choice

Three materials were tested for sink EDM machining: stainless steel alloy 316, stainless steel alloy 420, and carbon steel alloy 1045. Their characteristics are summarized in Table 5.3.

Because of their resistance to rust, nozzles composed of stainless steels have the advantageous ability of maintaining their original contour even after multiple uses or long exposure to water. However, the higher the content of non-ferrous materials such as chromium and magnesium, the lower the content of iron and carbon, the more difficult to erode by spark. Consequently, the machining of stainless steel nozzles consistently yielded non-circular orifices or took more time to machine (Figure 5-5a-b).

1045 carbon steel was eventually chosen because of its high iron and carbon content. Nozzles machined using this material consistently yielded orifices of greater regularity and circularity (Figure 5-5c).

5.2.3 Micro-drilling and Sink EDM Fabrication

The first fabrication method attempted was to directly sink the workpiece using an electrode, of whose shape represented the desired nozzle interior. Because of the significant tool wear rate however, as much as 30 - 40% of the length of the electrode

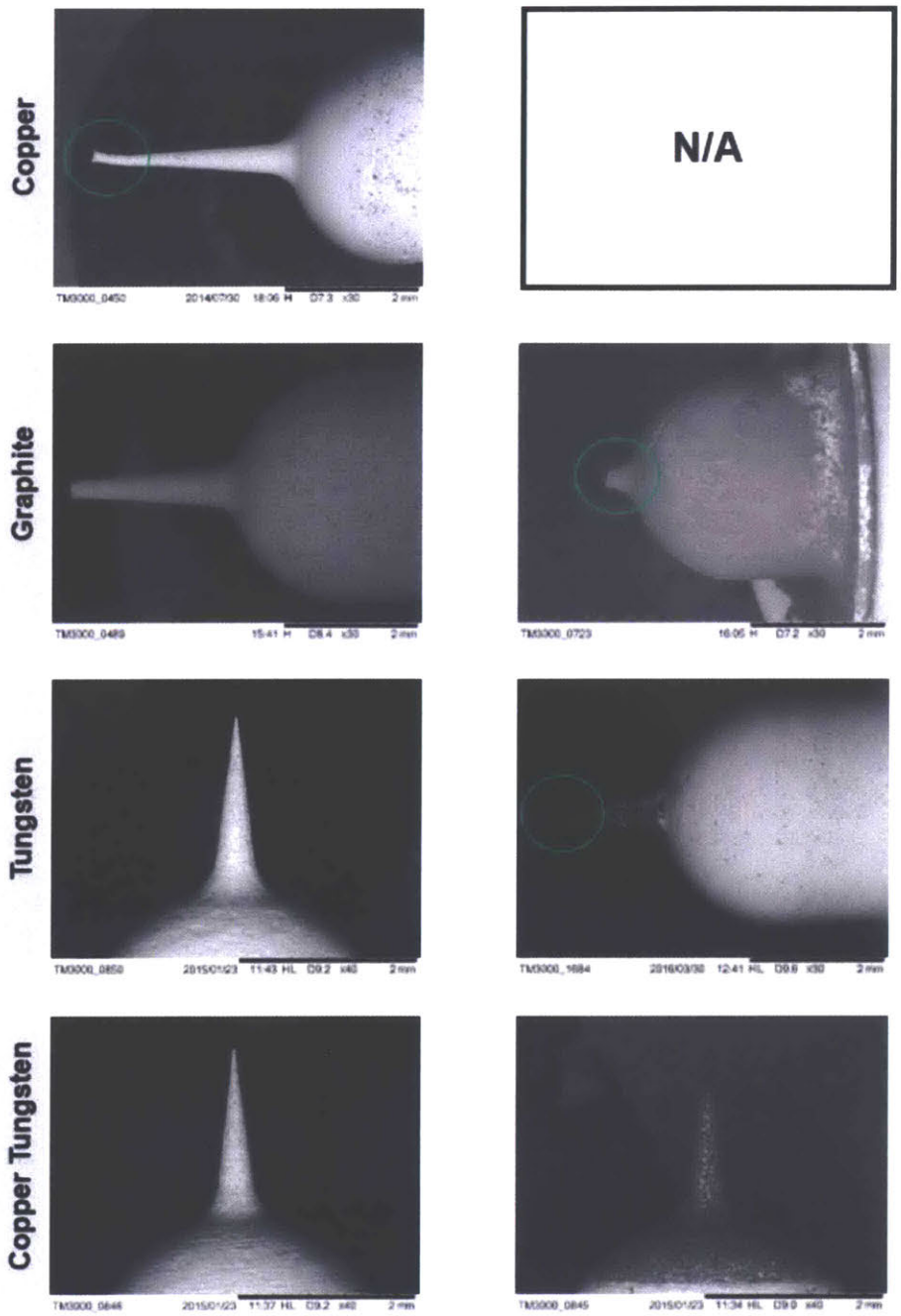

Figure 5-4: Sink EDM electrode using different materials. Left column pictures show fresh electrodes, right column of pictures show electrodes after machining to show tool wear.

tip was eroded (Figure 5-4), even with the improved tool wear characteristics of CuW.

To mitigate these issues, a three-stage fabrication process is developed (Figure

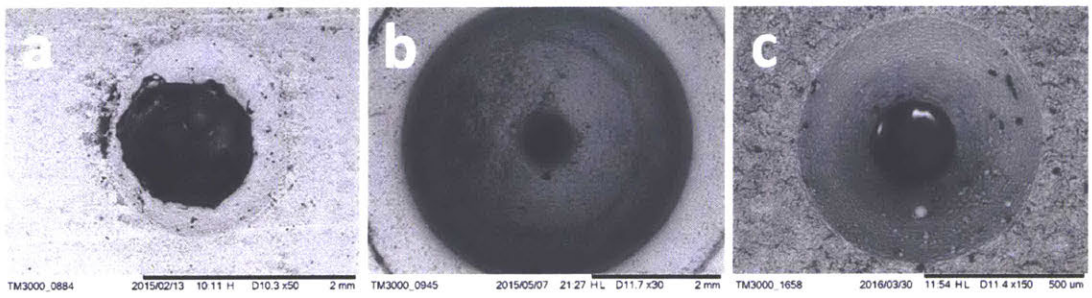

Figure 5-5: Materials are imaged on the SEM after sink EDM machining: a) stainless steel 316, stainless steel 420, and carbon steel alloy 1045.

5-6). In the first step, micro-drilling is used remove the bulk of the material in the workpiece. In the second step, a thin electrode is used to machine the nozzle orifice. In the third step, a larger electrode with a tip on the order of 20 - 30 μm in diameter is machined. Because the tip diameter is less than the diameter of the narrow region machined in the second stage, it is can be used as a probe to edge-find the center of the narrow region using electric contact. This larger electrode then is used to machine the larger orifice entrance geometry. Because micro-drilling was found to consistently machine circular orifices, another smaller micro-drilling step could be introduced after the first micro-drilling step to machine the orifice exit geometry, yielding a four-stage process.

5.2.4 Post-processing

Orifices with interior burrs and non-circular exit geometries presented challenges in nozzle machining. These obstructions to flow can cause the jet to disperse. A post-processing method was developed to address these challenges remove interior burrs and increase circularity. A typical sandblaster was modified (Figure 5-7a) to host nozzle inserts that produce dispersed jets (Figure 5-7b). When fine aluminum oxide particles (1200 grit, 3.6 μm radius) are forced through the orifice, the interior burrs and were lessened, and the nozzle insert produces a jet of increased collimation (Figure 5-7c).

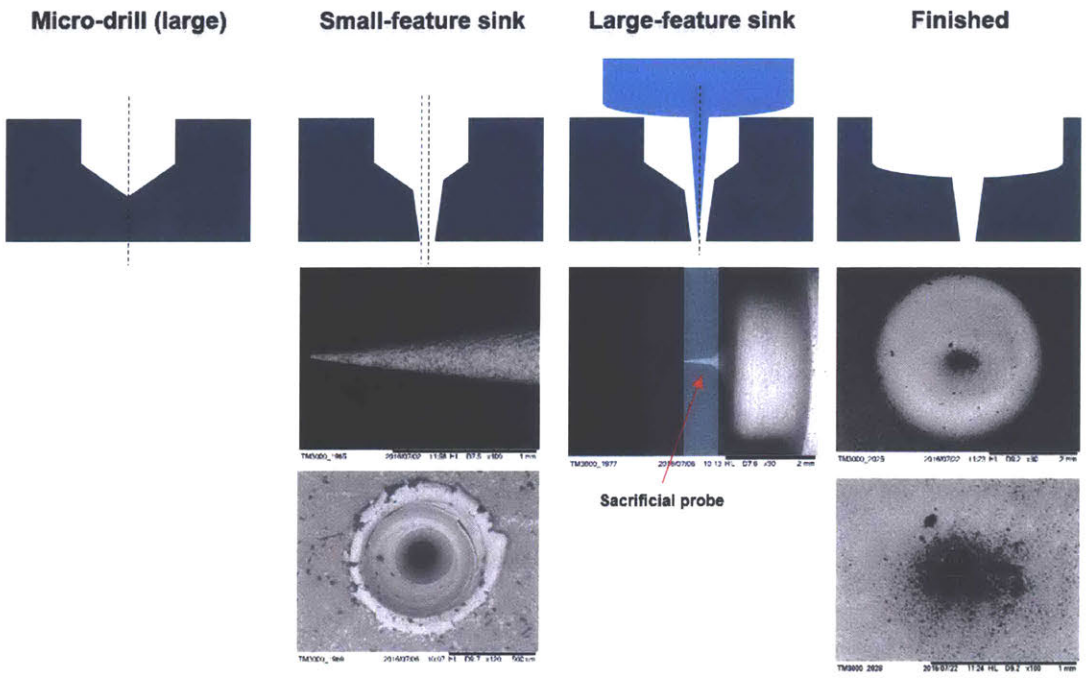

Figure 5-6: A fabrication method is developed that involves three stages of micro-machining: micro-drilling, small-feature sink, and large-feature sink.

5.3 Fabrication of Planar Nozzles

Cavitation within the nozzle is difficult to image in the traditional nozzle. The nozzles presented above are composed of optically opaque metal. While the Injex nozzle is made of polycarbonate, at the nozzle orifice, the thick walls are difficult for light to penetrate and the walls are curved. Even if the walls were optically clear, cavitation around the circumference of the interior wall would obscure the camera's line of sight and render imaging a cross-section of the cavitation challenging.

In the similar field of fuel injector nozzles, Sou and colleagues examined the relationship between cavitation and dispersion angle by fabricating and imaging 2D nozzles, consisting of two stainless steel plates to form the the sharp-edges at the inlet of a nozzle sandwiched between two acrylic flat plates [5]. The flow and cavitation inside the 2D nozzles were then imaged by a high-speed camera. Although the width of these 2D nozzles were an order of magnitude larger than the diameters common in needle-free injection, the tested Reynolds numbers ranging in the tens of thousands

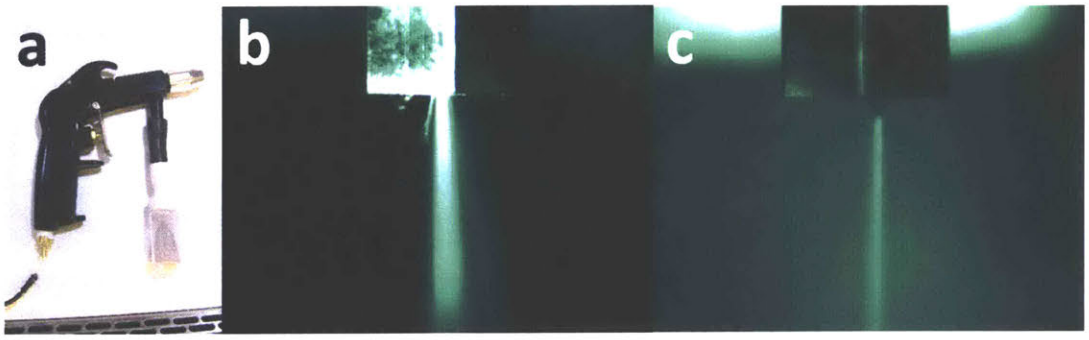

Figure 5-7: a) A post-processing method ejects an air-sand mixture to sands the interior of nozzles. b) Nozzles of dispersed jets produce c) collimated jets after post-processing.

is a similar range as that experienced in needle-free injection.

1 mm sheet aluminum was first cut on the Wire Electrical Discharge Machine (Wire EDM) to form a monolithic structure of which the nozzle shape formed the interior shape (Figure 5-8). This piece was then sandwiched between laser cut 7 $\times$ 7 $\times$ 1 mm optically clear cast acrylic and bonded using a combination of Loctite Super Glue Liquid Professional and Weld-on 4 Acrylic Cement. After bonding, the top of the structure was then grinded off to form the nozzle inlet opening, then bonded to a circular adapter to fit into the multi-piece ampoule (Figure 5-9). To further reinforce the hydraulic seal between the three plates, screws and nuts were also tightened on either side of the nozzle walls.

The minimum orifice height of the 2D planar nozzles was limited at 1 mm, because a sufficient contact area is required between the acrylic walls and aluminum insert given the bond strength of the current fabrication technique. Improving the bonding techniques between acrylic and aluminum or developing a method to fabricate monolithic, optically-clear structures could expand the range of geometries in 2D planar nozzles that can be imaged for cavitation.

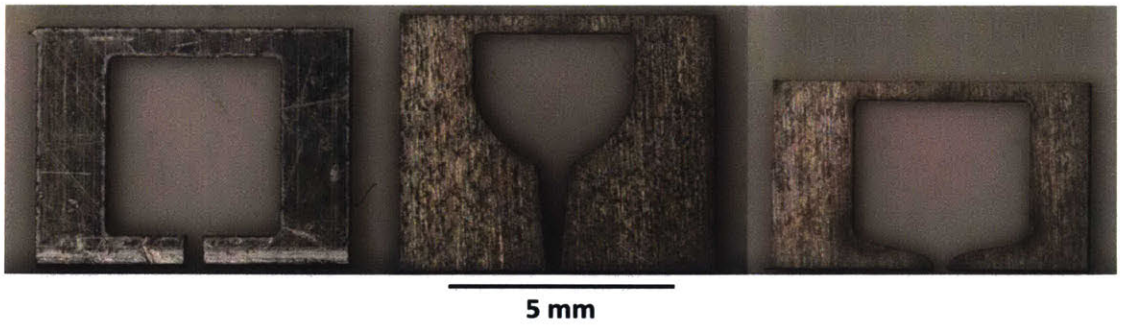

Figure 5-8: 1 mm sheet aluminum is cut on the Wire EDM to form a monolithic aluminum structure of which the nozzle shape forms the interior cut-out. The cut-outs of the following geometries are shown: cylindrical, Injex, and optimized planar nozzle

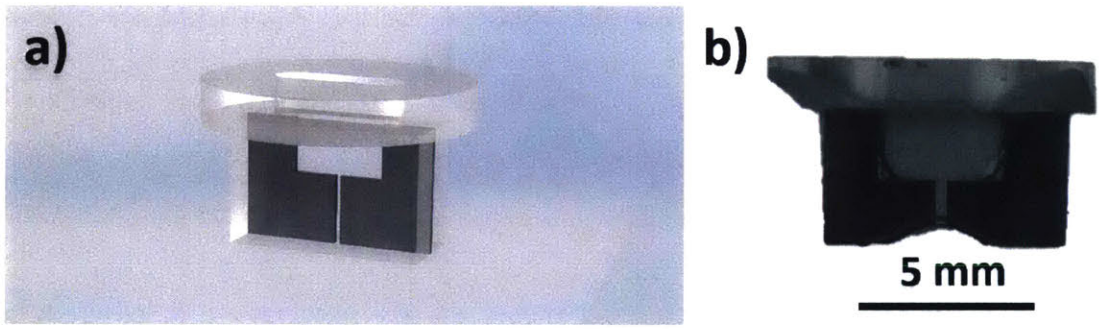

Figure 5-9: The 2D clear nozzle is composed of a two aluminum plates cut by wire EDM, sandwiched between two optically clear cast acrylic walls, and attached to an circular adapter to fit into the multi-piece ampoule. A 2D version of the cylindrical nozzle was a) first designed in CAD then b) fabricated and tested.

5.4 Manufacturing Informed Geometry Optimization

Recall that the minimum height for fabrication of 2D nozzles was determined by the bonding between the acrylic and metal nozzle walls. Manufacturing insights can further inform geometry optimization and are explored below.

5.4.1 Planar Nozzle Optimization

With a minimum height of 1 mm for 2D nozzles, the minimum length in the 2D optimization space was increased from 0.5 to 1 mm. An new objective function can be defined as:

$$Z_3 = res_L + res_{cav1} + res_{s,planar},$$

where $res_{s,planar}$ is defined as

$$res_{s,planar} = \begin{cases} 0, & \text{if } z > 1mm \\ \infty, & \text{if } z < 1mm. \end{cases} \tag{5.1}$$

Figure 5-10a shows the objective function Z_3, yielding the TF0.05L1 nozzle (Figure 5-10b) as the optimized geometry and was chosen for fabrication.

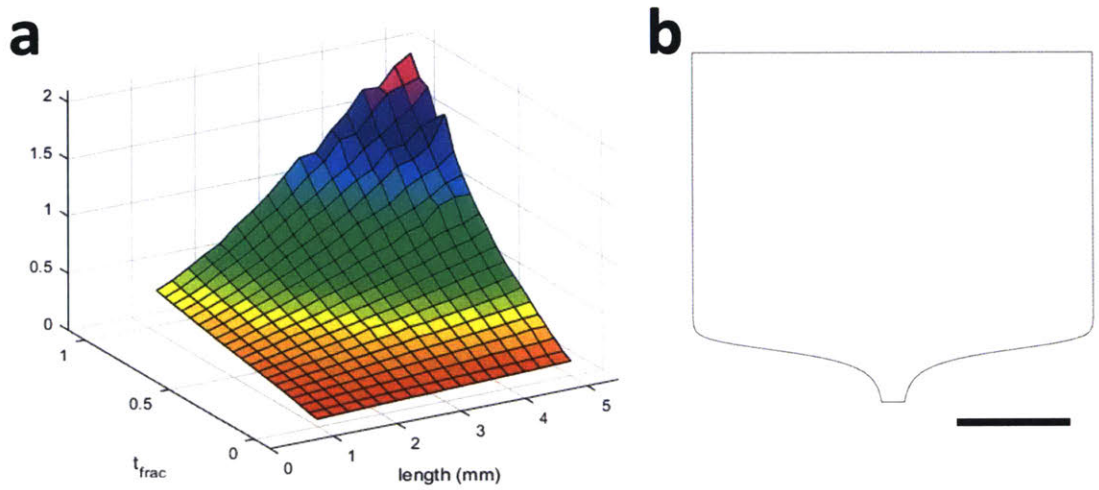

Figure 5-10: Planar Nozzle Optimization: a) the planar nozzle objective function and b) the optimized geometry for planar nozzles. (Scale bar = 1 mm.)

5.4.2 Polycarbonate Axisymmetric Nozzle Optimization

Injection molding polycarbonate is commonly used to mass manufacture needle-free injector ampoules. While fabricating injection molded nozzles was out of the scope of the work of this thesis, the stress in nozzle walls caused by the pressure of fluid flow acting on the nozzle walls of different nozzle geometries can be used to inform nozzle geometry optimization.

Model Setup

Using the fluid-structure module of COMSOL Multiphysics, a stationary study was set up to simulate the two-way interaction between the fluid flow within the nozzle and deformable nozzle walls. The geometry is composed of the nozzle interior through which fluid flows and nozzle walls (Figure 5-11).

The inlet (side a) condition is a uniform velocity that matches the piston's travel of 0.562 m/s. Side b is the axis of symmetry around which the rest of the 2D geometry is revolved to form the 3D geometry. The outlet of the nozzle is side c and is set at atmospheric pressure. A no-slip condition is imposed on the orifice and ampoule wall (side d). Only side e is fixed, atmospheric pressure is placed on sides f and g. The mesh on side b is prescribed to zero r-displacement, whereas the mesh on sides a and c are prescribed to zero z-displacement.

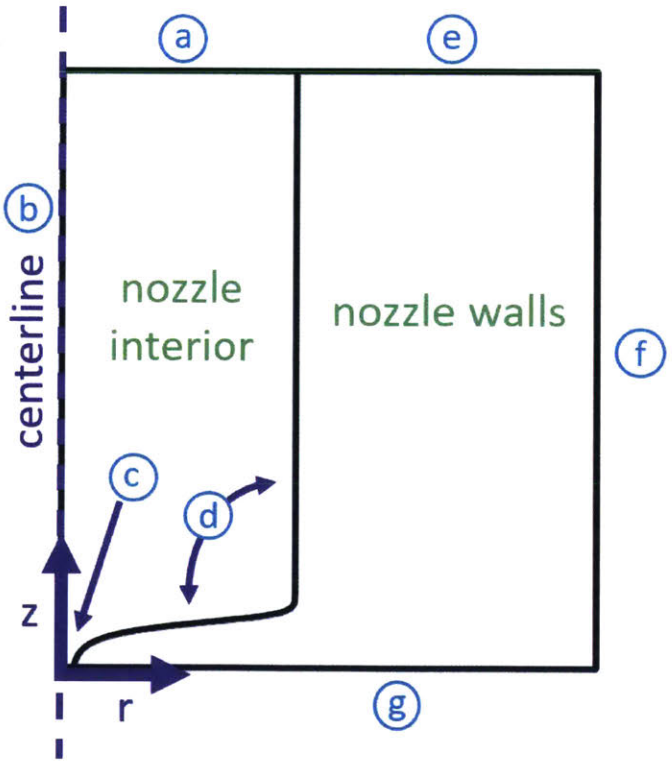

Figure 5-11: Fluid-structure model setup: geometry and boundary conditions.

Results

Polycarbonate under stress experiences two types of failure modes: brittle and ductile [47]. The stress, σ, required to make a crack to propagate is

$$\sigma = \frac{CK_{1c}}{\sqrt{\pi a}},$$

where C is a constant near unity, a is the crack length, K_{1C} is the plane-strain fracture toughness, 3 MPa·$m^{0.5}$ [48]. Given that the maximum principal stress experienced in the entire space was 240 MPa, the minimum crack length that will propagate is 50 μm. This crack length in polycarbonate is considered unlikely in injection molded polycarbonate nozzles where the smallest feature size is on 200 μm or less. It is concluded that the ductile mode is the most likely failure mode.

The strength of polycarbonate is 70 MPa [48]. Placed under the pressures of flow, many geometries will experience structural failure, including the first optimized geometry, the TF0.025L0.5 (Figure 5-12a). Nozzle geometries that experience more gradual transitions of pressure do not fail (Figure 5-12b).

A structural residual, $res_{s,polyc}$, can be defined as the ratio of the maximum von Mises stress over the strength:

$$res_{s,polyc} = \frac{max(\sigma_{Vmises})}{\sigma_f},$$

where σ_f is the strength and $sigma_{Vmises}$ is the von Mises stress in a given nozzle geometry. The plot of $res_{s,polyc}$ is shown in Figure 5-13.

A second manufacturing-informed objective function can thus be defined as

$$Z_4 = res_L + res_{cav1} + res_{s,polyc}.$$

The Z_4 objective function is shown in (Figure 5-14a). The nozzle geometry with the minimum value in the objective function is the TF0.05L5 nozzle (Figure 5-14b). (Scale bar = 1 mm.)

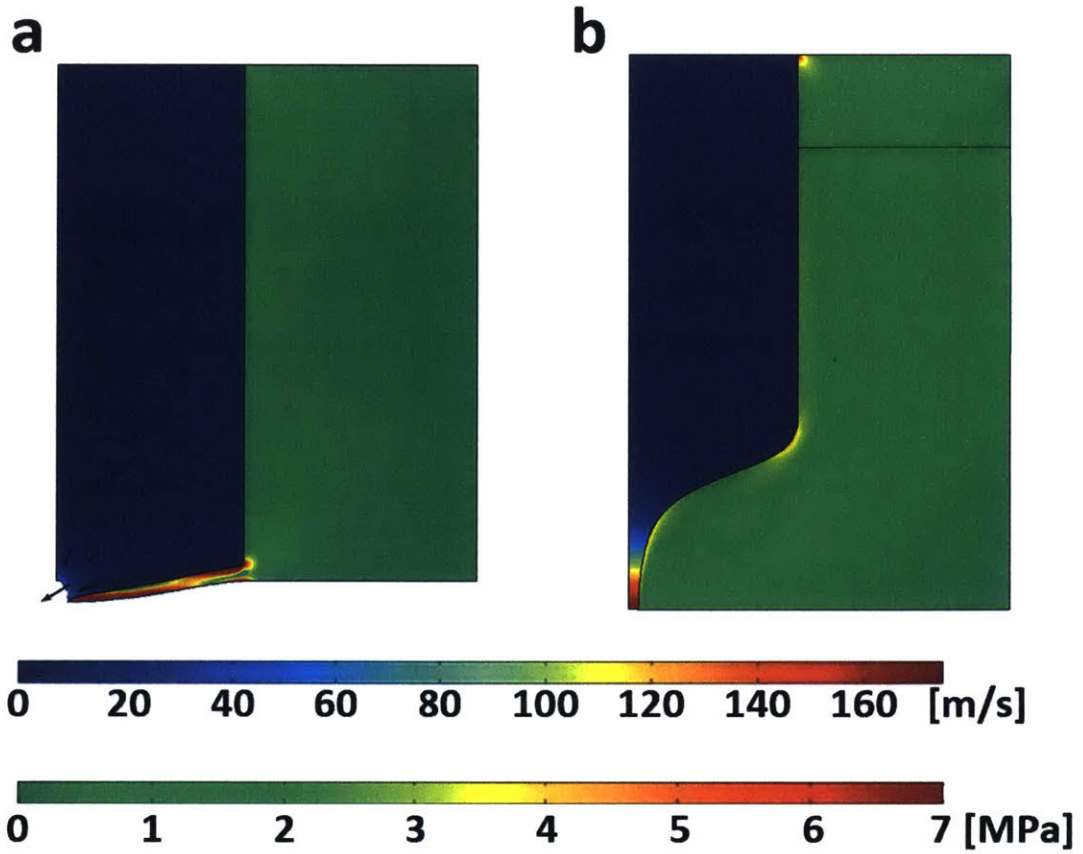

Figure 5-12: Total velocity and von Mises stress fields of nozzles. Polycarbonate nozzles of geometries hosting large pressure gradients such as a) TF0.025L0.5, will fail, while other nozzle geometries such as the b) TF0.2L2 will not fail.

5.5 Summary

A novel nozzle manufacturing technique is developed using a combination of micro-drilling and sink electrical discharge machining to fabricate axisymmetric nozzle shapes. Optically clear planar nozzles are developed and fabricated to image cavitation within the interior of nozzles.

New residuals informed by the structural integrity of manufactured planar or polycarbonate axisymmetric nozzles, yielding two new optimized geometries. These new residuals are combined with the original metrics of efficiency and cavitation (from Chapter 4) to form optimization functions for planar or axisymmetric nozzles, and completing the framework for nozzle shape optimization (Figure **??**).

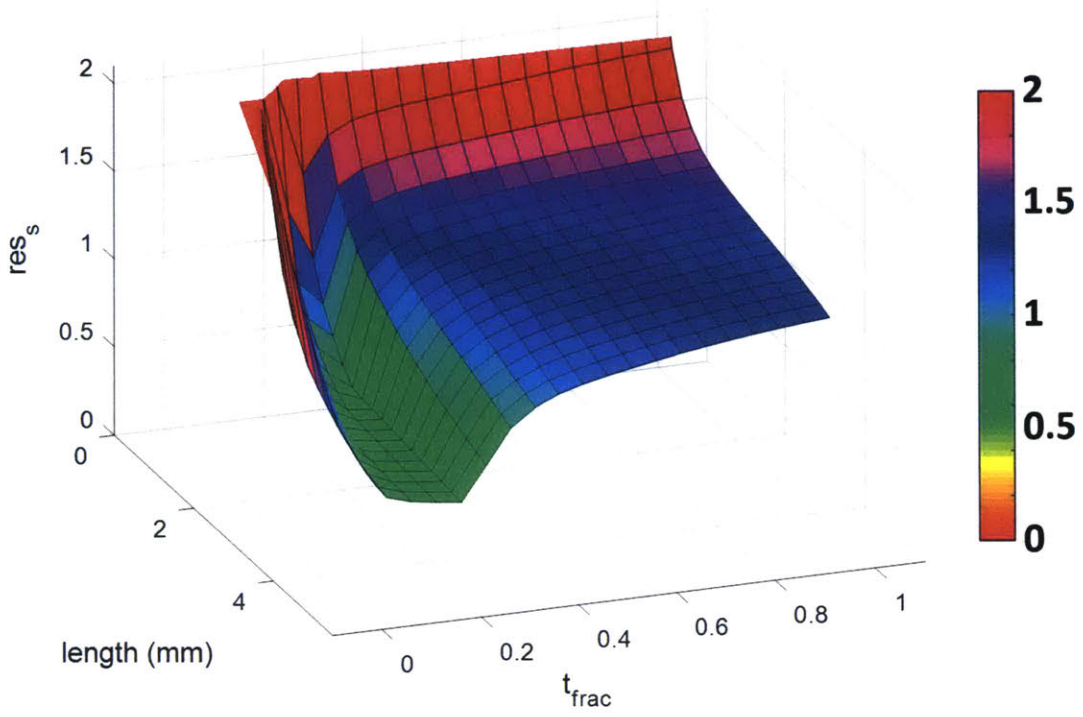

Figure 5-13: Structural residual for polycarbonate nozzles.

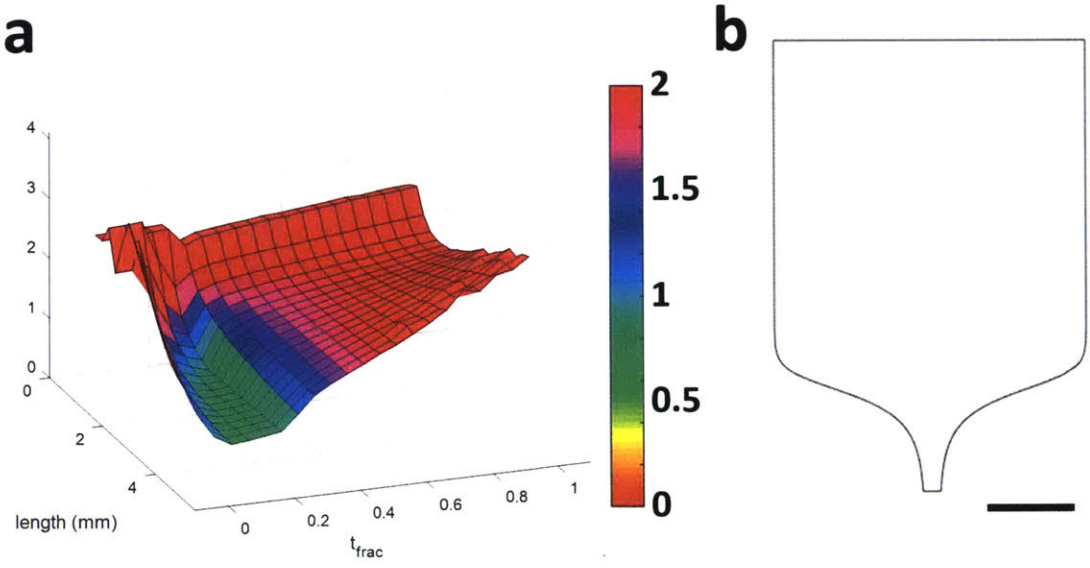

Figure 5-14: a) Manufacturing-informed objective function, b) the optimized nozzle for objective function Z_4.

Material	**Resisitivity (ohm·m)**	**Melting Point (°C)**	**Density (kg/m^3)**	**Hardness**	**Machinability**	**Modulus of Elasticity (GPa)**	**Thermal Expansion (10^{-6}/K)**
Graphite (B325)	1.4×10^{-5}	3350	2300	Shore Hardness 65	easy, but needs ventilation	11.36	5.9
Copper (Multi-purpose 110)	1.7×10^{-8}	1065	8900	Rockwell F65	too soft, will deform	117	16
Tungsten (90WCu4-Ni6)	5.6×10^{-8}	3422	17000	Rockwell C25	very hard, abrasive to cutting tool	400	4.5
Copper Tungsten (70W30Cu)	4.1×10^{-8}	3380 / 1085	13800	175 Hb	very hard, abrasive to cutting tool	220	10.3

Table 5.2: Characteristics of tested electrode materials.

Material	% Carbon	% Iron	Corrosion resistance
Stainless Steel 316	0.03 - 0.08	70.95	high
Stainless Steel 420	0.14 min	87.12	moderate
Steel 1045	0.42 - 0.50	98.75	low

Table 5.3: Characteristics of tested workpiece materials.

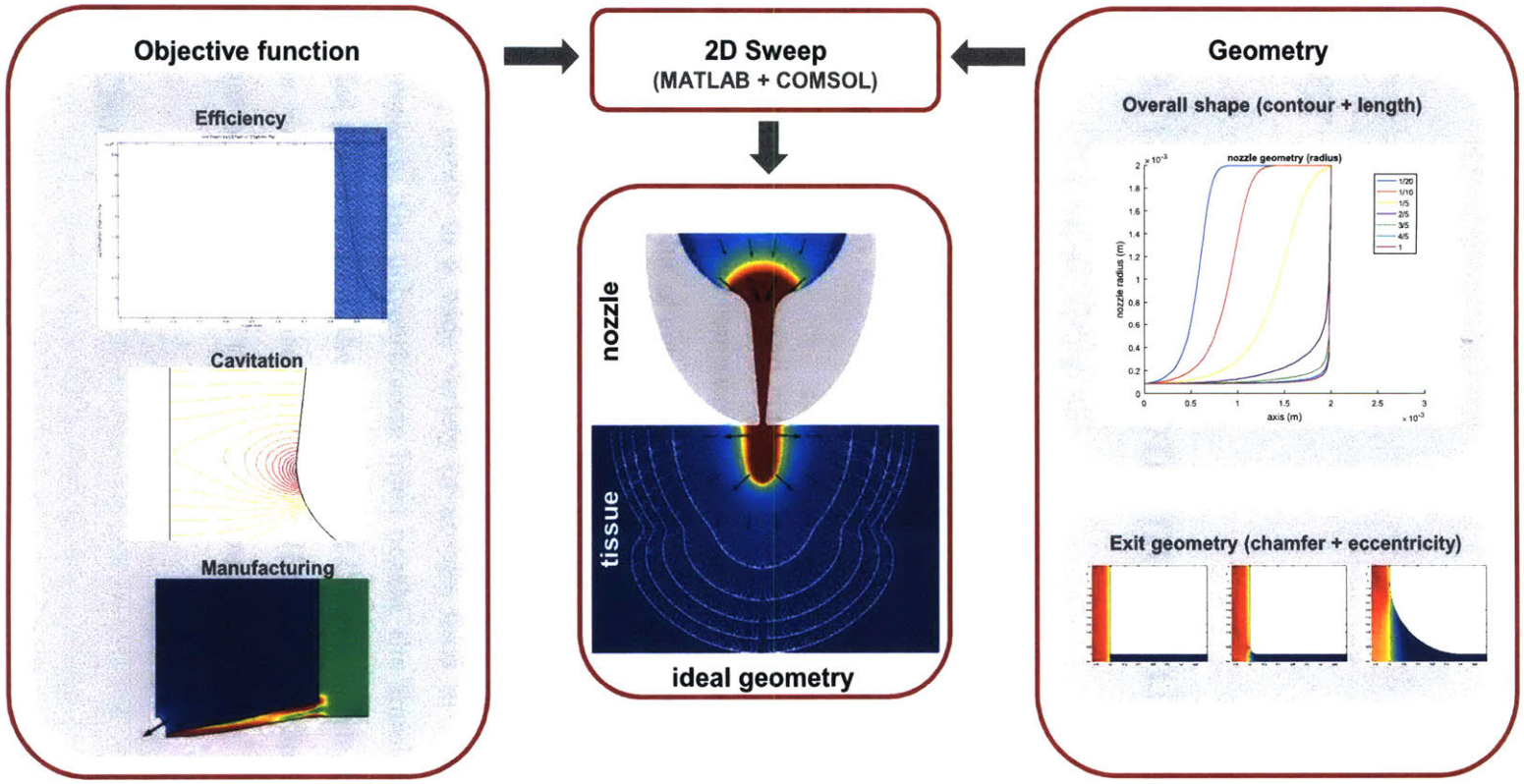

Figure 5-15: Overview of the final optimization framework for nozzle shape optimization.

Chapter 6

Comparisons of Commercial to Optimized Nozzles

6.1 Introduction

Using a mixture of experiments and computational tools developed in Chapters 3 and 4, the optimized nozzle is compared with commercially available nozzles. The Injex nozzle is the focal point of comparison because it is commonly accepted in the needle-free injection industry. The cavitation was imaged within planar nozzles of the shapes of Injex, cylindrical, and optimized planar nozzle.

Computational analysis will also be used to compare the efficiency and cavitation of the optimized nozzle to a wide variety of nozzles used in needle-free injection industry and research: the polycarbonate Injex nozzle, the stainless steel standard cylindrical orifice (1 mm length), the stainless steel O'Keefe nozzle, the ceramic SPT nozzle, and the jeweled Bird Precision 24 nozzle (Figure 6-1). For consistency, the optimized planar nozzle is used as the point of comparison.

6.2 Efficiency

The efficiencies of all nozzles are calculated and compared (Figure 6-2). The cylindrical orifice has the sharpest transition at the orifice exit (entrance angle of 0 degrees)

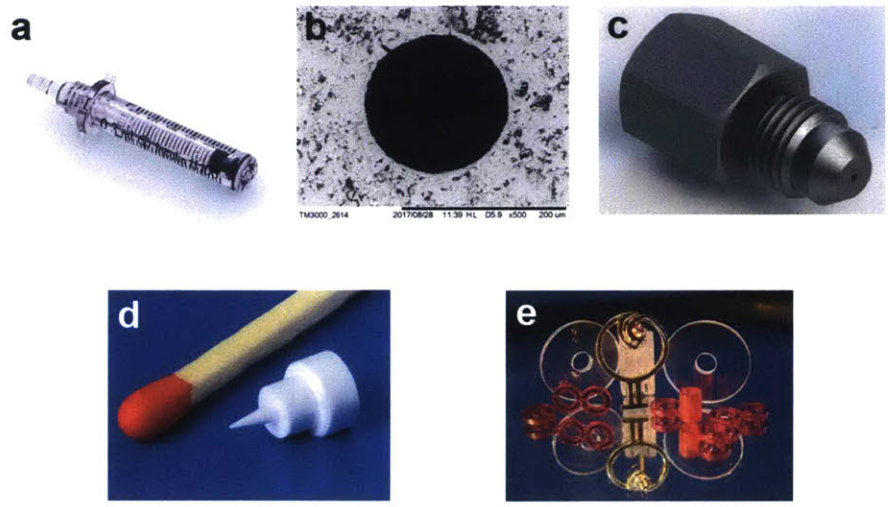

Figure 6-1: Nozzles commonly used in needle-free injection industry or research are compared to the optimized nozzle: a) Injex nozzle, b) cylindrical orifice, c) O'Keefe nozzle, d) SPT nozzle, and e) Bird Precision 24 nozzle.

and consequently yields the largest viscous loss and lowest efficiency. The Injex nozzle hosts a large exit fillet, 100 μm in radius, causing flow separation and flow expansion just above the fillet, and thus inducing viscous loss upstream from the orifice exit. The geometries of the O'Keefe, SPT, and Bird Precision 24 nozzles all employ a ampoule-orifice conical transition of various entrance angles to a cylindrical orifice similar to the geometry explored in the parametric study of entrance angle (Chapter 3). Viscous losses occur at the orifice transition, causing decreased efficiency. The efficiency of the optimized planar nozzle is the highest and is about 7% higher than that of the Injex nozzle.

6.3 Cavitation

Comparison of Simulated Cavitation

Using the streamline approach developed in Chapter 3, cavitation regions within commercially available nozzles and the optimized planar nozzle are simulated and shown in Figure 6-3. In the Injex nozzle the transition from ampoule diameter to nozzle di-

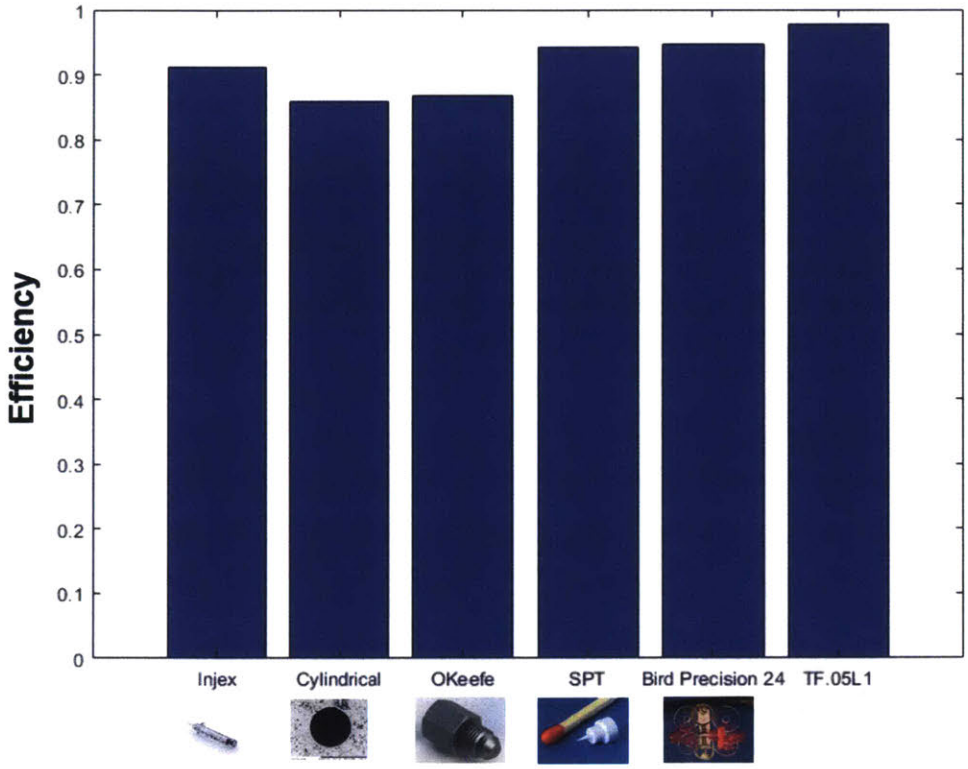

Figure 6-2: Efficiency comparison of commercial available nozzles with the optimized planar nozzle.

ameter is smooth, and no cavitation is predicted in the bulk of the interior. However, because Injex nozzle hosts a large exit fillet, 100 μm in radius, flow separation and flow expansion occurs just above the fillet, causing significant cavitation at the orifice. In nozzles used in needle-free injection research, sharp transitions at the orifice entrance cause cavitation in the orifice. Because the SPT nozzle has the largest entrance angle and therefore the most gradual transition, the cavitation is least. Little cavitation is perceived in the optimized planar nozzle.

The cavitation metric developed in Chapter 4 is used to quantify the difference of cavitation within each nozzle (Figure 6-4). The model predicts the cavitation in the cylindrical nozzle to be the largest. This is consistent with the findings of Chapter 3; sharper transitions at the orifice entrance increase flow separation and expansion. The simulated cavitation in optimized planar nozzle is four orders of magnitude less than

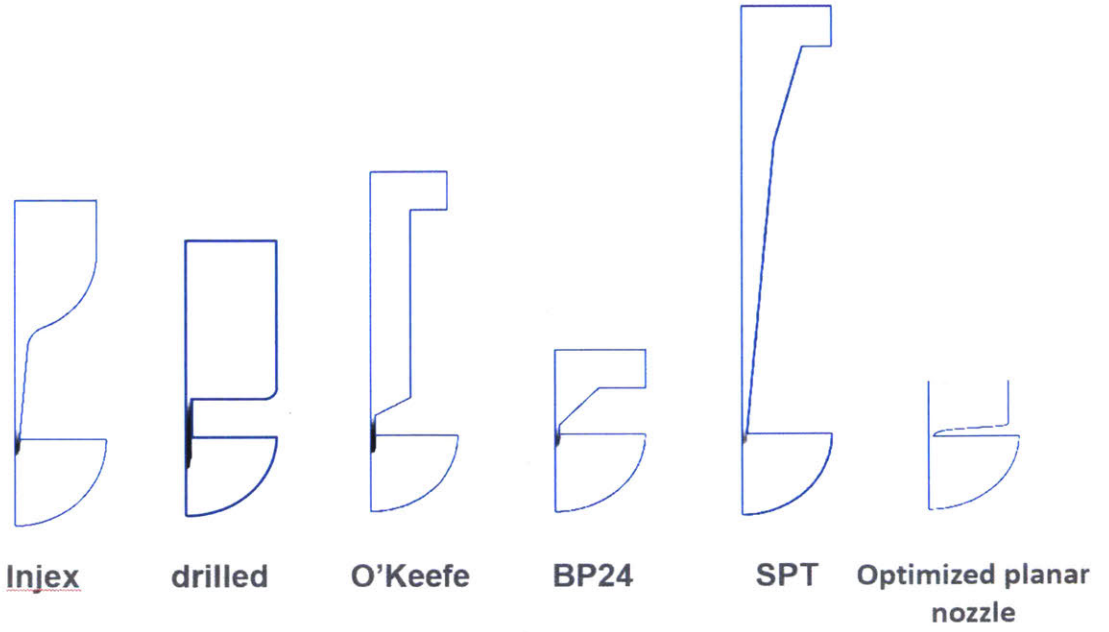

Figure 6-3: Comparison of simulated cavitation between commercial available nozzles and the optimized nozzle.

the cavitation in the cylindrical geometry and one to three orders of magnitude less than other nozzles commonly used in NFI research. Of note, the simulated cavitation in the optimized planar nozzle nozzle is about two orders of magnitude less than that of the Injex nozzle.

Cavitation Imaging

We seek to experimentally confirm the predictions of cavitation regions made by our streamline cavitation computational analysis. The planar nozzle was placed in between a high-speed camera (Phantom v2511, courtesy of the MIT Edgerton Lab) and a halogen LED lamp that shone directly through the planar clear nozzle into the camera lens, forming a back-lit imaging setup. The high-speed camera caught images at a rate of 50,000 to 75,000 fps, with an exposure time of 1 μs.

Given the backlit set up, cavitating bubbles most often appear as dark regions because bubbles scatter incoming light away from the camera lens and sensor. Significant cavitation is observed in the cylindrical nozzle (Figure 6-5). Note the initial

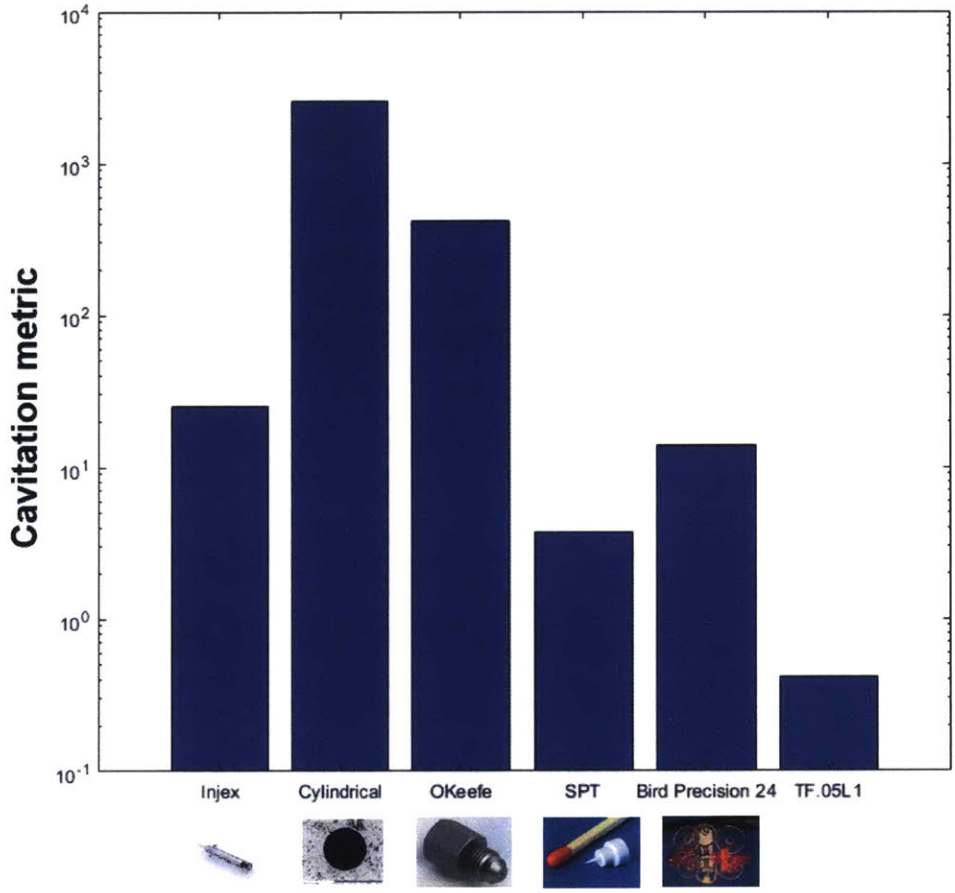

Figure 6-4: Cavitation metric comparison of commercial available nozzles with the optimized nozzle geometry.

water-air interface above the orifice entrance into the at t = 0 s. This interface is pushed downwards as the ejection begins and water begins to push out of the nozzle at t = 0.436 ms. The growing cloud of cavitation bubbles reaches the the full length of the orifice at t = 1.399 ms.

Similarity of Simulations and Experiments

The cavitating bubbles are well above 1 μm and easily in the 10 to 50 μm range, which means that pressure is the dominant force, helping to further justify the assumption made for the streamline approach in simulating cavitation in Chapter 2 to neglect viscous and surface tension terms and only include the pressure forcing

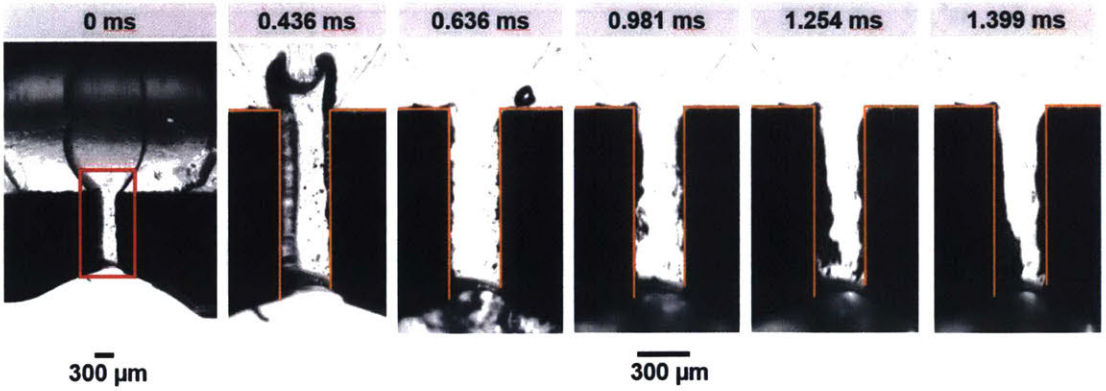

Figure 6-5: Imaged cavitation within the planar nozzle of the cylindrical shape. Cavitating bubbles appear as dark patches because they refract and scatter the light away from the camera lens and sensor. The red box in the first frame indicates the area of zoom of the subsequent frames. Orange lines denote the nozzle walls to distinguish between the dark wall and cavitation in the orifice.

term. On the other hand, if these bubbles were to grow still larger and combine with other large bubbles to form regions of gas, these regions would be fixed at cavitation pressure [37] instead of the pressures in the negative MegaPascals predicted by CFD simulations. If so, then our cavitation tool could be significantly inaccurate. When the cloud of cavitation grows larger beyond 1.254 ms, it is unclear in the time-lapse images whether the bubbles are combining to form regions of gas or whether they are primarily surrounded by fluid.

How similar are the flow and cavitation in these planar nozzles as compared to the simulations of 2D axisymmetric nozzles? Two comparisons on the observable structures within the flow of these two scenarios suggest promising accuracy of these simulations.

The regions of cavitation as predicted by the streamline approach are compared with cavitation imaged in the planar nozzle (Figure 6-6). While the cavitation clouds of both corners do not meet at axis as simulated, the general structure is the same; a start at the sharp-corner and an extension of the cavitation down the length of the orifice and beyond the exit. This visual comparison helps confirm the accuracy of the cavitation prediction tool developed in Chapter 2.

A time-dependent, axisymmetric study of a two-phase (air and water) CFD sim-

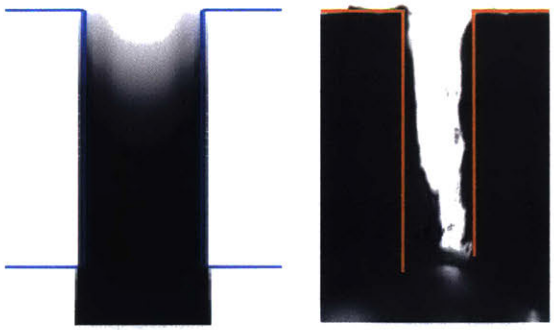

Figure 6-6: Side-by-side comparisons between the simulated (left) and imaged cavitation (right), where orange lines in the cavitation image indicate the nozzle walls. Black regions represent regions of cavitation in both simulated and imaged cavitation.

ulation of a water ejection into atmospheric air was carried out in COMSOL. The initial water-air interface was placed slightly above the orifice exit. As water is ejected from the nozzle with increasing speed, the slowly moving jet front will bunch up and be pushed out by the faster traveling fluid behind it, eventually forming a "curling lip" (Figure 6-7). The simulations predict this curling lip for a large range of geometries, provided the initial interface is near the orifice exit. In the planar nozzle experiment, when we are careful to control the water such that the water-air interface is located slightly above the orifice exit, the same behavior is seen (Figure 6-8).

It is worth noting that the development of the curling lip are on different timescales. The imaged curling lip forms over the course of about 1 ms, because the timescale for the power amplifier and motor to ramp up to maximum current and force is on the order of 1 ms. In the simulation however, the computation cost was conserved by decreasing the timescale of the inlet velocity ramp 1 μs and the study was studied the behavior of the jet shape over the first 15 μs.

While the simulation failed after the tip of the lip curled inward and collided with the main body of the jet, imaging of flow in the planar nozzles reveals that the curling lip develops until t = 0.613 ms, after which it is pierced through by the fluid moving behind it, the fast-moving fluid that ultimately forms the jet.

The similarity between the initial flow structure predicted by simulations and that imaged in the planar nozzles, demonstrates further promise that the flow within these

planar nozzles are similar to the 2D axisymmetric flows that are simulated.

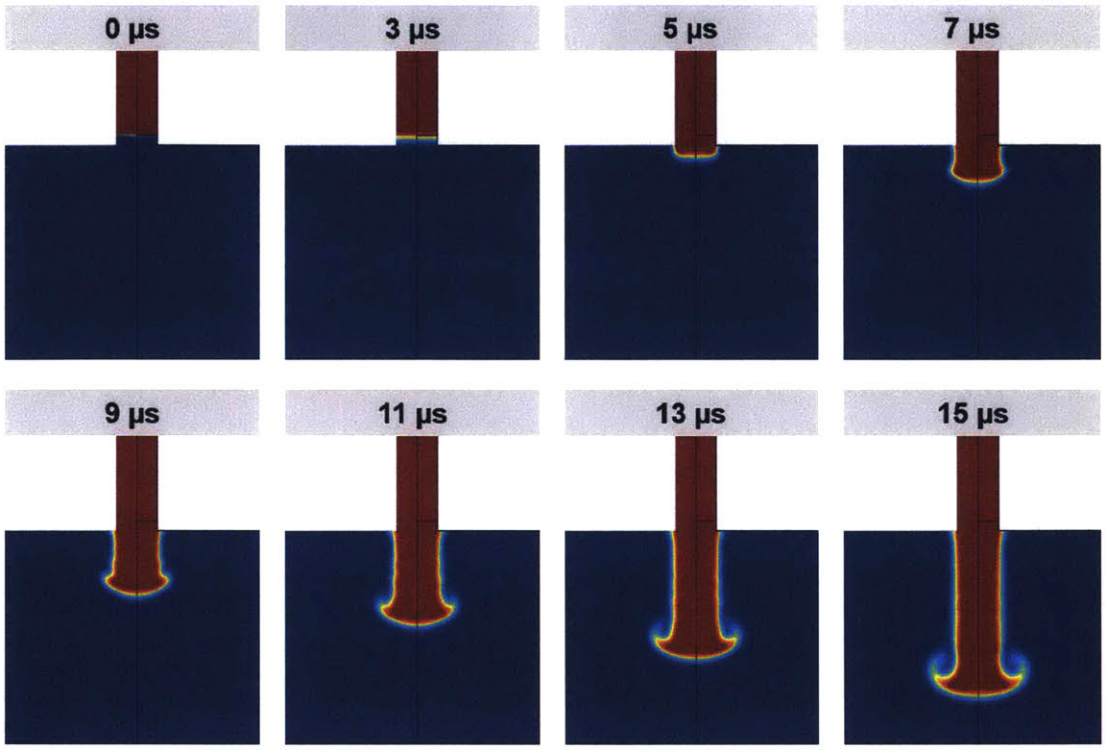

Figure 6-7: COMSOL simulation of an ejection of water into atmospheric air. Regions of blue are occupied by air and regions of red are occupied by water. As water is ejected from the nozzle with increasing speed, the slowly moving jet front bunches together and is pushed out by the faster traveling fluid behind it, eventually forming a "curling lip".

Comparison of Imaged Cavitation

We now experimentally compare the cavitation in the different nozzles of interest by choosing to image the flow in few representative planar nozzles: the cylindrical, injex, and optimized planar nozzle. We compare side-by-side the snapshot of greatest cavitation in each of the planar versions of these nozzles (Figure 6-9). Here we see that the amount of cavitation differs in the different geometries: cavitation extends throughout the entire length of the orifice in the cylindrical geometry, the cavitation is only present just above the exit expansion of the Injex nozzle, and little cavitation is present in the optimized planar nozzle.

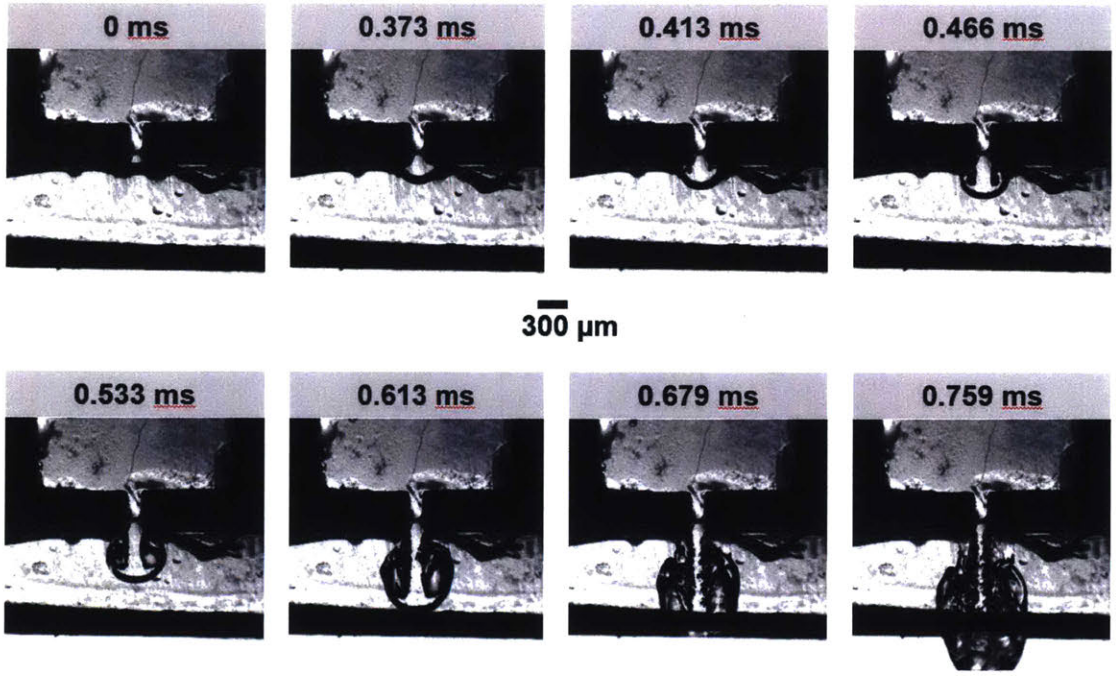

Figure 6-8: The curling lip is imaged in the fluid flow of planar nozzles. The curling lip develops until t = 0.613, after which the faster moving fluid behind the curling lip penetrates through to form the jet.

6.4 Summary

By computational analysis, the optimized planar nozzle is more efficient than any commercial nozzle and specifically, 7% more efficient and than the Injex nozzle. The cavitation structure and curling-lip imaged in planar nozzles are similar to the structures predicted in simulations, demonstrating promise in the accuracy of the simulations presented in this thesis. The planar nozzle causes one to three orders of magnitude less cavitation than research NFI nozzles, and two orders of magnitude less cavitation than the Injex nozzle.

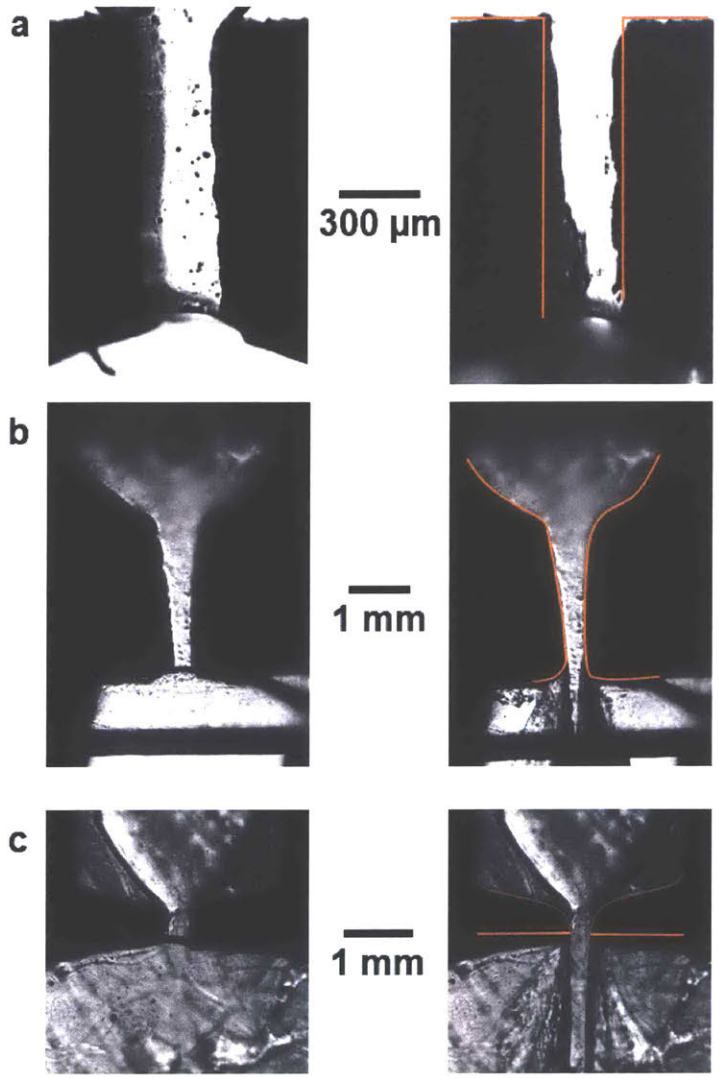

Figure 6-9: Imaged cavitation of three different nozzle geometries in the planar nozzle: cylindrical, Injex, and the optimized planar nozzle. Left column of pictures shows the nozzle at t = 0, where the black line near the orifice exit shows the initial water-air interface. The right picture column shows the nozzle at full flow, where orange lines indicate nozzle walls.

Chapter 7

Conclusion

This thesis presents the optimization of the nozzle shape for NFI application and the development of nozzle geometries.

An ampoule platform that houses different nozzle inserts has been developed and demonstrated, enabling a concentration on the design and fabrication of the nozzle geometry instead of the entire ampoule. The ampoule and piston are rigid and have increased controllability compared to its commercial counterparts. Nozzle geometries capable of producing non-axial jets are developed to expand needle-free injection modalities. These two novel geometries produce radial jets and intersecting jets, respectively. They are demonstrated through injection into tissue analog and *ex vivo* porcine tissue to have potential for intradermal and intratympanic membrane injections.

We examined via computational fluid dynamics studies how different geometric elements of the cylindrical orifice affect the characteristics of the flow in NFI nozzles such as viscous loss, mechanical efficiency, flow separation, and velocity field. These insights informed the optimization of the nozzle shape. We considered objective functions composed of combinations of loss, velocity field, and cavitation. After further examination of the effect of developing flow on penetration ability and required energy, we argued that plug flow is more advantageous than fully developed flow and chose to combine the residuals of loss and cavitation for the formation of an objective function. The time-dependent solutions to the 1D convection-diffusion equation was

chosen as the class of curves to represent the bulk shaping of velocity within the nozzle based on their properties and drastic decrease of degrees of freedom to span the range of shapes we are interested in. We used a 2D parametric sweep to find the optimal nozzle shape.

A novel nozzle manufacturing technique is developed using micro-drilling and sink electrical discharge machining to create axisymmetric nozzles that consistently produce collimated jets and do not deform over time. Optically clear 2D planar nozzles are also developed to offer experimental comparisons of cavitation that occur in nozzles of different shapes. The manufacturing of nozzles inform the creation of a third kind of residual based on the structural integrity of manufactured nozzles to form the final optimization function.

The optimized nozzle is compared to commercial nozzles using a combination of simulations and experiments. By computational analysis, the efficiency of the optimized nozzle is 7% to 50% greater than that of a commercial NFI nozzle and the cavitation is two orders of magnitude less. Imaging of the planar nozzles confirms that the cavitation in the optimized nozzle is significantly less than the cavitation in the commercial ampoule or drilled orifice.

7.1 Future Work

7.1.1 Experimental confirmation of optimization

The sink EDM failed near the end of this thesis work and the optimized nozzle is yet to be fabricated. An important step would be to fabricate the optimized nozzle and experimentally compare its efficiency, injection characteristics (such as injection depth or volume delivered), collimation, and dispersion angle with commercial nozzles.

7.1.2 Cavitation

This thesis explored for the first time the issue of cavitation in NFI and demonstrated promise in predicting and imaging cavitation. However, there still exists no direct and

quantitative relation between the amount of cavitation in a nozzle and final injection outcome. Thus in this thesis, we naively formed the final objective functions, Z_3 and Z_4, by equally weighting the three normalized residuals of efficiency, cavitation, and structural integrity equally.

Obtaining a quantitative relation between cavitation and injection characteristics (such as injection depth or volume injected) would further the creation of a more realistic objective function. Given how complex cavitation, two-phase flow, and tissue fracture are, these insights are likely best obtained through experimentation.

7.1.3 Device development and manufacturing

Nozzle mass manufacturing

One of the major issues with commercial NFI industry is the wide range of jet characteristics due to the manufacturing tolerances in the 3D orifice geometry of injection molded nozzles, traditionally favored because of its low-cost for mass manufacturing. While the nozzle fabrication technique presented in this thesis has the capability of fabricating nozzles to appropriate tolerances, it requires many steps and is time-consuming. The time to manufacture a particular geometry could be introduced in the objective function for an optimization of greater scope and realism. Secondly, it would be helpful to explore different manufacturing methods to find the optimal method and material for mass manufacturing, tight tolerances, and biomedical application. One final work that would be of interest is the design of a compliant nozzle such that the manufacturing deviations from the intended nozzle geometry deform to the pressure gradient experienced in the flow of the nozzle interior to still produce the originally intended nozzle shape.

Non-axial nozzle geometries

The space of possible needle-free injection modalities is as wide as the space for medical injections. A narrow three-orifice nozzle, one to shoot axially downwards and two to shoot diagonally downwards and outwards within the same plane could

be developed for the cosmetic industry to fill wrinkles. A nozzle composed either of a rifled orifice geometry or of two off-axis cylindrical orifices slightly spaced apart could produce one spiraling jet to enhance a jet's ability to penetrate tissue. Finally, a thin and wide orifice could be fabricated to produce radial sheets of flow to penetrate tissue, and take advantage of tissue anisotropy by traveling between tissue layers instead of through tissue layers for increased efficiency of drug delivery.

Chapter 8

Bibliography

[1] A. Taberner, N.C. Hogan, and I.W. Hunter. Needle-free jet injection using real-time controlled linear lorentz-force actuators. *Med. Eng. Phys.*, 34(9):1228–1235, 2012.

[2] A. Modak, N.C. Hogan, and I.W. Hunter. Adaptive controller for a needle free jet-injector system. In *Conf. Proc. IEEE Eng. Med. Biol. Soc. 2015*, pages 7345–7349, August 2015.

[3] G. Park, A. Modak, N.C. Hogan, and I.W. Hunter. The effect of jet shape on jet injection. In *Conf. Proc. IEEE Eng. Med. Biol. Soc. 2015*, pages 7350–7353, August 2015.

[4] J. Liu, N. C. Hogan, and I. Hunter. Ampoule and nozzle development for needle-free injections. In *Conf. Proc. IEEE Eng. Med. Biol. Soc. 2017*, pages 304–308, 2017.

[5] A. Sou, S. Hosokawa, and A. Tomiyama. Effects of cavitation in a nozzle on liquid jet atomization. *Int. J. Heat Mass Transfer*, 50:3575–3582, 2007.

[6] F. M. White. *Fluid Mechanics.* McGraw Hill, 2003.

[7] Reliable EDM. *Complete EDM Handbook*, 2016.

[8] E. L. Giudice and J. D. Campbell. Needle-free vaccine delivery. *Adv. Drug Deliv. Rev.*, 58(1):68–89, 2006.

[9] J. Jagger, E. H. Hunt, and R. D. Pearson. Estimated cost of needlestick injuries for six major needled devices. *Infect Control Hosp. Epidemiol.*, 11:586–588, 1990.

[10] A. Prüss-Ustün, E. Rapiti, and Y. Hutin. Estimation of the global burden of disease attributable to contaminated sharps injuries among health-care workers. *Am. J. Ind. Med.*, 48(6):482–490, December 2005.

[11] Safe Needle Disposal. Safe needle disposal: The problem. `http://www.safeneedledisposal.org/general-information/the-problem`, (accessed February 24, 2016).

[12] M. A. F. Kendall. Needle-free vaccine injection. In Monika Schäfer-Korting, editor, *Handbook of Experimental Pharmacology: Drug Delivery*, pages 193–219. Springer, 2010.

[13] World Health Organization PATH. Intradermal delivery of vaccines: A review of the literature and the potential for development for use in low- and middle income countries. `http://www.safeneedledisposal.org/general-information/the-problem`, 2009 (accessed February 24, 2011).

[14] J. C. Stachowiak, T. H. Li, A. Arora, S. Mitragotri, and D. A. Fletcher. Dynamic control of needle-free jet injection. *J. Control Release*, 135(2):104–112, 2009.

[15] N. C. Hogan, A. J. Taberner, L. A. Jones, and I. W. Hunter. Needle-free delivery of macromolecules through the skin using controllable jet injectors. *Expert Opinion Drug Delivery*, 23(10):1637–1648, 2015.

[16] R. Williams, B. Ruddy, N.C. Hogan, I.W. Hunter, P. Nielsen, and A. Taberner. Analysis of moving-coil actuator jet injectors for viscous fluids. In *Conf. Proc. IEEE Eng. Med. Biol. Soc. 2015*, pages 1–4, August 2015.

[17] A. B. Raynal, N. C. Hogan, and I. W. Hunter. Design of a debridement device using impinging jets. *J. Med. Devices*, 20(3), 2016.

[18] COMSOL Multiphysics. *COMSOL CFD User Guide*, 2017.

[19] B. D. Hemond, A. Taberner, C. Hogan, B. Crane, and I. W. Hunter. Development and performance of a controllable autoloading needlefree jet injector. *Journal of Medical Devices*, 5(1):015001–1 - 015001–7, 2011.

[20] J. Schramm-Baxter, J. Katrencik, and S. Mitragotri. Jet injection into polyacrylamide gels: investigation of jet. *Journal of Biomechanics*, 37:1181–1188, 2004.

[21] J. Schramm-Baxter and S. Mitragotri. Needle-free jet injections: dependence of jet penetration and dispersion in the skin on jet power. *Journal of Controlled Release*, 97(3):527–537, 2004.

[22] F. Payri, V. Bermudez, R. Payri, and F.J. Salvador. The influence of cavitation on the internal flow and the spray characteristics in diesel injection nozzles. *Fuel*, 83(4):419 - 431, 2004.

[23] R. Payri, J.M. Garcia, F.J. Salvador, and J. Gimeno. Using spray momentum flux measurements to understand the influence of diesel nozzle geometry on spray characteristics. *Fuel*, 84(5):551 - 561, 2005.

[24] R. Payri, F.J. Salvador, J. Gimeno, and L.D. Zapata. Diesel nozzle geometry influence on spray liquid-phase fuel penetration in evaporative conditions. *Fuel*, 87(7):1165 - 1176, 2008.

[25] J. Schramm and S. Mitragotri. Transdermal drug delivery by jet injectors: Energetics of jet formation and penetration. *Pharmaceutical Research*, 19(11), 2002.

[26] J. Baxter and S. Mitragotri. Jet-induced skin puncture and its impact on needle-free jet injections: Experimental studies and a predictive model. *Journal of Controlled Release*, 106:367–373, 2005.

[27] O. A. Shergold and N.A. Fleck. Mechanisms of deep penetration of soft solids, with application to the injection and wounding of skin. *Proc. R. Soc. London*, Ser. A(460):3037–3058, 2004.

[28] O. A. Shergold, N. A. Fleck, and T. S. King. The penetration of a soft solid by a liquid jet, with application to the administration of a needle-free injection. *Journal of Biomechanics*, 39(14):2593–2602, 2006.

[29] K. Comley and N. Fleck. Deep penetration and liquid injection into adipose tissue. *Journal of Mechanics of Materials and Structures*, pages 127–140, 2012.

[30] K. Chen, H. Zhou, J. Li, and G. Cheng. A model on liquid penetration into soft material with application to needle-free jet injection. *Journal of Biomechanical Engineering*, 132(101005):1–7, 2010.

[31] K. Chen, H. Zhou, J. Li, and G. Cheng. Stagnation pressure in liquid needle-free injection: Modeling and experimental validation. *Drug Delivery Letters*, 1:97–104, 12 2011.

[32] S. I. Barry, G. Aldis, and G. Mercer. Injection of fluid into a layer of deformable porous medium. *Appl. Mech. Rev.*, 48(10):722–726, 1995.

[33] S. I. Barry., G. Mercer, and C. Zoppou. Deformation and fluid flow due to a source in a poro-elastic layer. *Appl. Math. Modelling.*, 21:681–689, 1997.

[34] R. Portaro and H.D. Ng. Experimental analysis of the performance of an air-powered needle-free liquid jet injector. In *Conf. Proc. IEEE Eng. Med. Biol. Soc. 2013*, pages 3499–3502, 2013.

[35] R. Portaro, H. Nakayama, and H.D. Ng. Optimization of drug viscosity used in gas-powered liquid jet injectors. In *Conf. Proc. IEEE Eng. Med. Biol. Soc. 2015*, pages 7354–7357, August 2015.

[36] D. M. Wendell, B. D. Hemond, N. C. Hogan, A. J. Taberner, and I. W. Hunter. The effect of jet parameters on jet injection. In *Conf. Proc. IEEE Eng. Med. Biol. Soc. 2006*, pages 5005–5008, August 2006.

[37] C. E. Brennen. *Cavitation and Bubble Dynamics.* Cambridge University Press, 2014.

[38] M. J. McCarthy and N. A. Molloy. Review of stability of liquid jets and the influence of nozzle design. *The Chemical Engineering Journal*, 7(1):1–20, 1974.

[39] B. Mohammadi and O. Pironneau. *Applied shape optimization for fluids.* Oxford University Press, 2010.

[40] J. Chang. *Needle-free interstitial fluid acquisition using a Lorentz-force actuated jet injector.* Phd thesis, Massachusetts Institute of Technology, 2014.

[41] Y. Cimbala, A. Yungas, and John. Cengel. *Fluid mechanics : fundamentals and applications (1st ed.).* McGraw-Hill Higher Education, 2006.

[42] M. J. McCarthy. Phd thesis, Univ. of Newcastle, 1972.

[43] D. D. DiBitonto, P. T. Eubank, M. R. Patel, and M. A. Barrufet. Theoretical models of the electrical discharge machining process i. a simple cathode erosion model. *Journal of Applied Physics*, 66(4095), 1989.

[44] M. R. Patel, M. A. Barrufet, P. T. Eubank, and D. D. DiBitonto. Theoretical models of the electrical discharge machining process. ii. the anode erosion model. *Journal of Applied Physics*, 66(4104), 1989.

[45] P. T. Eubank, M. R. Patel, M. A. Barrufet, and B. Bozkurt. Theoretical models of the electrical discharge machining process. iii. the variable mass, cylindrical plasma model. *Journal of Applied Physics*, 73(7900), 1993.

[46] ACGIH. *Industrial Ventilation: A Manual of Recommended Practice for Design, 28th Edition*, 2015.

[47] D. G. Legrand. Crazing, yielding, and fracture of polymers. i. ductile brittle transition in polycarbonate. *J. Appl. Polym. Sci.*, 13(10), 1969.

[48] M. Ashby. *Materials Selection in Mechanical Design.* Elsevier, 2011.